

**NASA CONTRACTOR REPORT**

**UACRL C-920243-12**

**NASA CR-54451**

**INVESTIGATION OF COLLISION PROBABILITY  
OF ELECTRONS AND IONS WITH  
ALKALI METAL ATOMS**

**PREPARED BY R. H. BULLIS AND W. L. NIGHAN**

**N65-28877**

(ACCESSION NUMBER)

(PAGES)

(THRU)

(CODE)

(CATEGORY)

(NASA CR OR TMX OR AD NUMBER)

GPO PRICE \$ \_\_\_\_\_

CFSTI PRICE(S) \$ \_\_\_\_\_

Hard copy (HC) 3.00

Microfiche (MF) .75

ff 653 July 65

**SEMIANNUAL REPORT  
MAY 1965**

**PREPARED UNDER CONTRACT NO. NAS 3-4171**

**BY**

**United Aircraft Research Laboratories**

**U  
UNITED AIRCRAFT CORPORATION  
A**

**EAST HARTFORD, CONNECTICUT**

**FOR**

**NATIONAL AERONAUTICS & SPACE ADMINISTRATION  
LEWIS RESEARCH CENTER  
CLEVELAND, OHIO**

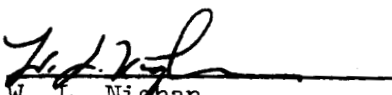
UNITED AIRCRAFT CORPORATION  
RESEARCH LABORATORIES  
East Hartford, Connecticut

NASA Report No.: CR-54451  
United Aircraft Corporation Research Laboratories Report No.: D-920243-12  
Semiannual Report  
Date of Reporting Period: October 22, 1964, to May 11, 1965  
Title of Contract: Investigation of Collision Probability of Electrons and Ions  
with Alkali Metal Atoms  
Contract Number: NAS3-4171  
Contractor: United Aircraft Corporation Research Laboratories  
East Hartford, Connecticut  
203-565-4321  
Principal Investigator: R. H. Bullis


National Aeronautics and Space Administration  
Lewis Research Center  
Space Power Systems Division  
Project Manager: Mr. H. E. Nastelin, MS 500-309

Reported By:

  
R. H. Bullis

  
W. L. Nighan

Approved By:

  
H. D. Taylor, Manager  
Physics Department

Date: July 29, 1965

Report D-920243-12

Semiannual Report Under Contract NAS3-4171  
for the Period October 22, 1964, through May 11, 1965

Investigation of Collision Probability of Electrons and Ions  
with Alkali Metal Atoms

TABLE OF CONTENTS

	Page
SUMMARY . . . . .	1
ELECTRON-CESIUM ATOM COLLISION PROBABILITY MEASUREMENTS . . . . .	2
Introduction . . . . .	2
Theory and Plasma Model . . . . .	3
Verification of Assumptions . . . . .	12
Measurements and Results . . . . .	16
Analysis of Trial Functions for the Cross Section . . . . .	17
Conclusions . . . . .	22
CESIUM ION-ATOM TOTAL COLLISION PROBABILITY MEASUREMENTS . . . . .	27
Introduction . . . . .	27
Description of Experiment and Measurement Techniques . . . . .	28
Analysis of Cross-Section Data . . . . .	32
Measurement and Results . . . . .	34
Outline of Research for the Next Six-Month Period . . . . .	36
REFERENCES . . . . .	37-38
LIST OF FIGURES . . . . .	39-41
FIGURES . . . . .	42
DISTRIBUTION LIST . . . . .	I-VIII

Investigation of Collision Probability of Electrons and

Ions with Alkali Metal Atoms

Semiannual Progress Report - October 22, 1964, to May 11, 1965

Contract NAS3-4171

Summary

This report is a summary of the experimental research investigations conducted at the United Aircraft Corporation Research Laboratories to determine the collision probabilities of electrons and cesium ions with cesium atoms during the second six-month period from October 22, 1964, to May 11, 1965, under Contract NAS3-4171. In previous studies under Contract NASr-112, electron-cyclotron resonance techniques were employed to measure the electron-cesium atom collision probability over an energy range from 0.05 to 0.10 eV. A modified Ramsauer beam experiment was employed under the same contract to measure the collision probability of cesium ions with cesium atoms over the energy range from 0.12 to 9.7 eV. The results of these investigations were reported at the IEEE Thermionic Conversion Specialist Conference, Gatlinburg, Tennessee, on October 7 to 9, 1963. The work under this present contract represents an extension of these earlier investigations. In the first six-month period of the contract, preliminary measurements of electron-cesium atom cross sections were made, and the cesium ion-atom total collision cross-section information obtained under Contract NASr-112 was analyzed to determine low energy cesium ion mobilities. The results of the ion mobility analysis were presented at the IEEE Thermionic Conversion Specialist Conference held in Cleveland, Ohio, on October 26 to 28, 1964. In this period a cesium arc discharge has been used in conjunction with electrostatic and rf conductivity probe techniques to determine the collision probability of electrons with cesium atoms over the energy range from 0.2 to 0.6 eV. Further cesium ion-cesium atom collision probability measurements have been made in the existing modified Ramsauer beam experiment in an attempt to extend the energy range of these measurements below 0.1 eV. Ion beam energy distributions have been obtained at 0.1 eV, ion beams with energies of 0.058 eV have been successfully detected, and preliminary collision cross-section data are reported herein. Experiments are continuing to refine and further analyze these data. A knowledge of both the collision probability of electrons and cesium ions with cesium atoms is essential in the analysis of the neutralization plasma existing in the thermionic converter as well as being important in the analysis of other devices that employ cesium vapor in an ionized state.



## ELECTRON-CESIUM ATOM COLLISION PROBABILITY MEASUREMENTS

## 1. Introduction

Electron-atom momentum transfer collisions are known to play a dominant role in the determination of the transport properties of slightly and partially ionized plasmas. As a result, a knowledge of the elastic electron-cesium atom collision cross section for momentum transfer, or collision probability, is a prerequisite for obtaining an understanding of the physical properties of the non-equilibrium plasma that exists in thermionic converters and other plasma devices employing cesium vapor in an ionized state. In most practical cesium plasma devices, electron mean energies are less than 1 eV. In this range of electron energies, there is approximately an order of magnitude variation in the experimental cross-section values reported in the literature with no particular energy dependence exhibited in the data.

A compilation of the available electron-cesium atom collision probability data is presented in Fig. 1. R. B. Brode<sup>1</sup> measured the total collision probability (approximately equal to the momentum transfer collision probability for nearly isotropic scattering) over thirty years ago using monoenergetic electron beam techniques. His measurements cover a range down to an electron energy of approximately 0.6 eV and are considered to have established at least the approximate magnitude and general qualitative behavior of the collision probability for energies near 1 eV. However, experimental difficulties associated with the use of very low energy electron beams have prevented the extension of these methods to lower energies, and in fact, Brode's measurements have not even been checked for cesium at the higher energies.

The data presented in Refs. 2 to 11 have been determined from electron swarm experiments where the electrons are distributed in velocity over almost the entire energy range from 0 to 1 eV. These experiments were each designed to measure a different electron transport property in a cesium plasma, from which an average collision probability was then determined. For example, the high-frequency microwave effective collision frequency was measured (Ref. 2), microwave cyclotron resonance absorption spectra were studied (Ref. 3), the direct current plasma conductivity was determined (Ref. 5), the dc properties of gas discharges in cesium were measured (Refs. 9 and 10), and the single data points presented in Fig. 1 represent, for the most part, average collisional parameters inferred from the operational characteristics of devices such as the thermionic converter. Unfortunately, the importance of proper averaging of the velocity dependent collision probability over all electron velocities has not been appreciated, and since plasma transport properties depend on the averaging process, large discrepancies in the various measurements can exist as a result of misinterpretation of experimental data, even though the measurements may be correct.

Another significant point is the consideration of the role played by electron-ion collisions in the various investigations. For approximately half

of the available experimental collision probability data, particularly those obtained from device studies, electron-ion effects have been neglected altogether. For the other half, it has been assumed that electron-atom and electron-ion resistive effects can be treated separately and added like resistivities without regard to the method of averaging over the electron velocity distribution. This procedure and other such averaging techniques can result in large errors in the interpretation of experimental data if the collision probability is a strong function of electron velocity, as most of the available experimental and theoretical work for cesium indicates.

The objective of the research program reported herein was to obtain reliable experimental data from measurements of the plasma properties in the positive column of a dc cesium arc discharge, which is amenable to analytical and laboratory diagnosis. These measurements lead to an effective electron-cesium heavy particle collision frequency from which the actual momentum transfer collision probability was then obtained from an analysis of the integral equation describing the effective collision frequency. With these results a comparison was made with the existing collision probability data interpreted on a consistent basis and with the available theoretical predictions of the electron-cesium atom collision probability.

## 2. Theory and the Plasma Model

### Homogeneous Plasma

The equation describing the electron current flow through a plasma under the influence of a dc electric field may be derived on the basis of the physical model for a plasma originally developed by Lorentz.<sup>12,13,14</sup> In this approach, it is assumed that collisions are instrumental in setting up a nearly spherically symmetric velocity distribution of electrons and that small deviations from spherical symmetry are described accurately enough by the second term in the spherical harmonic expansion of the velocity distribution function. Upon substitution of this first order expansion into the Boltzmann equation, two coupled equations describing the relationship of the terms of the expansion result. From these relations and the equation for particle current, the following equation may be obtained for the current density:

$$J = - \frac{4\pi}{3} \frac{n_e e^2}{m} \int_0^\infty \frac{v^3 (\partial f_0 / \partial v)}{\nu_{ed}(v) + \nu_{ei}(v)} dv E, \quad (1)$$

where

- m - electron mass
- e - electronic charge
- v - electron velocity
- $n_e$  - electron number density
- J - current density

- $E$  - electric field intensity  
 $f_0$  - isotropic part (first term in spherical harmonic expansion) of the velocity distribution function normalized with respect to electron density  
 $\nu_{ea}(v)$  - elastic electron-atom collision frequency for momentum transfer  
 $\nu_{ei}(v)$  - effective elastic electron-ion collision frequency for momentum transfer

In this derivation it has been assumed that the plasma is homogeneous, that the collisional friction force exerted on electrons is due to elastic momentum transfer encounters with heavy particles which are assumed infinitely massive in comparison with electrons, and that electron-electron encounters have no direct influence on the momentum of the electron gas. A more complete analysis of the problem, which yields this result, is presented in Ref. 13.

For the cesium arc discharge plasma (to be described in Section 3), which is the subject of this analysis, the relatively high degree of ionization results in extremely short electron thermalization times. Therefore, it will be assumed that electron-electron collisions are influential in establishing a Maxwellian distribution of electron velocities, and Eq. 1 becomes

$$J = \frac{8}{3\sqrt{\pi}} \frac{n_e e^2}{m} \left( \frac{m}{2kT_e} \right)^{\frac{5}{2}} \int_0^{\infty} \frac{v^4 e^{-\frac{mv^2}{2kT_e}}}{\nu_{ea}(v) + \nu_{ei}(v)} dv E, \quad (2)$$

where  $k$  is Boltzmann's constant and  $T_e$  the electron temperature. The validity of the assumed Maxwellian form for the electron velocity distribution and of the other assumptions in this derivation will be analyzed in Section 4. Equation 2 can be expressed in the convenient form

$$J = \frac{n_e e^2}{m \nu_{eff}} E, \quad (3)$$

where  $\nu_{eff}$ , the effective electron heavy particle momentum transfer collision frequency, is defined by

$$\nu_{eff}^{-1} = \frac{8}{3\sqrt{\pi}} \left( \frac{m}{2kT_e} \right)^{\frac{5}{2}} \int_0^{\infty} \frac{v^4 e^{-\frac{mv^2}{2kT_e}}}{\nu_{ea}(v) + \nu_{ei}(v)} dv. \quad (4)$$

The velocity dependent electron-atom and electron-ion collision frequencies are related to their respective momentum transfer cross sections by

$$\nu_{ea}(v) = n_a Q_{ea}(v)v, \quad \nu_{ei}(v) = n_i Q_{ei}(v)v, \quad (5)$$

where

$n_a$  - atom density

$Q_{ej}(v)$  - elastic electron-atom momentum transfer cross section

$n_i$  - ion density (equal to electron density in a neutral plasma)

$Q_{ei}(v)$  - effective elastic electron-ion cross section.

The substitution of this form for the collision frequency into Eq. 4, after normalization with respect to atom density, results in the following expression for the normalized effective collision frequency:

$$\nu_{eff}^{*-1} = \left( \frac{\nu_{eff}}{n_a} \right)^{-1} = \frac{8}{3\sqrt{\pi}} \left( \frac{m}{2kT_e} \right)^{\frac{5}{2}} \int_0^{\infty} \frac{v^3 e^{-\frac{mv^2}{2kT_e}}}{Q_{ej}(v) + \alpha Q_{ei}(v)} dv = g(T_e, \alpha), \quad (6)$$

where  $\alpha$  is the degree of ionization defined as the ratio of electron density to atom density. Equation 6, defining the normalized effective collision frequency, represents an average of the total normalized electron heavy particle momentum transfer collision frequency and is a function of electron temperature and degree of ionization alone. It should be noted that this normalized effective collision frequency is not the simple average of collision frequency over the velocity distribution but rather is the average of the reciprocal sum of momentum transfer collision frequencies representing specifically the over-all resistive effect of momentum transfer collisions on dc current flow. This collision parameter, if known as a function of electron temperature and degree of ionization, would be extremely useful in the calculation of dc transport properties in plasmas satisfying the assumptions made in this analysis.

Equation 5 relates the effective elastic electron-ion momentum transfer collision frequency to an electron-ion collision cross section which represents the collective effects of electron-ion interactions. Isolated coulomb collisions in a plasma cannot be physically distinguished because of the long range of the coulomb force field. However, as an approximation, a two-body coulomb collision term can be derived classically in which scattering is limited to particles within a Debye sphere about the test charge. This procedure eliminates the divergence of the integral describing the effective electron-ion momentum transfer cross section and reasonably accounts for the shielding effect which results in the necessarily finite value for the cross section. The derivation of the effective electron-ion collision term presented in detail in Refs. 13 and 15 reduces to the following expression:

$$Q_{ei}(v) = \frac{e^4}{4\pi\epsilon_0^2 m^2 v^4} \cdot \log_3 \left[ \frac{12\pi(\epsilon_0 k T_e / e^2)^{3/2}}{n_e^{1/2}} \right], \quad (7)$$

where  $\epsilon_0$  is the permittivity of free space. Upon substitution of the appropriate constants and after consideration of the experimental range of electron temperatures and densities covered in this investigation, Eq. 7 becomes

$$Q_{ei}(v) = 0.806 \times 10^7 \delta(T_e) v^{-4}, \quad (8)$$

where  $\delta(T_e)$  is approximately one and results from the logarithmic term in Eq. 7. Equation 8 is plotted in Fig. 2 for two typical electron temperatures. The representation of the effect of electron-ion interactions by Eqs. 7 and 8 is adequate for the purpose of this investigation, since electron-ion effects never dominate in the range of plasma conditions encountered in this experiment.

#### Diffusion Dominated Arc Discharge Plasma

In the analytical development leading up to Eq. 6, it was assumed that the plasma was homogeneous. In the case of the cylindrical cesium arc discharge, it is assumed that axial and circumferential uniformity exists and that the only gradient in the radial direction is the electron density variation resulting from particle diffusion to the walls of the discharge tube. Because there are no significant plasma gradients in the direction of discharge current flow, the plasma behaves as though it were homogeneous, and a simple averaging process can be used to account for the radial variation in discharge current density caused by the diffusion gradient in electron density. When the radial variation in the degree of ionization is considered, Eq. 2 becomes

$$J(r) = \frac{8}{3\sqrt{\pi}} \frac{a(r)e^2}{m} \left( \frac{m}{2kT_e} \right)^{\frac{5}{2}} \int_0^{\infty} \frac{v^3 e^{-\frac{mv^2}{2kT_e}}}{Q_{ea}(v) + a(r)Q_{ei}(v)} dv, \quad (9)$$

where the form relating the collision frequency to cross section (Eq. 5) has been used. Since it is assumed that circumferential uniformity in plasma properties exists, the current flow through a cross sectional area of the discharge tube is given by

$$I = 2\pi \int_0^R J(r) r dr, \quad (10)$$

where  $I$  is the discharge current and  $R$  the tube radius. If it is assumed that the radial variation in degree of ionization can be reasonably represented by a parabola of the form

$$a(r) = a_0(1 - r^2/R^2), \quad (11)$$

where  $\alpha_0$  is the degree of ionization on the tube axis, and this form is then used in Eqs. 9 and 10, the total discharge current becomes

$$I = \frac{16\sqrt{\pi}}{3} \cdot \frac{\alpha_0 e^2}{m} \left( \frac{m}{2kT_e} \right)^{\frac{5}{2}} \int_0^R \int_0^\infty \frac{(1-r^2/R^2) v^3 e^{-\frac{mv^2}{2kT_e}}}{Q_{ea}(v) + \alpha_0 (1-r^2/R^2) Q_{ei}(v)} r dv dr E. \quad (12)$$

Since  $r$  and  $v$  are independent, the radial integration can be performed, and Eq. 12 reduces to

$$I = \frac{16}{3\sqrt{\pi}} \cdot \frac{\alpha_0 e^2}{m} \left( \frac{m}{2kT_e} \right)^{\frac{5}{2}} \int_0^\infty \frac{v^3 e^{-\frac{mv^2}{2kT_e}}}{\alpha_0 Q_{ei}(v)} \left[ 1 + \frac{Q_{ea}(v)}{\alpha_0 Q_{ei}(v)} \log_e \left( \frac{Q_{ea}(v)}{Q_{ea}(v) + \alpha_0 Q_{ei}(v)} \right) \right] dv \frac{\pi R^2}{2} E. \quad (13)$$

Once again an effective collision frequency can be defined from the relationship between current flow and electric field intensity, i.e.,

$$I \equiv \frac{n_{e0} e^2}{m \nu_{eff}} \cdot \frac{\pi R^2}{2} E. \quad (14)$$

Solving for the effective collision frequency defined by Eqs. 13 and 14 and normalizing with respect to atom density yields

$$\nu_{eff}^{-1} = \frac{16}{3\sqrt{\pi}} \left( \frac{m}{2kT_e} \right)^{\frac{5}{2}} \int_0^\infty \frac{v^3 e^{-\frac{mv^2}{2kT_e}}}{\alpha_0 Q_{ei}(v)} \left[ 1 + \frac{Q_{ea}(v)}{\alpha_0 Q_{ei}(v)} \log_e \left( \frac{Q_{ea}(v)}{Q_{ea}(v) + \alpha_0 Q_{ei}(v)} \right) \right] dv = g(T_e, \alpha_0). \quad (15)$$

This expression, like Eq. 6 for the homogeneous case, represents the normalized average of the total electron heavy particle momentum transfer collision frequency, with the exception that in Eq. 15 spatial averaging has been performed to account for the radial dependence of the electron-ion contribution to the over-all resistance to discharge current flow.

It is apparent from Eq. 15 that knowledge of the normalized effective collision frequency dependence on electron temperature and degree of ionization could lead to information pertaining to the electron-atom cross section which appears in the integrand of the integral. An extensive numerical analysis of trial functions for the electron-atom cross section has been carried out based on the experimental information obtained from this investigation. The results of that analysis are presented in Section 6.

The normalized effective collision frequency of Eq. 15 can be related to the measurable parameters of the cesium discharge plasma from Eq. 14. Using the perfect gas relationship

$$n_a = \frac{P}{kT_g} \quad (16)$$

where

P - cesium vapor pressure  
 $T_g$  - cesium vapor temperature,

the following expression for the effective collision frequency can be obtained:

$$\nu_{eff}^* = \frac{e^2 k}{2m} \cdot \frac{\pi R^2 n_{e0} E}{(P/T_g) I} \quad (17)$$

Equation 17 was used to determine experimentally the normalized effective collision frequency from measurements of electron density, electric field intensity, gas pressure and temperature, and discharge current.

### 3. Description of the Experiment and Diagnostic Techniques

#### Discharge Tube

The laboratory plasma used in this investigation was the positive column of a cesium arc discharge. The theoretical analysis presented in the previous section was used to describe the arc discharge plasma which has properties in the ranges of practical interest and which is more suitable for laboratory diagnosis than cesium plasma devices such as the thermionic converter. For moderate cesium pressures ( $10^{-2}$  to  $10^{-1}$  mm Hg) and arc currents (0.3 to 1.5 amps), the electron temperature in the positive column varied from approximately 2500 to 4500°K, the electric field from 0.2 to 0.6 volts/cm, the electron density from  $10^{11}$  to  $3 \times 10^{12}$  elec/cc, and the degree of ionization from approximately  $3 \times 10^{-4}$  to  $3 \times 10^{-3}$ .

Of the parameters in Eq. 17 required to obtain experimentally the normalized effective collision frequency, the electron density and temperature are the two most difficult to measure. Various plasma diagnostic techniques are available; however, the most practical for obtaining these particular plasma properties is the electrostatic probe. From an analysis of the current-voltage characteristics of an electrostatic probe, the electron temperature and density can be determined and the assumption regarding the equilibrium distribution of electron energies verified. In addition, the electric field can be determined from plasma potential measurements made with probes positioned axially along the positive column. A high degree of spatial resolution can be realized with electrostatic probes, and they can be moved from point to point in the plasma to measure local conditions.

As a check on the potential measurements made with electrostatic probes and on the discharge current measurements, rf conductivity probes have been used to measure the plasma conductivity. With this technique a small probing rf coil is inserted in the plasma. The magnetically induced rf electric field of the coil penetrates into the plasma which behaves as a lossy medium for the rf power, loading the coil to an extent determined by the plasma conductivity. Therefore, a measurement of the power dissipated can be directly related to the plasma conductivity. These measurements provide an independent check on the experimentally determined ratio of current density to electric field intensity. A description of the rf probe and its associated instrumentation is presented in Refs. 16 and 17.

A photograph of a typical discharge tube is shown in Fig. 3. Cathode-to-anode separation in this tube is 50 cm, and the inside diameter is 3.8 cm. The cathode, a 1.25 cm in diameter tantalum tube, received heat indirectly from a tungsten filament positioned within the tantalum tube which provided a separate vacuum chamber for the filament, isolating it from the plasma. Ceramic spacers prevented electrical contact between the cathode and heater which was bifilar wound in order to effectively cancel the magnetic field resulting from the flow of current through the heater. The electrostatic probe sidearm assemblies shown in the photograph are constructed in such a way that the probes, which protrude through a small hole in the wall of the discharge tube, could be moved radially into the plasma by means of a magnet. The probes were constructed of 0.010-in. diameter tungsten rod covered with a glass sheath which served as an electrical insulator. The entire assembly averaging 0.018 in. in diameter was ground flat, exposing only the 0.010-in. tungsten tip to the plasma. Great care was exercised in the fabrication of the electrostatic probes in order to make them as small as possible and so that the tip of the probe (collection area) exposed to the plasma was both flat and flush with the glass insulation. The probe tips were periodically examined with a microscope at operating temperature in the discharge tube so that any flaw could be detected. A schematic of the moveable probe and sidearm assembly is shown in Fig. 4.

During operation the tube was located within a dual oven assembly which controlled the gas temperature and prevented cesium from condensing on the tube walls. The cesium appendix shown in Fig. 3 extends down to the lower portion of the oven, which was always held at a lower temperature than the main oven in order to control the cesium vapor pressure. The cesium pressure was determined from the cesium vapor pressure curve of Ref. 18 and is a strong function of temperature. Consequently, stabilization and control of the temperature in the pressure control oven containing the cesium reservoir was critical. The temperature in this oven, which was varied from 150 to 200°C in order to achieve the range of pressures of interest, was controlled by a temperature stabilization circuit capable of holding the oven temperature to within  $\pm 1/2^\circ\text{C}$ , equivalent to a pressure variation of approximately  $\pm 2$  per cent. The sensing element for the circuit was a commercially available platinum wire resistor positioned in close contact with the liquid cesium in the appendix. Cesium reservoir temperature was measured with two precision grade laboratory thermometers which were calibrated by the manufacturer against



a standard that has been calibrated at the NBS. These thermometers were certified accurate to  $\pm 1/8^\circ\text{C}$ . Temperature gradients inside the oven were effectively eliminated by circulating the air with a fan. In order to determine the gas temperature, thermocouples were secured to the glass wall of the discharge tube. A thermocouple positioned in a small well on the tube axis and one positioned near the inside wall of the tube verified that the arc did not cause significant heating of the gas.

Figure 5 shows a tube designed for use with the rf conductivity probe. The conductivity probe shown in the figure was inserted axially through a hole in the anode in order to take advantage of the common symmetry of the probe, rf fields, and the plasma. Figure 6 is a detailed view of the anode area of this tube. Electrostatic probes were positioned in the region of the conductivity probe so that the electric field could be determined in the portion of the discharge tube occupied by the probe well. During operation the rf coil was positioned along the tube axis at the midpoint between the two electrostatic probe locations shown in Fig. 6. The probe coil shown in this photograph contained approximately 20 turns of 0.010-in. gold wire wrapped in the grooves of a threaded glass sleeve; the coil was 0.25 in. long.

#### Electrostatic Probe Measurements

The electron temperature, electron density, and plasma potential variations in the discharge have been measured using pulsed, electrostatic probe techniques. A pulsing system was used to apply a cleaning pulse, sweep voltage or data acquisition pulse, and rest voltage to the probe; the time duration of each portion of the probe pulse could be varied independently. The time scale of the total pulse applied to the probe with this system ranged from approximately 100 microseconds to 100 milliseconds. With such versatility the effect of changing probe surface conditions, errors due to circuit and plasma response limitations, and the effect of plasma drift or instability could be detected. The importance of being able to vary sweep speed and applied voltage in this manner is detailed in Refs. 19 and 20.

Since the physical presence of the probe may significantly perturb the plasma, as outlined in Ref. 21, errors in the determination of electron density from probe measurements can be related to probe size. In order to check on possible perturbations of the plasma resulting from the presence of the electrostatic probes, a special discharge tube was constructed which contained probes of a significantly larger size than the 0.010-in. diameter probes described previously. Incorporated in this tube were three 0.010-in. diameter and two 0.0315-in. diameter electrostatic probes alternately positioned along the tube axis. The large probes occupied a volume about three times as large as the small probes and had a collection area approximately ten times larger. Measurements made over the entire range of cesium pressures and arc currents used in this investigation indicated no significant variation of either electron density or temperature with probe size. The greatest discrepancy in the electron density, as determined with the large and small probes, was 20 per cent at the highest cesium pressure. On

the basis of these results, it was concluded that the small 0.010-in. diameter probes did not perturb the plasma for the conditions encountered in these measurements.

### Conductivity Probe Measurements

Conductivity probing techniques have been used as a check on the measurement of the ratio of current density to electric field intensity (an average conductivity). This ratio was determined from measurements of the plasma floating potential along the tube axis and the current flowing through the plasma. The rf probe detects the conductivity in its immediate vicinity by dissipating a very small amount of radio frequency (10 mc) power in the plasma. This weak interaction with the plasma was detected by observing the resistive loading of a sensitive oscillator-detector. The loading was then compared with a calibration curve obtained by placing the probe in a variety of salt solutions having known conductivities. From such a comparison the conductivity of the plasma was determined. A typical calibration curve is shown in Fig. 7. Probes of this type are very sensitive to temperature change and must be temperature corrected by determining the amount of energy dissipated in known resistive loads at the temperatures the probes will encounter in operation (200 to 300°C). The amount of energy dissipated at operating temperature was then compared to the amount dissipated at room temperature for a fixed resistive load. From this information a temperature correction was applied to the salt solution calibration curve so that temperature effects could be distinguished from those due to real power dissipation in the plasma. In order to make a valid comparison of the data obtained by the two methods, the manner in which the radial variation of the conductivity was weighted by each measuring technique has been considered. The conductivity obtained from the floating potential and discharge current measurements was a simple average of the radial conductivity variation, whereas the conductivity obtained from the rf probe measurements was weighted by the square of the rf electric field. A comparison of the two techniques has been made by numerically integrating the appropriate averages for a class of functions representative of the radial variation in plasma conductivity in the vicinity of the probe well. Since the main plasma loss mechanism was diffusion, the plasma conductivity was assumed to vary from a maximum value near the center of the annular region occupied by the plasma to zero at both the wall of the probe well and the wall of the main tube. With this assumption, the integration describing both averages was then performed numerically. The ratio of the averages is a correction factor relating the data obtained from the two conductivity measurement techniques. The correction factor obtained in this manner was approximately 1.1. A slight modification of the assumed radial conductivity variation or of the radial dependence of the rf electric field amounted to only about one or two per cent, and therefore, a ratio factor of 1.1 was used to compare the data obtained using the two techniques.

Using the rf conductivity probe, measurements of plasma conductivity were made as a function discharge current and cesium pressure and compared to the average conductivity determined from the ratio of current density to electric field intensity as determined from the electrostatic probes. Figure 8 shows a typical plot of conductivity as a function of arc current. It can be seen that the agreement

between the two techniques was quite good, with the largest discrepancy (30 per cent) occurring at low discharge currents. The difference between the two techniques was within the limits of experimental uncertainty of the conductivity probe measurements, and therefore, it was concluded that the electric field as determined from floating potential measurements made with the electrostatic probes was correct.

#### 4. Verification of Assumptions

During the course of the theoretical analysis describing the plasma model, which was to be representative of the laboratory plasma, several restricting assumptions were made which require some justification if the model is to be considered reasonable.

##### Spherical Symmetry of the Distribution Function

In the series expansion of the electron velocity distribution function, it has been assumed that small deviations from spherical symmetry are described adequately by the second term in the expansion. That is, the anisotropy of the distribution function due to the net flow of current was assumed to be small. This is equivalent to the requirement that the average drift velocity of the electrons must be small compared to their thermal speeds. For the range of operating conditions of this experiment, this condition was satisfied as can be seen from the following relations. The current density is related to the average drift velocity by

$$J = n_e e \langle v_d \rangle_v, \quad (18)$$

where  $\langle v_d \rangle_v$  is the drift velocity averaged over all electron velocities. From Eqs. 3 and 18 it is apparent that the drift velocity is given by

$$\langle v_d \rangle_v = \frac{e E}{m \nu_{\text{eff}}}. \quad (19)$$

The most probable velocity for a Maxwellian distribution is

$$v_{\text{mp}} = \left( \frac{2 k T_e}{m} \right)^{1/2}, \quad (20)$$

and it is required that

$$\frac{\langle v_d \rangle_v}{v_{\text{mp}}} = \frac{e E / m \nu_{\text{eff}}}{(2 k T_e / m)^{1/2}} \ll 1. \quad (21)$$

For the experimental variations of electric field intensity, effective collision frequency and electron temperature encountered in this experiment, this ratio was approximately 0.05 and varied very little about this value. Consequently, the first order expansion for the distribution function is adequate.

#### Contributions to Electron Heavy Particle Collision Frequency

The assumption that the only significant contribution to the velocity dependent momentum transfer collision frequency comes from elastic electron-atom and electron-ion collisions is also reasonable. For the electron temperatures encountered in this investigation, the contribution to the total momentum transfer collision frequency from inelastic collisions must be approximately two orders of magnitude less than that due to elastic electron heavy particle collisions because of the very small percentage of electrons having sufficient energy to make an inelastic collision with a cesium atom. Mutual electronic interactions cannot alter the momentum of the electron gas directly, since the total change of momentum in such encounters must be zero. Although electron-electron collisions can influence the rate of electron heavy particle collisions by altering the anisotropic part of the distribution function, the resultant change in the effective collision frequency has been found to be only about 40 per cent for the case of a fully ionized plasma which would represent the extreme case.<sup>22</sup> Therefore, for the degrees of ionization encountered in this investigation ( $10^{-4}$  to  $10^{-3}$ ), this effect must be small.

#### Form of the Distribution Function

A knowledge of the form of the isotropic part of the velocity distribution function is of prime importance. It has been assumed that mutual electron interactions are effective in establishing a nearly Maxwellian distribution of electron velocities. This assumption is reasonable for the degrees of ionization encountered in this investigation, as can be shown by the following analysis. The rate of energy input to the electrons from the electric field must be balanced by the rate of inelastic electron energy loss, which is the dominant energy loss mechanism in the cesium arc discharge. Therefore, as energy is supplied to the electrons residing in the body of the velocity distribution by the electric field, it must be redistributed through electron interactions in such a way as to replace the losses due to inelastic collisions in the tail of the distribution. In this manner the process is maintained. As the degree of ionization rises, the more frequent encounters between electrons tend to drive the distribution function towards Maxwellian. The transition in the distribution from that characteristic of a weakly ionized gas to a Maxwellian distribution occurs over several orders of magnitude in degree of ionization. However, an indication of the likelihood of the existence of a Maxwellian distribution can be obtained by comparing the approximate rate of electron energy exchange for a Maxwellian distribution to the rate of energy input from the electric field. An approximate expression for the rate of energy exchange among the electrons of a Maxwellian distribution is

$$\frac{U_{th}}{\tau_{ee}} = \frac{k T_e}{\frac{3\pi^{3/2}}{2n_e} \left(\frac{\epsilon_0 m}{e^2}\right)^2 \left(\frac{3kT_e}{2m}\right)^{3/2}} \log_e \left[ \frac{12\pi(\epsilon_0 k T_e / e^2)^{3/2}}{n_e^{1/2}} \right], \quad (22)$$

where  $U_{th}$  is the energy corresponding to the most probable electron speed and  $\tau_{ee}$  is an electron-electron relaxation rate characteristic of the time required for an electron to approach the average energy of the distribution.<sup>13</sup> The rate of energy input from the field is given approximately by the ratio of the average drift energy to the average relaxation time of the drift energy; i.e.,

$$\frac{U_d}{\tau_{eff}} = m \langle v_d \rangle_v^2 \nu_{eff} = \frac{(e E^2)}{m \nu_{eff}}. \quad (23)$$

It is required that

$$\frac{U_{th}/\tau_{ee}}{U_d/\tau_{eff}} \gg 1 \quad (24)$$

For the ranges of electron temperature, electron density, electric field intensity, and effective collision frequency encountered in this experiment, this ratio varied from approximately 10 to 100. This indicates that the rate at which the electrons of a Maxwellian distribution could replenish the losses due to inelastic collisions in the high energy tail of the velocity distribution greatly exceeds the rate at which these losses occur. Therefore, it is reasonable to assume that the distribution function was Maxwellian for the body of slow electrons responsible for the transport properties in the plasma. Deviations from the Maxwellian form probably occur in the vicinity of the first excitation level, 1.38 eV for cesium. However, the trial function analysis (to be discussed in Section 6) has shown that, for the range of electron temperatures encountered in this investigation, the exact form of the various terms in the integrand of the integral equation describing  $\nu_{eff}^*$  (Eq. 15) is of little importance for electron energies greater than about 0.7 eV and has almost no effect for energies greater than 1 eV. It is for this reason that the collision probability velocity structure cannot be determined above about 0.6 eV (Section 6). The linear behavior of the semilog plots of the electrostatic probe current-voltage characteristic is experimental verification of the existence of a Maxwellian distribution of velocities, at least for the slow moving electrons in the body of the distribution. A typical probe curve (Fig. 9) exhibits the linear behavior indicative of the existence of a Maxwellian distribution over approximately one and a half decades in probe current. Deviations from linearity at the low probe currents (approximately 10 microamps) were random in nature and due to the limits of sensitivity of the system.

### Spacial Variation of Plasma Properties

The approximation of the radial variation of the degree of ionization by a parabola has been verified experimentally. In a diffusion dominated plasma the electron density would be expected to fall from a maximum on the tube axis to very nearly zero as the tube wall is approached. If the rate of electron production is directly proportional to electron density, the radial profile would follow a zero-order Bessel function. Radial measurements of electron density have been made with the moveable electrostatic probes over all ranges of discharge current and pressure. A typical plot of the radial density profile is shown in Fig. 10 for various arc currents where a comparison is made with both the lowest order Bessel function and the assumed parabolic form. It is apparent from this figure that the assumption of a parabolic radial dependence for the electron density and consequently the degree of ionization was satisfactory. The electron temperature determined from the radial measurements showed no significant dependence on radial position. The verification of the existence of the diffusion profile in electron density and the symmetry of the density profile with respect to the tube center line are further evidence that the electrostatic probes are not perturbing the plasma.

The Bessel function in Fig. 10 seems to be a slightly better fit to the data than the parabola. However, use of the Bessel function rather than the parabola in the analysis of Section 2 would result in an unnecessary complication of the mathematics. A correction factor could be used to alter the parabolic form so that the radial average of the parabola and the best curve through the data would be the same. However, this correction would be small and well within the limits of experimental uncertainty. Consequently, since nothing meaningful would be gained by making such a correction, the parabolic form of Eq. 11 was used in the calculations of the normalized effective collision frequency.

The axial uniformity of plasma properties was verified from measurements made with electrostatic probes positioned axially along the discharge column. Measurements made over all discharge conditions indicate no significant axial gradients in plasma properties.

## 5. Measurements and Results

Typical measurements were conducted with cesium pressure and discharge current as independent experimental variables. All other plasma properties are established by fixing these two parameters and the temperature of the gas. The experimentally determined plasma properties for a typical test run are presented in Figs. 11 to 14. Figure 11 presents the electron temperature determined from the slope of the semilog current-voltage characteristics of the electrostatic probes as a function of discharge current and cesium pressure. As can be seen from the figure, the electron temperature is rather insensitive to pressure but is a rather strong function of discharge current, particularly for low currents. Approximately a 2000°K temperature range is covered in these measurements with the electron temperature varying from approximately 2500 to 4500°K. The variation of electric field in the plasma with discharge current and pressure is shown in Fig. 12. From measurements of the plasma floating potential obtained with probes positioned along the axis of the tube and from a knowledge of the spacing between probes, the electric field intensity was calculated and found to vary from about 0.2 to 0.6 volts/cm. The electric field, which supplies energy to the electron gas, has the same qualitative behavior with current and pressure as the electron temperature. The electron density in Fig. 13 is the value measured on the axis of the tube and exhibits a strong dependence on both discharge current and pressure. From the value of the electron density, which varies from about  $10^{11}$  to  $3 \times 10^{12}$  electrons/cc, and the cesium atom density calculated from the perfect gas law (Eq. 16), the degree of ionization was obtained and is plotted in Fig. 14. Note that, although the absolute value of electron density increases with increasing pressure, the degree of ionization decreases. Because of the radial variation of electron density and the independence of atom density on tube radius, the degree of ionization varies radially in the same manner as the electron density (Fig. 10).

### Experimentally Determined Effective Collision Frequency

Using the relationship of Eq. 17, the normalized effective electron-cesium heavy particle collision frequency has been determined over the range of plasma variables from the experimental data of several test runs, such as those in Figs. 11 to 14. Figure 15 presents this effective collision frequency as a function of electron temperature and degree of ionization on the tube axis. The effective collision frequency data of this figure were obtained from two different discharge tubes and several electrostatic probes positioned at different points along the tube axis. In spite of this variation in experimental conditions, the scatter in the data points is very small. As is apparent from Fig. 15, a clearly defined trend in the collision frequency exists with both electron temperature and degree of ionization. Of particular significance is the strong dependence of effective collision frequency on electron temperature. Moving along a constant degree of ionization line, the effective collision frequency increases by a factor of two over the experimental temperature range. Also significant is the fact that the collision frequency shows

a pronounced dependence on the degree of ionization in the  $10^{-4}$  to  $10^{-3}$  range, where electron-ion effects in cesium plasmas are often neglected. Consequently, the necessity of including electron-ion effects in the theoretical analysis of the plasma model becomes apparent.

Although the arc discharge used in this investigation is essentially free from gradients in the direction of current flow, many practical cesium devices, such as the arc mode thermionic converter, have significant variations in plasma properties along the direction of electron transport.<sup>23</sup> Since the electron heavy particle collisions impede the motion of electrons due to density and energy gradients in much the same fashion as in the case of electron mobility due to electric fields, it can be shown that the equations relating plasma transport properties to the effective collision frequency can be expanded in more general terms to include plasma nonuniformities. When this is done, the theoretical integral expressions for effective collision frequency (Eqs. 6 and 15) appear in the resulting gradient terms. Therefore, the experimental determination of the effective collision frequency (Fig. 15) is of considerable value when making calculations pertaining to device performance, et al, since the experimentally determined effective collision frequency is equal to the integral equation itself. However, because of the experimental and analytical difficulties encountered when working with cesium plasmas, prior to the completion of this investigation, no other effective collision frequency measurements covering the practical range of electron temperatures and degrees of ionization were available.

#### 6. Analysis of Trial Functions for the Cross Section

Since the experimental measurement of plasma properties leads to a normalized effective electron-cesium heavy particle collision frequency (Fig. 15), which is an average over all electron velocities, it is necessary to determine how the integral (Eq. 15) describing this collision frequency behaves as a function of electron temperature and degree of ionization for variations in the form of the velocity dependence of the collision probability. Numerical integration techniques permit analysis of this integrated behavior for trial forms of the collision probability velocity dependence. Initially, various trial forms were selected on the basis of best estimates as to the magnitude of the collision probability and on trends observed in experimental and theoretical data. Subsequently, hundreds of additional functions representing almost every reasonable magnitude and velocity dependence in the range of interest were numerically integrated, yielding a variety of hypothetical normalized effective collision frequency curves with electron temperature and degree of ionization as variables. This was done so that an accurate estimate of the resolution of the technique could be made and so that trends in the experimental data could be understood and related to the type of cross-section behavior most likely to have produced them.



### Trial Function Technique

As an illustration of the trial function technique, Fig. 16 presents four hypothetical trial functions for the collision probability. These functions were chosen to represent significantly different velocity dependent behavior in the range of maximum sensitivity of this experiment; i.e.,  $0.3$  to  $0.8\sqrt{\text{eV}}$ . In order to illustrate the differences in the integrated values of such functions, the collision probability curves of Fig. 16 were integrated using Eq. 15 and compared with the experimental data of Fig. 15. This comparison is presented in Fig. 17. On Examination of this figure, it is apparent that the qualitative and quantitative behavior of the normalized effective collision frequency, over the range of electron temperatures and degree of ionization covered in this investigation, is significantly dependent on the magnitude and velocity structure of the collision probability. Of the four illustrative examples treated, none exhibits the strong electron temperature dependence, coupled with the uniform spacing with varying degree of ionization, of the experimental effective collision frequency data (dashed lines in Fig. 17). Even Curve B, which yields fair agreement with the experimental data for the lower electron temperatures, results in effective collision frequencies which are low by approximately 50 per cent at the higher temperatures. The analysis of the numerical and experimental data in Figs. 16 and 17 is illustrative of the comparative techniques used to analyze a wide variety of trial functions for the electron-cesium atom collision probability. However, it is worth repeating that in order to make a realistic appraisal of the resolution in the collision probability velocity structure that could reasonably be expected, several hundred trial functions have been numerically integrated and analyzed.

### Comparison of Numerical and Experimental Data

Following the procedures outlined in the previous paragraphs, a particular class of functions for the velocity dependent electron-cesium atom momentum transfer cross section has been found, which, when integrated, gives the best fit to the experimental data of Fig. 15. The integrated value of this best estimate for the cross section is compared in Fig. 18 with the experimental data. The dashed lines of Fig. 18 are the same straight lines drawn through the effective collision frequency data of Fig. 15. It is apparent from this figure that the quantitative and qualitative agreement between theory and experiment is quite good. The slope of the effective collision frequency temperature dependence is exactly duplicated by the theoretically calculated curve, and the agreement between theory and experiment for the parametric dependence on the degree of ionization is also very good. The maximum discrepancy that does occur for the highest degree of ionization ( $24 \times 10^{-4}$ ) is only 15 per cent, which is well within the limits of uncertainty of the experiment, the theoretical model, and the theoretical form used to represent electron-ion effects. The match between theory and experiment can be improved by decreasing the electron-ion term ( $\alpha_0 Q_{ei}(v)$ ) in Eq. 15 with a corresponding increase in the electron-atom term  $Q_{eo}(v)$ . For example, a 25 per cent reduction in  $\alpha_0 Q_{ei}(v)$  at each velocity point for a degree of ionization of  $6 \times 10^{-4}$ , when added to the  $Q_{eo}(v)$  used in the

calculations leading to the numerical data of Fig. 18, results in almost a perfect match between theory and experiment when  $\nu_{\text{eff}}^*$  is recalculated for  $\nu_0$  equal to 3, 12, and  $24 \times 10^{-4}$ , using the modified electron-atom cross section. A variation of 25 per cent in  $\nu_0 Q_{\text{eff}}(\nu)$  is within the limits of uncertainty associated with this term, and therefore, additional refinement of the approximation for  $Q_{\text{eff}}(\nu)$  would not be meaningful.

#### Electron-Cesium Atom Collision Probability

Only one class of functions for the velocity dependent collision probability yields the agreement between theory and experiment described in the previous paragraph and shown in Fig. 18. Figure 19 presents this collision probability (solid line in the figure) as a function of electron velocity. As can be seen from the figure, the collision probability resulting in the best agreement between theory and experiment is a strong function of electron velocity, rising from a minimum value of approximately 100 collisions per cm per mm Hg in an electron velocity range corresponding to  $0.4$  to  $0.6 \sqrt{\text{eV}}$  to a maximum over an order of magnitude larger at a velocity in the  $0.7$  to  $0.8 \sqrt{\text{eV}}$  range where the strong possibility of a resonance in the collision probability exists. It is this very rapid increase in the collision probability at approximately  $0.7 \sqrt{\text{eV}}$  that produces the strong electron temperature dependence of the effective collision frequency. There is a loss of sensitivity below about  $0.4 \sqrt{\text{eV}}$  due to the fact that for lower electron velocities electron-ion interactions begin to dominate the collisional process for the degrees of ionization covered in this experiment. A decrease in sensitivity at the high energy end of the velocity spectrum results from the small number of electrons in the tail of the electron velocity distribution. However, for higher electron velocities the collision probability must maintain the approximate magnitude indicated by the cross hatched area of the figure; this magnitude is in agreement with that established by Brode's total collision probability data. Although the collision probability velocity structure cannot be precisely determined above a velocity of about  $0.8 \sqrt{\text{eV}}$ , the magnitude above this level still carries weight in the integration leading to the effective collision frequency. For example, in various trial integrations resonances in the collision probability with values in excess of 3000 collisions per cm per mm Hg at an electron velocity of about  $1 \sqrt{\text{eV}}$  were used in the calculation of the effective collision frequency. These functions fall within the envelope defined by the dashed lines in Fig. 19. This envelope indicates the limits of uncertainty in the collision probability in various velocity ranges; the manner in which the envelope was established is discussed in a subsequent paragraph.

#### Resolution of Trial Function Technique

The improvement of the resolution of this technique due to the requirement that the theoretically calculated effective collision frequency match the experimental effective collision frequency behavior as a function of two variables (electron temperature and degree of ionization), rather than the usual single parameter (electron

temperature), can be seen from the following example. Figure 20A shows the effective collision frequency for very low degrees of ionization (all electron-ion interactions neglected) calculated from the collision probability of Fig. 19 (solid line). If it is assumed that this represents experimental data, another function which will match this data reasonably well, the curve labeled b in Fig. 20B can be obtained by numerical analysis. Both collision probability curves shown in the figure have the same general behavior (increasing with electron velocity) and the same average magnitude, but it is apparent that there is a definite limit to the exact amount of velocity structure that can be determined when the experimental effective collision frequency is a function of electron temperature alone; i.e., for very low degrees of ionization. The extremes of the resulting uncertainty are represented by the two collision probability curves of Fig. 20B, and together they define the envelope indicated by the dotted line in the figure. The dominant feature of Curve a is its rapid increase with velocity at higher velocities, while that of Curve b is its rapid decrease at lower velocities. These features are of such a nature as to result in approximately the same effective collision frequency behavior in the range of electron temperatures of interest in this investigation when electron-ion effects are ignored. However, when it is required that these two functions satisfy experimental data for various degrees of ionization, this places additional requirements on the exact velocity structure of the collision probability as can be seen in Fig. 20C where the two collision probability curves are shown to yield significantly different behavior when electron-ion effects are included. Figure 20 illustrates the fact that the coupling between the experimental electron temperature range of this investigation and the electron velocity range of sensitivity is significantly strengthened by the fact that the normalized effective collision frequency is dependent on the degree of ionization as well as electron temperature. This results in a significant improvement in the ability of the technique to determine the velocity structure of the electron-atom collision probability.

#### Effect of Variation of Electron-Ion Collision Term

In order to determine the extent to which the calculated normalized effective collision frequency is affected by variations in the effective electron-ion cross-section term (Eqs. 7 and 8), a variety of modifications to both the magnitude and velocity dependence of this term were incorporated in Eq. 15 for the effective collision frequency. The effective collision frequency was calculated first assuming variation of approximately 50 to 100 per cent in the absolute magnitude of the constant associated with the electron-ion term. The velocity dependence of was also modified and numerical integrations performed. Electron-ion cross sections varying as  $v^{-7/2}$  and  $v^{-9/2}$  were used with a force fit to the standard  $v^{-8/2}$  term (Eqs. 7 and 8) at electron velocities of 0.35, 0.6, and  $0.85\sqrt{\text{eV}}$  which correspond to the low, medium, and high velocity ranges characteristic of the electron temperatures of this investigation. The variations in the calculated normalized effective collision frequency caused by such manipulation of the electron-ion term

are shown in Fig. 21. The solid lines in the figure are the same as those in Fig. 18 and represent the normalized effective collision frequency calculated using Eq. 15, the collision probability of Fig. 19, and the standard electron-ion collision cross section (Eqs. 7 and 8). The shaded areas represent the limits of the variation in the calculated effective collision frequency caused by alterations in the electron-ion cross section as described above. It is apparent from the figure that the resultant effect on the collision frequency is relatively small with neither the qualitative or quantitative behavior significantly altered. For reasonable variations in the electron-ion term, such behavior would be expected since electron-ion effects, although significant, do not dominate the collisional process for the degrees of ionization encountered in this experiment.

#### Limits of Uncertainty in the Collision Probability

The numerical procedures described in the preceding paragraphs have been used to establish the degree of uncertainty in the velocity structure of the collision probability resulting from variations in the theoretical expression for the effective collision frequency (Eq. 15); the over-all resolution of the "trial function" technique for the range of experimental variables covered in this investigation has also been considered. Various experimental checks (outlined in Section 3) were made to insure that the plasma diagnostic systems were reliable. Therefore, it is felt that the quantitative and qualitative behavior of the experimentally determined effective collision frequency data is correct. However, the possibility always exists that an undetectable systematic experimental error may result in an alteration in the slope, but not the magnitude, of the effective collision frequency. If this were the case, the absolute magnitude of  $\nu_{\text{eff}}^*$  would not be significantly affected. However, the exact velocity structure of the collision probability as determined from the integral analysis would be altered, particularly at the extremes of the velocity range of interest where the sensitivity of the technique begins to fade. In consideration of such a possibility, a variation of approximately 25 to 50 per cent in the slope of the effective collision frequency data of Fig. 15, equivalent to a variation of about 15 to 20 per cent in the experimentally determined magnitude of  $\nu_{\text{eff}}^*$ , has been taken into account when establishing the envelope of uncertainty for the collision probability velocity structure (dashed lines in Fig. 19). Such a variation is reasonable in view of the known limits of accuracy of the experimental techniques.

A family of collision probability curves which forms this envelope has been determined from an analysis of trial functions for  $Q_{\text{eq}}(v)$ . Each member of this family when averaged over all electron velocities yields a normalized effective collision frequency having the quantitative and general qualitative behavior of the  $\nu_{\text{eff}}^*$  data of Fig. 15 subject to the possibility of experimental error as described in the previous paragraph. The envelope (dashed lines in Fig. 19) has the same qualitative behavior as the collision probability curve yielding the best fit to the experimental data of this investigation (solid line in Fig. 19). However, it is apparent from the figure that the total increment of uncertainty

$(\Delta \rho_c)$  in the collision probability magnitude as defined by the envelope can be quite large, particularly at the extremes of the velocity range of sensitivity. This should not be interpreted as meaning that any collision probability curve falling within the envelope will, when averaged, satisfy the experimental data of this investigation. For example, an increase in the magnitude of the collision probability in the lower velocity range of sensitivity (0.4 to 0.5 eV) must be accompanied by a decrease at higher velocities such as to yield the same magnitude and approximately the same slope as the  $\nu_{eff}^*$  data of Fig. 15 when averaged over the electron velocity distribution. It should be noted that the collision probability of Fig. 19 is not experimental data but rather is based on the interpretation of experimental data. The range of uncertainty in the precise velocity structure of the collision probability, as determined from the analysis described above, is an indication of the possible variations associated with this interpretation and also indicates the importance of consistent and realistic interpretation of "average" or "effective" collision probability data determined from experimental measurements of over-all collisional effects in plasmas.

## 7. Conclusions

### Averaging of the Collision Frequency

The significance of the inclusion of a collision term to represent electron-ion interactions in the theoretical formulation of Section 2 is easily appreciated from the analysis of the experimental and theoretical data presented previously. However, the effect that differences in the averaging of the actual velocity dependent collision probability can have on plasma transport properties (the actual measurables in an experimental system) is not so obvious. The following example will illustrate this point. The effective electron-heavy particle collision frequency or resistive term for the dc flow of current through a homogeneous plasma was defined by Eq. 4 and can be written

$$\nu_{eff}^{-1}(dc) = \frac{8}{3\sqrt{\pi}} \left( \frac{m}{2kT_e} \right)^{\frac{5}{2}} \int_0^{\infty} \frac{v^4 e^{-\frac{mv^2}{2kT_e}}}{\nu_{eh}(v)} dv . \quad (25)$$

where  $\nu_{eh}(v)$  is the total electron heavy particle momentum transfer collision frequency. Subject to the same restricting assumptions pertinent to the derivation of Eqs. 4 and 25, an effective collision frequency can be defined for the case where the electric field is ac. If the square of the radian frequency of the electric field is much greater than the square of the electron heavy particle collision frequency ( $\omega^2 \gg \nu(v)^2$ ), a case often encountered in practice, an ac effective collision frequency can be defined

$$\nu_{eff}(ac) = \frac{8}{3\sqrt{\pi}} \left( \frac{m}{2kT_e} \right)^{\frac{5}{2}} \int_0^{\infty} \nu_{eh}(v) v^4 e^{-\frac{mv^2}{2kT_e}} dv , \quad (26)$$

which represents the over-all ac resistive effects due to collisional encounters between electrons and heavy particles. It is apparent from Eqs. 25 and 26 that, if expressions of this type are used without consideration for the differences in the averaging process, the resultant effective collision frequency will be dependent on the experimental techniques used in the measurements. For example, dc conductivity measurements can lead to an effective collision frequency given by Eq. 25, and microwave attenuation measurements can result in an effective collision frequency given by Eq. 26. Although an "average" collision frequency can be obtained in this manner, Eq. 25 and 26 illustrate that the resultant effective dc and ac collision frequencies do not represent the same average of collision frequency over electron velocities. That is, effective collision frequencies of the type defined by the preceding equations are not unique plasma parameters as is the actual velocity dependent collision frequency which depends on the properties of the atom representative of the scattering gas.

Often an effective collision probability is obtained indirectly from the measurement of plasma transport properties, which lead to an effective collision frequency, by normalizing the effective collision frequency with respect to atom density and dividing by the most probable or average electron velocity of a Maxwellian distribution. This approach, which relates the experimental measurable electron temperature to an electron velocity (Eq. 20), assumes that the heaviest weighting of the collisional process occurs very close to the peak of the distribution of the electron velocities. This assumption is not generally met in practice, particularly for low electron energies where the collision frequency may be a strong function of velocity over the range covered by the electron velocity distribution. As a consequence, the dc effective collision frequency (Eq. 25) would be the result of weighting the actual velocity dependent collision frequency most heavily at its minimum, and the ac effective collision frequency (Eq. 26) the result of weighting which places greatest emphasis on the velocity range where the actual collision frequency is a maximum.

Numerical calculations of the ac and dc effective collision frequency have been made using a variety of hypothetical collision probability curves similar to those presented in Fig. 16. The resulting differences in the effective collision frequencies were found to be as high as a factor of four; even the qualitative behavior of the effective collision frequencies was different in certain ranges of electron temperature. The effective collisional parameters defined by Eqs. 25 and 26 and a variety of other collisional parameters obtained from equations relating such plasma transport properties as conductivity directly to a collision probability are not unique plasma properties, but rather, are defined for convenience to represent the over-all effect of collisions on a particular measurement. Only in the case of nearly constant collision frequency ( $v^{-1}$  dependence of collision probability on electron velocity) do all the effective forms of the collision frequency reduce to approximately the same value and adequately represent the true electron heavy particle collision frequency.

### Analysis of Available Collision Probability Data

The apparent necessity of including electron-ion effects in the analysis of cesium plasmas in the ranges of electron temperature and degrees of ionization of practical interest and the importance of proper averaging of the electron-cesium heavy particle collision probabilities over electron velocities have prompted a re-evaluation of the available average cesium collision probability data reported in the literature. Of the available collision probability data (Fig. 1), only Refs. 2 and 3 attempted to determine the actual velocity dependent collision probability from an integral analysis. References 4 through 11, involving measurement of a variety of plasma transport properties, inferred an average collision probability from an effective collisional term similar to those described in the previous paragraphs. The average collision probability so determined was then plotted as a function of most probable or average electron velocity which is a function of electron temperature, an experimental measurable. In addition to the normal experimental error, the collision probability determined in this manner is subject to the uncertainties associated with the differences in averaging described in the previous paragraph. A considerable improvement in the understanding of the cesium collision probability data results if the available data is converted back into an effective collision frequency form and plotted as a function of electron temperature. This is accomplished by converting the velocity coordinate of each data point of Fig. 1 to an electron temperature through the use of Eq. 20. A normalized effective collision frequency is recovered by multiplying each collision probability data point by its corresponding most probable velocity point. This conversion process results in a presentation of the available experimental data in a form more closely associated with the manner in which the measurements were actually made.

Figure 22 presents the available experimental data (Refs. 2 through 11) in effective collision frequency form, the experimental data of this investigation, and numerically calculated normalized effective collision frequency extrapolated to lower and higher electron temperatures. Although the lowest electron temperature of the current investigation was approximately 2500°K, the integrated collision probability (effective collision frequency) can be numerically calculated for lower electron temperatures with reasonable safety, since at lower temperatures and degrees of ionization in the  $10^{-4}$  to  $10^{-3}$  range, electron-ion effects begin to dominate the collisional processes. The theoretical curve was obtained using Eq. 15 and the collision probability of Fig. 19. It is apparent from this figure that interpretation of the available cesium collision probability data on the basis of an effective collision frequency formulation which includes the effect of electron-ion collisions, produces a clearly definable qualitative and quantitative trend. The general agreement that results when the available data are analyzed on a common basis and compared with the numerically calculated effective collision frequency is further evidence of the importance of a consistent interpretation of experimental results and lends support to the validity of the collision probability curve resulting in the best fit to the data of this investigation (solid line in Fig. 19).

Extrapolation of Total Collision Probability Data

Additional evidence is available that the velocity dependent electron-caesium atom collision probability must drop to an average value considerably less than the value of 1400 collisions per cm per mm Hg suggested by Nottingham. In Fig. 23 is plotted a smooth extrapolation of Brode's<sup>1</sup> total collision probability data at the higher velocity end of the range of interest to the low velocity momentum transfer collision probability data of Refs. 2 and 3; the average value of the extrapolated portion is approximately 1400 collisions per cm per mm Hg. The integrated value of this extrapolated collision probability is compared in Fig. 24 with the effective collision frequency of Fig. 22. For electron temperatures above approximately 2000°K, the integrated extrapolated collision probability curves yield the same result whichever low velocity path is followed, Ref. 2 or Ref. 3. Upon examination of the figure, it is apparent that the normalized effective collision frequency of this example is considerably higher in magnitude than the collision frequency which results in the agreement between the data of this investigation and the data of Refs. 2 to 11 (Fig. 22). The difference in magnitude between the two sets of collision frequency curves varies from approximately a factor of 2 at the higher electron temperatures (5000°K) to as much as a factor of 5 for electron temperatures of about 1000°K. Since the  $\nu_{\text{eff}}^*$  data presented in Fig. 22, above an electron temperature of 1000°K, represents information obtained from nine different experimental efforts including the current investigation, it would seem reasonable to assume that at least the correct magnitude of the collision probability has been established. Consequently, a smooth extrapolation of Brode's data similar to that of Fig. 23 or the assumption of a constant average value of approximately 1400 collisions per cm per mm Hg could lead to considerable error in calculations pertaining to plasma transport properties.

Comparison of Theoretical and Experimental Collision Probability Data

Although even approximate theoretical calculations leading to the electron-caesium atom cross section are quite complicated, current interest has been stimulated by the practical application of ionized caesium vapor in devices such as the thermionic converter. It is of interest to analyze some of the more recent theoretical results in light of the conclusions drawn from the experimental and analytical work of this program. In Ref. 24 the total elastic scattering cross section for slow electrons from caesium atoms was calculated theoretically. Various experimental values for the polarizability were used, and the cutoff parameter, the distance at which the polarization-induced force disappears, was allowed to vary slightly. Consequently, three different theoretical cross sections were determined, and it was found that significant variations in the scattering curves are obtained for small changes in the cutoff parameter. However, it is interesting to note that, of the three curves calculated, two had very sharp resonances corresponding approximately to a collision probability of 3250 collisions per cm per mm Hg at the peak, which occurred at an electron velocity of approximately  $0.9\sqrt{eV}$ . The total and momentum transfer electron-caesium atom cross sections were calculated theoretically in Ref. 25. The resultant scattering



curves for both the total and the momentum transfer cases are similar. As in Ref. 24, the resultant theoretical curve exhibits a resonance behavior having a peak of 1800 collisions per cm per mm Hg at an electron velocity of approximately  $0.7\sqrt{\text{eV}}$  and a minimum of about 560 collisions per cm per mm Hg at  $0.25\sqrt{\text{eV}}$ . A more recent calculation (Ref. 26) of both the total and momentum transfer elastic scattering cross sections has resulted in an extremely sharp resonance in both cross sections at about  $0.5\sqrt{\text{eV}}$ . The magnitude of the momentum transfer cross section rises from a minimum of about 200 collisions per cm per mm Hg at  $0.35\sqrt{\text{eV}}$  to a maximum of 3300 collisions per cm per mm Hg at  $0.5\sqrt{\text{eV}}$ . In this case the resonance is shifted more towards lower electron velocities than in either of the previous two cases mentioned. However, the general qualitative behavior featuring a pronounced resonance is the same. The total and momentum transfer collision probabilities of Ref. 26 differ by as much as 100 per cent in the  $0.7$  to  $1.0\sqrt{\text{eV}}$  range, which indicates a significant angular dependence of the differential scattering cross section. Such behavior points out the possible error in the use of total collision probability data obtained from electron beam measurements to calculate plasma transport properties which depend on the momentum transfer collision probability.

The theoretical calculations of Refs. 24 to 26 are presented in Fig. 25 along with the collision probability determined from the experimental and analytical data of this program. It is apparent from the differences in the various theoretical curves and from examples treated in the original references that the collision probability is extremely sensitive to the theoretical form used to represent polarization effects. Consequently, a model which accurately describes the atomic polarization by the incident electron is a prerequisite for an accurate theoretical prediction of the elastic electron scattering cross section for cesium. However, the general form of the various theoretical scattering curves of Fig. 25 is the same and is in excellent qualitative and semi-quantitative agreement with the collision probability curve determined from this investigation. Of particular significance is the theoretical predication of a resonance in the  $0.5$  to  $1.0\sqrt{\text{eV}}$  range, coupled with a sharp drop to a minimum in the collision probability in the  $0.3$  to  $0.7\sqrt{\text{eV}}$  range of electron velocities. In Ref. 26, which is the most recent work and presumably an improvement over previous calculations, an average value of the polarizability was used which corresponds approximately to the average of the experimental values. However, numerical experimentation in Ref. 26 indicates considerable sensitivity to the exact choice of the polarizability. Although the general shape of the theoretical curve remains the same for slight variations in the polarizability, the location of the resonance can be shifted along the velocity scale. Since the range of maximum sensitivity of this investigation and the data of Refs. 4 through 11 corresponds to the velocity range where theory predicts a sharp dip in the collision probability, the analysis of the numerical and experimental data presented here indicates that the actual location of the collision probability minimum (approximately 100 to 300 collisions per cm mm Hg) is in the  $0.45$  to  $0.65\sqrt{\text{eV}}$  range of electron velocities with the indicated resonance occurring in the  $0.75$  to  $1.0\sqrt{\text{eV}}$  range.

## CESIUM ION-ATOM TOTAL COLLISION PROBABILITY MEASUREMENTS

## 8. Introduction

In order to obtain an insight into the mechanism responsible for the production of the non-equilibrium ionization which exists in the neutralization plasma of arc-mode thermionic converters, the loss rate of ions from the plasma must be accurately known. In diffusion-dominated plasmas the loss rate of ions is determined by their mobility. Preliminary measurements of the total collision cross section of cesium ions interacting with cesium atoms have been made over the energy range of 0.12 to 9.7 eV using a modified Ramsauer experiment under Contract NASr-112. The present investigations are extensions of this work to energies below 0.12 eV which is the energy range of most interest in the analysis of the neutralization plasma that exists in the converter. Knowledge of the cesium ion mobility provides an insight not only into the loss rate of ions from the plasma but also of the possible energy transfer mechanisms from the plasma to the emitter surface which can cause a significant change in the emitter surface work function.

Extrapolations of high-energy charge exchange information reported in the literature to the energy range of interest in the converter have been made by Sheldon.<sup>27</sup> These extrapolations, which have included approximations to account for polarization effects at energies below 1.0 eV, vary by as much as an order of magnitude. The lowest energy at which charge exchange cross sections have been measured using beam techniques is 6.0 eV (Ref. 28). Due to the nature of the experimental apparatus employed in these charge exchange measurements, no correction for contact potential effects could be made in these investigations. Therefore, the reported charge exchange cross-section information at an energy of 6.0 eV can be in serious error due to a large uncertainty in the determination of the energy of the ion beam. Other attempts have been made to determine cesium ion mobilities by observing the decay rate of the afterglow of a cesium plasma.<sup>29,30</sup> In these measurements no attempt was made to determine the nature of the ion energy distribution, and in some cases, the dominant ionic species existing in the plasma was not identified. In the present experiment, which uses a modified Ramsauer beam technique, contact potential effects have been eliminated from the measurement by employing an electroformed collision chamber. The energy, as well as the species of the ion beam interacting with the cesium atoms in the collision chamber, has been positively identified in these investigations. The one limitation of this measurement has been that the cross section determined by these techniques is a quasi total collision cross section which is dependent on the resolution of the system. However, completely classical techniques have been successfully used to analyze the total collision cross-section information to determine the magnitude of the charge exchange contribution. A paper outlining the results of this analysis and the cesium ion mobility determined on the basis of these results was presented at the IEEE Thermionic Conversion Specialist Conference held in Cleveland, Ohio, on October 26 to 28, 1964. One other essential feature that this analysis of the cross-section information has brought out is the importance of determining ion mobilities by integrating the diffusion cross section over the ion

energy distribution rather than using a value of the diffusion cross section which corresponds to the temperature of the ion energy distribution to determine ion mobility. In this report period further analysis of the available cross-section data has been conducted to take into account the energy resolution of the collision chamber and the effect of the finite velocity of the target gas atoms on the magnitude of the measured low-energy total collision cross-section information. Ion beam energy distributions were obtained down to energies of 0.107 eV and ion beams with energies as low as 0.058 eV were detected in the system. Attempts have been made in this period to measure the total collision cross section at energies below 0.1 eV, but due to problems encountered with control of the cesium pressure within the well, this information should be considered preliminary and should not be considered as a quantitative measurement of the true cross section existing at these energies.

## 9. Description of Experiment and Measurement Techniques

Beam techniques have been employed by many investigators to determine ion-atom collision probabilities. The most noteworthy of these measurements are the investigations conducted by Ramsauer,<sup>31</sup> the results of which are quoted in the English literature incorrectly. The use of beam techniques at energies less than several electron volts is seriously limited by uncertainties in the determination of the ion beam energy due to contact potential effects which are particularly severe in cesium environments. In this investigation, as in the earlier Ramsauer beam experiments, the total collision cross section is determined by measuring the attenuation of an ion beam of known energy produced by an increase in collision chamber neutral particle density. In the present cesium ion-atom total collision cross-section measurements, contact potential problems were eliminated by employing an electroformed collision chamber in which no metal interfaces exist that can give rise to possible contact potential effects. Shown in Fig. 26 is a schematic drawing of the system employed in these measurements. Cesium ions are produced by boiling cesium atoms through a porous tungsten cap which is maintained at a temperature of approximately 1200°C. Standard accelerating-decelerating ion optics are employed to extract ions from the porous cap. Two sets of deflection plates, one located immediately adjacent to the ion gun and the other located directly in front of the collision chamber entrance slit, are employed to align the ion beam with the collision chamber. A magnetic field applied perpendicular to the plane of the schematic is employed to energy-select ions produced on the porous tungsten cap. The collision chamber is designed so that the entrance and exit slits and the necked-down portion in the center of the collision chamber serve as three degrees of restraint which define the radius of a circle. The energy of the ion beam passing through the collision chamber is uniquely determined from a knowledge of chamber geometry and the magnitude of the applied magnetic field. Re-entry type entrance and exit slits are employed on the collision chamber to prevent external electric fields from penetrating into the chamber, which can seriously perturb ion trajectories. In these measurements the energy of the ion beam is uniquely determined only while the beam is within the collision chamber. Prior to entering the

chamber the beam energy can be significantly altered by the accelerating-decelerating optics system. Similarly once the beam exits the collision chamber, an accelerating plate is used to deflect the ion beam off its initial trajectory in the magnetic field and into an electron multiplier. Only a knowledge of the energy of the ion beam while it is in the collision chamber is essential in the measurement. The measured total collision cross section is composed of elastic scattering events that produce deflections of the ion beam greater than 0.0074 radians and essentially all charge exchange interactions. All charge exchange collisions are measured in this system because the newly formed ions produced by the interaction have incorrect trajectories in the magnetic field to exit the chamber. The attenuation of the ion beam can be predicted by

$$I = I_0 e^{-P_0 P_t x} \quad (27)$$

where

- I is the ion beam current exiting the collision chamber for a finite pressure in the chamber
- $I_0$  is the ion beam current exiting the collision chamber for zero pressure in the chamber
- $P_0$  is the pressure in the collision chamber reduced to 273°K
- $P_t$  is the number of collisions per cm of path per mm of pressure
- x is the path length of the ion beam through the chamber.

The total collision cross section is determined by gradually increasing the cesium pressure in the collision chamber and measuring the number of particles missing from the ion beam produced by the increase in chamber pressure. The length of the collision chamber was chosen so that the operating cesium pressure in the chamber ranged from  $10^{-7}$  to  $10^{-5}$  mm Hg. Therefore, at this pressure level the exit and entrance slits on the collision chamber were always operating in the free molecular flow regime. The operating pressure range of the vacuum system in the multiplier was always several orders of magnitude lower than the cesium pressure in the chamber so that additional collision events produced by interactions of the ion beam with the background gas in the system could not produce spurious results. As Eq. 27 indicates, the cross section can be determined by making a relative measurement of the attenuation of the ion beam intensity and an absolute measurement of the cesium pressure existing in the collision chamber.

#### Method of Determining Ion Beam Energy

As it has been outlined in the previous section, the ion beam energy is determined uniquely in these measurements from the radius of curvature determined by the geometry of the electroformed collision chamber and the magnitude of the applied magnetic field. Since the collision chamber slits have a finite width, the ion beam focused through the collision chamber has a finite energy width. For the collision chamber used in these investigations, the geometrical energy resolution of the chamber is essentially the center energy  $E \pm \Delta E$ , where  $\Delta E$  is approximately  $\pm 8$  per cent

of the center energy  $E$ . Shown in Figs. 27 through 33 are typical ion beam distributions obtained with this system. Shown in Fig. 34 is a comparison between theoretically calculated and experimentally measured ion beam energies at half-width. As can be seen from this figure, the agreement between theory and experiment is extremely good. The determination of the absolute magnitude of the ion beam energy is dependent upon the absolute magnitude of the applied magnetic field and the geometry of the collision chamber.

The collision chamber geometry is determined by making careful measurements prior to plating of the dimensions of the aluminum mandrel over which the copper collision chamber is electroformed. These measurements include shadowgraphing the shape of the mandrel so that the thickness of the copper plate can be determined absolutely upon completion of the electroforming of the chamber. After the aluminum mandrel is removed with caustic solutions from the electroformed chamber, X-rays are taken to determine the actual build-up of copper in various portions of the chamber and also to inspect the chamber for possible traces of aluminum from the mandrel which have not been entirely removed by the caustic solutions. Shown in Fig. 35 is a typical X-ray obtained of an electroformed collision chamber. As can be seen in this figure, the width of the collision chamber slits is clearly defined as is the width of the necked-down portion in the center of the chamber. Excellent agreement has been obtained between the width of the necked-down portion determined by measuring the thickness of the aluminum mandrel prior to plating and the thickness of this portion determined from X-ray measurements.

Hall probes were used to align the Helmholtz coils employed to generate the magnetic field in these measurements. To insure that proper alignment was achieved between the coils and the collision chamber, a jig which represented the trajectory of the ion beam within the collision chamber was mounted in the vacuum tank. Hall probes were positioned along the jig to determine the magnetic field intensity at various locations along the ion beam trajectory. The spatial resolution of probes employed in these measurements was one eighth of an inch. This is large in comparison to the finite slit width of the chamber which runs from 0.020 to 0.030 of an inch depending upon the particular chamber employed in the measurements. However, Hall probes were used to determine the average field and for alignment purposes since it was not anticipated that a widely diverging magnetic field would be produced by the Helmholtz coil configuration and since magnetic materials were eliminated from the critical regions of the experiment. The absolute magnitude to which the Hall probes could be calibrated over the range from approximately 50 to 700 gauss was  $\pm 3$  per cent. To increase the accuracy of the absolute measurements of the magnetic field, a rotating field gauss meter was employed. The absolute accuracy of this system was  $\pm 0.1$  per cent or 2 gauss. The accuracy of the rotating field gauss meter at low magnetic fields was improved by employing a null balance technique with a galvanometer to determine the magnitude of the field. The rotating field gauss meter was calibrated against a 100-gauss laboratory standard which had an accuracy of  $\pm 1$  gauss at 100 gauss. The rotating field gauss meter coil employed in these measurements encompasses a volume with a total diameter of 0.125 in. As has been previously indicated, only the magnetic field along the trajectory of the

ion beam within the collision chamber is essential in the determination of ion beam energies. The accuracy of the determination of the center line energy from these calibrations is  $\pm 2$  per cent at 0.21 eV. The radial variation in the magnetic field across the ion beam trajectory was measured and found to vary by 0.3 per cent. A typical magnetic field calibration is shown in Fig. 36.

The most important aspect of the determination of the ion beam energy in this system which makes it unique in comparison to other techniques is the use of an electroformed collision chamber to eliminate uncertainties in the energy determination produced by contact potential effects. Contact potential effects produced by preferential adsorption of cesium on electrode surfaces can significantly change the work functions of these surfaces, thereby producing large uncertainties in ion beam energy if retarding potential techniques are used.

Shown in Fig. 38 is a comparison of ion beam energies determined by using electroformed collision chamber techniques with energies determined using essentially retarding potential techniques. In this figure the results for two different experimental conditions are presented. For one set of measurements, which are represented by circular data points, the variation in the energy of the ion beam determined from the potential applied to the ionizer cap to the energy of the beam determined from the magnetic field energy analysis is approximately 0.25 eV across the entire energy range. By maintaining all conditions constant in the experiment and changing the cesium feed rate to the ionizer cap surface, thereby reducing the work function, the difference in the energy determined by the two techniques is once again constant but in this case is displaced by approximately 2.5 eV. This data is represented by the triangular points in Fig. 37. The effect of contact potentials which is so vividly illustrated by these results can be responsible for the wide discrepancy in cross-section information obtained by beam techniques at energies below 10.0 eV.

#### Cross-Section Determinations

The method employed to determine total collision cross sections in these investigations is to increase the cesium pressure in the collision chamber by increasing the temperature of the cesium well. Accurate control and correct determination of the cesium well temperature is one of the most difficult aspects of the experiment. From cross-section measurements with target gases, such as argon and nitrogen, it was found that the response time of the ion beam attenuation to changes in collision chamber pressure was essentially instantaneous. In the cesium measurements the pressure of cesium in the upper collision chamber was determined by measuring the temperature of the coldest spot in the cesium reservoir. The cesium reservoir system is shown schematically in Fig. 38. Both a copper baffle and a copper bottom were employed in the cesium reservoir design in an attempt to insure that the cesium would be located on the bottom of the reservoir. The stainless steel walls of the reservoir were heated by conduction from the copper blocks which were used to maintain the copper electroformed collision chamber at a temperature which was 100°C hotter than the reservoir. Detailed temperature profiles taken on this system indicated that the coldest location in the reservoir was the copper bottom. Thermocouples were buried

approximately 0.125 in. below the surface of the copper so that an accurate measurement of the cesium temperature in the reservoir could be obtained. The two thermocouples located on the bottom of the reservoir were calibrated by measuring inlet and outlet temperature of the cooling water of the reservoir under conditions where other thermal fluxes incident upon the system were negligible. It was felt that the accuracy of the measurements of these two thermocouples was within  $1^{\circ}\text{C}$ . In all cross-section measurements the temperature of the cooling water around the cesium reservoir was changed slowly, and the attenuation of the ion beam was measured as a function of reservoir temperature. Several experimental runs have been made in an attempt to determine the rate at which the pressure changes in comparison to the rate at which a temperature change occurs in the cesium reservoir. To date, for the measurements that have been conducted with this system, it appears conclusive that the rate at which the pressure change occurs is short in comparison with the time that ion cross-section information is obtained. To insure that the measurements are completely reversible and that the incident ion beam has not changed for reasons other than an increase in the pressure in the collision chamber, a comparison of the initial ion beam current to the final ion beam current once the cesium pressure has been reduced in the system is always made. As can be seen from the typical ion beam attenuation curve shown in Fig. 39, more than one pressure point is used to determine the actual value of the cross section. When counting equipment is not required, a minimum of at least 10 pressure points are used to determine a cross section. With counting equipment, which is used only at low ion beam current levels, three to five points are used in the determination of the cross section. This significant reduction in the number of ion current attenuation points is caused by the fact that the time required to obtain these points starts to become comparable with stability times of the system. From this data curve it can be seen that the ion beam attenuation does not exhibit an exponential behavior near zero pressures. This was due to the fact that there was a secondary cesium well produced by a cool spot located on the sidewall of the stainless steel cesium reservoir system. In an attempt to eliminate this problem in the most recent measurements, a copper baffle, as shown in Fig. 38, was inserted between the stainless steel sidewalls of the system and the main portion of the cesium reservoir. The temperature at the lower edge of this baffle was maintained at approximately  $30^{\circ}\text{C}$  above the cesium reservoir temperature to insure that secondary cesium wells that could possibly form on the reservoir walls could not give rise to spurious ion attenuation curves. Also to insure that the coldest spot in the reservoir was located at the bottom rather than on the sidewalls, copper which has excellent heat transfer characteristics in comparison to stainless steel was substituted for the original material in the bottom of the reservoir. Cesium pressure was determined from the vapor pressure curves of Ref. 32.

#### 10. Analysis of Cross-Section Data

Since ion-atom cross sections at thermal energies are being measured, the experimental results can no longer be interpreted in terms of a monoenergetic beam of ions interacting with a gas of fixed target atoms.

A computer program has been written which extracts the total ion-atom cross section from the average cross section as measured in the modified Ramsauer experiment. The experimentally measured cross section is really the true cross section as a function of relative velocity of the interacting particles,  $Q(V_r)$ , averaged over the velocity distributions of the beam particles  $f_b(V_b)$ , of the gas atoms  $f_g(V_g)$  and over the ratio of the relative velocity of the encounter to the beam particle velocity,  $V_r/V_b$ . The last term,  $V_r/V_b$ , converts the number of collisions per second to the number of collisions per unit path length of the ion beam. Therefore, the averaged cross section is given by

$$\overline{Q \frac{V_r}{V_b}} = \frac{\int f_b(V_b) f_g(V_g) \frac{V_r}{V_b} Q(V_r) d^3 V_g d^3 V_b}{\int f_b(V_b) f_g(V_g) d^3 V_g d^3 V_b} \quad (28)$$

which is similar to a form derived by Berkling, et al.<sup>33</sup> By assuming a true cross section of the form  $Q(V_r) = \alpha/V_r^\beta$  and knowing  $f_b(V_b)$  and  $f_g(V_g)$ , a double numerical integration may be performed for a particular  $\beta$  giving  $\overline{Q}$  in terms of  $\alpha$ . The  $\alpha$  may then be adjusted to give the least squares fit of  $Q$  to the experimental data. Computing  $\overline{Q}$  for a series of  $\beta$ 's, a best least squares fit may be obtained. This gives the best over-all values for  $\alpha$  and  $\beta$  or equivalently the best true cross section  $Q(V_r) = \alpha/V_r^\beta$ .

Since the slits on the collision chamber have a finite width, a range of ion velocities pass through the chamber for any applied magnetic field. A calculation based on the geometry of the collision chamber shows that the window for ion velocities is from  $0.96 V_c$  to  $1.04 V_c$ , where  $V_c$  is the velocity of the particle which moves through the centers of the three slits, that is, on a radius of 7.63 cm. Therefore, the size of the window is directly proportional to the center velocity of the beam. The limits of the window are used as the limits of integration for the component of the velocity in the direction of the beam current.

The ion beam is formed in an accelerating-decelerating-focusing system which is space-charge limited. Depending on whether the ions in the beam have enough time to thermalize, the velocity distribution function of the beam may range from an accelerated half-Maxwellian<sup>34</sup> to a Maxwell-Boltzmann distribution moving with a drift velocity. Based on the estimated ion number density in the beam of  $10^6$  to  $10^8/\text{m}^3$ , and an ion temperature of 0.1 eV, a thermalization time of about  $10^{-1}$  to  $10^{-3}$  sec may be calculated from Spitzer's formula.<sup>35</sup> The ions in the beam spend from  $10^{-2}$  to  $10^{-3}$  sec in transit through the 10 cm path length of the collision chamber. For these conditions at least some thermalization should be expected. The beam distribution may also be affected by space-charge effects and by high thermal velocities parallel to the magnetic field removing some ions from the beam. Ion beam current distributions were calculated on the basis of an accelerated half-Maxwellian and also on the basis of a Maxwellian moving with a drift velocity. By varying the limits of integration, plots of beam current as a function of energy were obtained for various center energies.



Comparing the energy widths at half height of the ion current distribution with the experimentally measured half-widths, it was observed that the accelerated half-Maxwellian gave a much closer fit to the experimental data than did the drifting Maxwellian which gave half-widths much too wide. The results which indicate that the accelerated half-Maxwellian should be used as the beam distribution function in this case are presented in Fig. 34.

$\bar{Q}$  was calculated for a series of  $\beta$ 's. In all these calculations,  $f_g(v_g)$  was assumed to be a Maxwellian distribution at the temperature of the collision chamber and the beam distribution was assumed to be an accelerated half-Maxwellian. The value of  $\beta$  which gave the best least squares fit to the experimental data was 0.76; the  $\alpha$  at this point was  $7.16 \times 10^5$ . Therefore, the cross section which best describes the experimental data on the basis of this analysis is

$$Q(v_r) = \frac{7.16 \times 10^5}{v_r^{0.76}} \text{ \AA}^2 \quad (29)$$

The results of this analysis are presented in Fig. 40.

## 11. Measurements and Results

Further measurements of low-energy total cesium ion-atom collision cross sections have been obtained with the new cesium reservoir. Modifications were made in the original reservoir system since detailed temperature profiles indicated that a localized cold spot existed on the walls of the reservoir. This cold spot produced a secondary cesium well which resulted in a nonexponential attenuation of the ion beam for low cesium pressures in the collision chamber, as shown in Fig. 39. The purpose of the copper baffle located in the lower portion of the new cesium reservoir and the copper bottom in the reservoir, as shown in Fig. 38, was to suppress the effects of secondary wells that could possibly form on the walls of the reservoir by virtue of the fact that the baffle was operated at a higher temperature than the walls of the reservoir and that the bottom was the coldest portion of the reservoir due to improved heat transfer properties of the copper. Even though the temperature profiles obtained with this new cesium reservoir design were much more uniform and the surroundings of the main portion of the reservoir were at an elevated temperature in comparison to the bottom of the reservoir, problems were still encountered with cesium being trapped in the feed line which was located behind the baffle. As a result, an uncertainty exists in the determination of the absolute neutral cesium pressure in the collision chamber for the most recent low-energy cross-section data obtained. As would be expected theoretically, with decreasing ion beam energy the measured total collision cross section increased. Shown in Fig. 41 is a comparison of this new data to information obtained previously with an all-stainless steel reservoir system. Even though the new cross-section information appears consistent with the previously obtained data, this new information should only at best be

considered quantitative due to possible pressure uncertainties that can exist in the reservoir system. This uncertainty in the absolute magnitude of the cross-section information produced by the uncertainty associated with the determination of the absolute cesium pressures in the collision chamber is reflected in the wide range of scatter in the data obtained at energies near 1.4 eV.

Shown in Figs. 27 to 33 are typical ion beam distributions measured at energies below 3.0 eV. Shown in Fig. 27 is an ion beam energy distribution obtained at an energy of 0.107 eV. This distribution was obtained with a new multiplier of the same design employed previously but of somewhat better construction. Being able to obtain this ion beam distribution is a direct result of the improvements made in the optics of the system and the fact that the whole experiment is now isolated from floor vibration which appears as low-frequency noise to the detection system. The minimum ion beam energy distribution obtained in this system was 0.107 eV. To obtain this energy distribution, ion beams with energies as low as 0.058 eV were focused through the collision chamber. The limiting parameter in obtaining low energy distributions is the temperature of the ionizer cap which determines the energy distribution of ions formed by contact processes on this surface.

The results of an analysis of the earlier cross-section information in which the distribution functions of both the ion beam and the neutral particle distribution are taken into account are shown in Fig. 41. The most significant result of this analysis is that at low energies, on the order of 0.12 eV, the true cross section determined from the low-energy measurements is really at relative energies of 0.16 eV.

Outline of Research for the Next Six-Month Period

1. Equipment will be set up to measure the total collision cross section of electrons interacting with cesium atoms over the energy range of 0.5 to 2.5 eV.
2. Experiments will continue to refine and further analyze the low-energy cesium ion-atom cross-section information.

# REFERENCES

1. R. Brode, Phys. Rev. 36, 673 (1929).
2. C. L. Chen and M. Raether, Phys. Rev. 128, 2679 (1962).
3. R. K. Flavin and R. G. Meyerand, Jr., Proceedings of the IEEE Thermionic Conversion Specialist Conference, Gatlinburg, Tennessee (1963).
4. G. L. Mullaney and N. R. Dibelius, ARS Journal 1575 (November, 1961).
5. D. Roehling, Symposium on Thermionic Power Conversion, Colorado Springs, Colorado, (May, 1962).
6. J. Bohdansky and R. Langpape, Sixth International Conference on Ionization Phenomena in Gases, Paris, Vol. IV, 543 (1963).
7. D. N. Mirlin, G. E. Pikus, and V. G. Yur'ev, Sov. Phys.-Tech. Phys. 7, 559 (1962).
8. L. P. Harris, J. Appl. Phys. 34, 2958 (1963).
9. C. Boeckner and F. L. Mohler, BSJR 10, 357 (1933).
10. J. C. Terlouw, personal communication.
11. N. D. Morgulis, and Yu. P. Korchevoi, Zhurnal Technicheskoi Fiziki 32, 900 (1962).
12. H. Margenau, Phys. Rev. 69, 508 (1946).
13. H. Dreicer, Phys. Rev. 117, 343 (1960).
14. D. H. Sampson and J. Enoch, Phys. of Fluids 6, 28 (1963).
15. D. J. Rose and M. Clark, Jr., "Plasmas and Controlled Fusion" published jointly by the M.I.T. Press and J. Wiley and Sons (1961), Chapter 8.
16. E. C. Lary and R. A. Olson, Rev. of Sci. Instr. 33, 1350 (1962).
17. E. C. Lary and R. A. Olson, AIAA Journal 1, 2513 (1963).
18. J. B. Taylor and I. Langmuir, Phys. Rev. 51, 753 (1937).
19. J. F. Waymouth, J. App. Phys. 30, 1404 (1959).
20. R. H. Bullis and W. J. Wiegand, Proceedings of the Twenty-third Annual Conference on Physical Electronics at M.I.T. (1963).

21. J. F. Waymouth, Phys. of Fluids 7, 1843 (1964).
22. R. S. Cohen, L. Spitzer, Jr., and P. McR. Routly, Phys. Rev. 80, 230 (1950).
23. R. H. Bullis and W. J. Wiegand, Proceedings of the Twenty-fourth Annual Conference on Physical Electronics at M.I.T. (1964).
24. W. R. Garrett and R. A. Mann, Phys. Rev. 130, 658 (1963).
25. P. M. Stone and J. R. Reitz, Phys. Rev. 131, 2101 (1963).
26. J. C. Crown and A. Russek, Phys. Rev. 138, A669 (1965).
27. J. W. Sheldon, "Mobility of Positive Ions in Their Own Gas: Determination of Average Momentum-Transfer Cross Sections" NASA Technical Note D-2408, August, 1964.
28. E. M. Kushnir, B. M. Palyukh, and L. A. Sena, Bulletin of the Academy of Sciences, USSR (Physics Series) 23, 995 (1959).
29. C. L. Chen and M. Raether, Phys. Rev. 128, 2679 (1962).
30. L. M. Chanin and R. D. Steen, Phys. Rev. 132, 2554 - 2557 (1963).
31. C. Ramsauer and O. Beeck, Ann. Physik 87, 1 (1928).
32. W. B. Nottingham, M.I.T. Research Laboratory of Electronics, Quarterly Progress Report No. 58, July 15, 1960.
33. K. Beakling, R. Helbing, K. Kramer, H. Pauly, Ch. Schlier, and P. Toschek, Zeit. fur Physik 166, 406 (1962).
34. P. A. Lindsay, "Velocity Distribution in Electron Streams," ADVANCES IN ELECTRONICS AND ELECTRON PHYSICS XIII, (Edited by L. Marton, Academic Press, New York, 1960).
35. L. Spitzer, Jr., PHYSICS OF FULLY IONIZED GASES (Interscience Publishers, New York, 1962), Chapter 5.

## LIST OF FIGURES

- Fig. 1 - Experimentally Determined Average Electron-Cesium Atom Collision Probability Variation with Average Electron Velocity
- Fig. 2 - Effective Electron-Ion Collision Cross-Section Variation with Electron Velocity
- Fig. 3 - Cesium Discharge Tube
- Fig. 4 - Schematic of Movable Electrostatic Probe Sidearm Assembly
- Fig. 5 - Cesium Discharge Tube with Conductivity Probe
- Fig. 6 - Anode Region of Cesium Discharge Tube with Conductivity Probe
- Fig. 7 - Calibration of R.F. Conductivity Probe Using Standard Electrolytic Solutions
- Fig. 8 - Variation of Averaged Plasma Conductivity with Discharge Current
- Fig. 9 - Typical Semi-log Plot of Electrostatic Probe Current Voltage Characteristic
- Fig. 10 - Variation of Electron Density with Radial Position
- Fig. 11 - Variation of Electron Temperature with Discharge Current and Pressure
- Fig. 12 - Variation of Electric Field with Discharge Current and Pressure
- Fig. 13 - Variation of Electron Density with Discharge Current and Pressure
- Fig. 14 - Variation of Degree of Ionization with Discharge Current and Pressure
- Fig. 15 - Experimentally Determined Normalized Effective Electron Cesium Heavy Particle Collision Frequency Variation with Electron Temperature and Degree of Ionization
- Fig. 16 - Illustration of Typical Trial Functions for the Electron-Cesium Atom Momentum Transfer Collision Probability
- Fig. 17 - Normalized Effective Collision Frequency Calculated Using Equation 15 and the Trial Functions for the Collision Probability Shown in Figure 16
- Fig. 18 - Comparison of Experimentally Determined and Numerically Calculated Normalized Effective Collision Frequency

- Fig. 19 - Electron-Cesium Atom Momentum Transfer Collision Probability Determined from an Analysis of the Experimental and Numerical Normalized Effective Collision Frequency Data
- Fig. 20 - Illustration of the Improvement in Resolution of Collision Probability Velocity Structure through Dependence of Effective Collision Frequency on Degree of Ionization
- Fig. 21 - Illustration of the Sensitivity of the Calculated Effective Collision Frequency to Variations in the Velocity Dependence and Magnitude of the Effective Electron-Ion Cross Section
- Fig. 22 - Normalized Effective Collision Frequency from References 2 to 11 Compared with UAC Experimental Data and Effective Collision Frequency Calculated Using Equation 15 and the Collision Probability of Figure 19
- Fig. 23 - Electron-Cesium Atom Collision Probability Variation with Electron Velocity
- Fig. 24 - Normalized Effective Collision Frequency Calculated Using the Extrapolated Collision Probability of Figure 23 Compared with the Collision Frequency Data of Figure 22
- Fig. 25 - Theoretically Calculated Electron-Cesium Atom Collision Probability Compared with Collision Probability Data of this Investigation
- Fig. 26 - Schematic Diagram of Ion Collision Cross-Section Apparatus
- Fig. 27 - Normalized Ion Beam Energy Distribution 0.107 eV
- Fig. 28 - Normalized Ion Beam Energy Distribution 0.88 eV
- Fig. 29 - Normalized Ion Beam Energy Distribution 0.97 eV
- Fig. 30 - Normalized Ion Beam Energy Distribution 1.14 eV
- Fig. 31 - Normalized Ion Beam Energy Distribution 1.40 eV
- Fig. 32 - Normalized Ion Beam Energy Distribution 2.36 eV
- Fig. 33 - Normalized Ion Beam Energy Distribution 2.59 eV
- Fig. 34 - Ion Beam Half-Widths
- Fig. 35 - X-ray of Electroformed Collision Chamber
- Fig. 36 - Magnetic Field Calibration

Fig. 37 - Variation of Applied Cap Potential with Measured Ion Energy

Fig. 38 - Cesium Reservoir

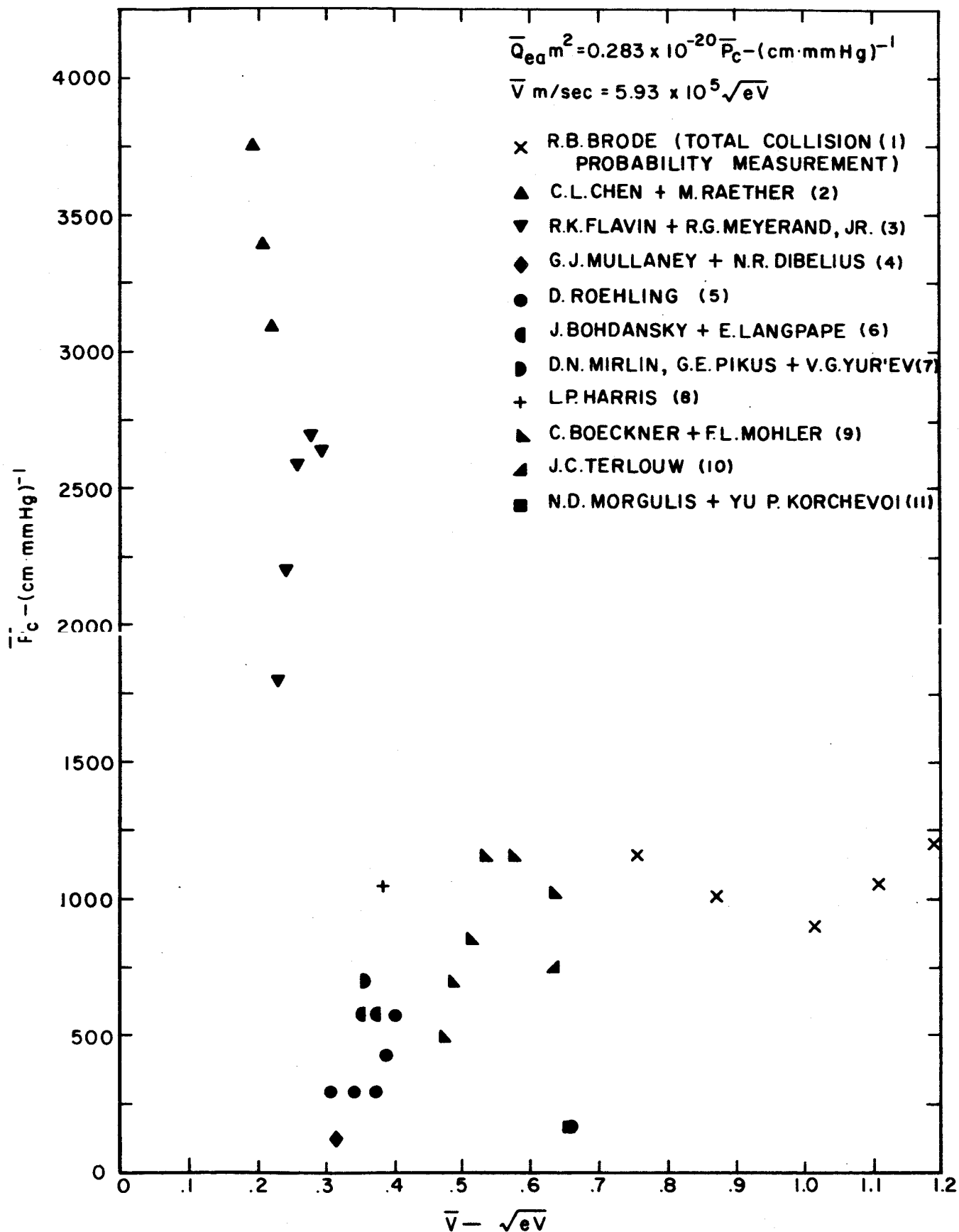
Fig. 39 - Typical Ion Beam Attenuation with Increasing Collision Chamber Pressure

Fig. 40 - Total Collision Cross Section

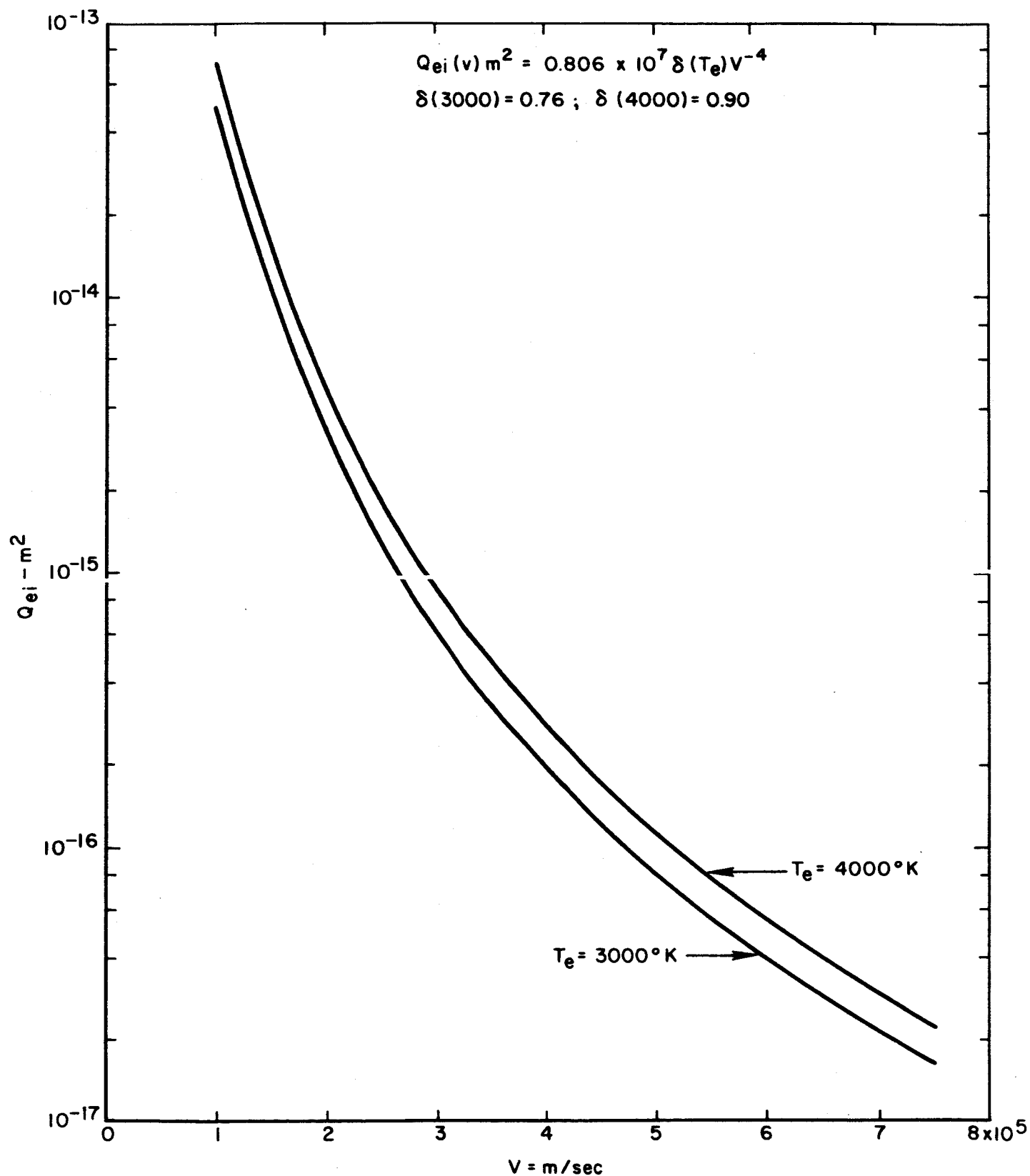
Fig. 41 - Comparison of Current Data and Previously Reported Data



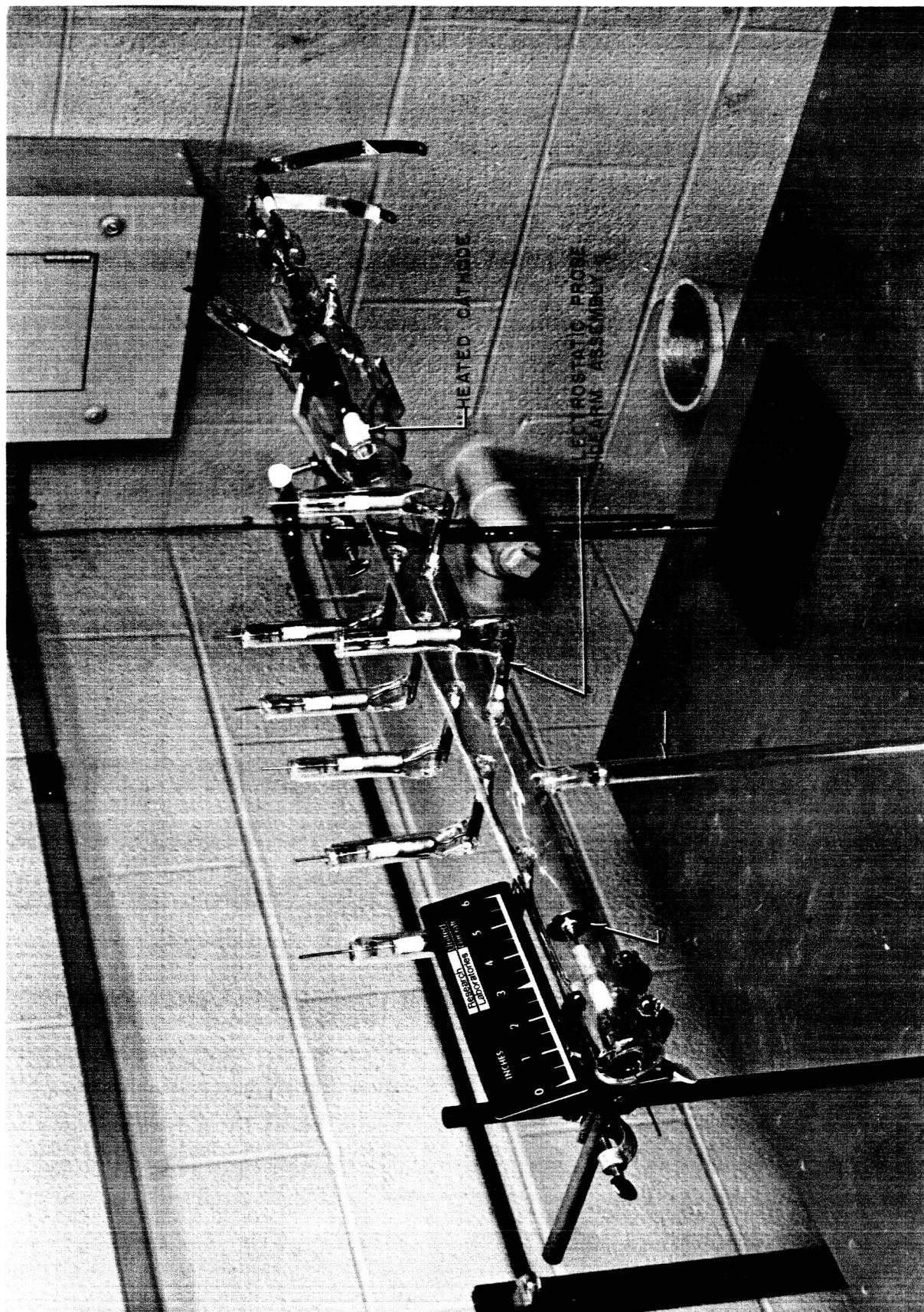
# EXPERIMENTALLY DETERMINED AVERAGE ELECTRON-CESIUM ATOM COLLISION PROBABILITY VARIATION WITH AVERAGE ELECTRON VELOCITY



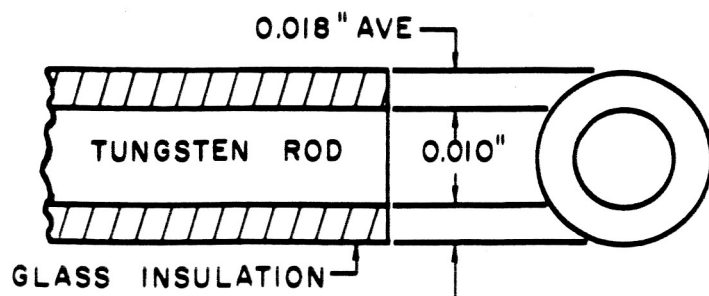
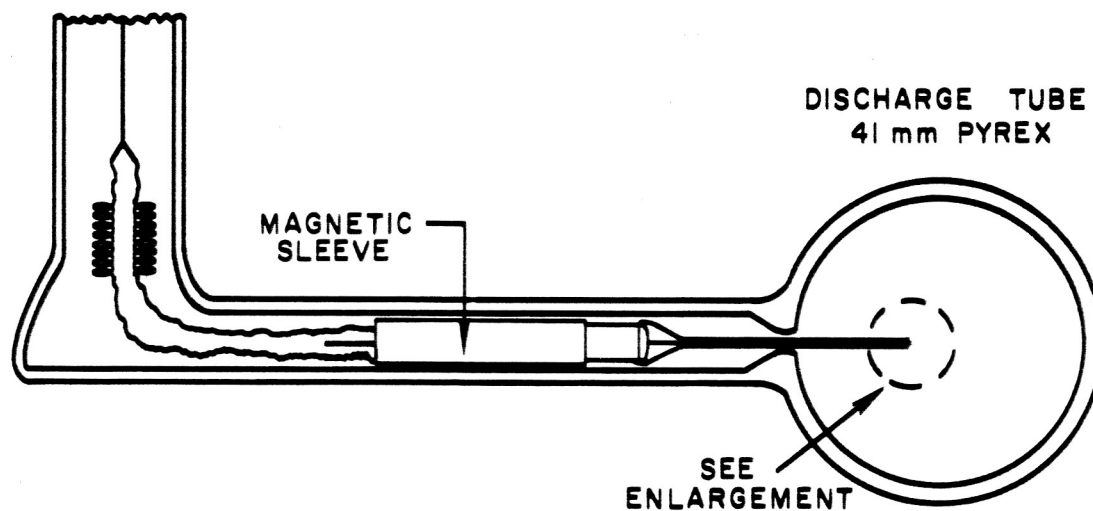
# EFFECTIVE ELECTRON-ION COLLISION CROSS SECTION VARIATION WITH ELECTRON VELOCITY



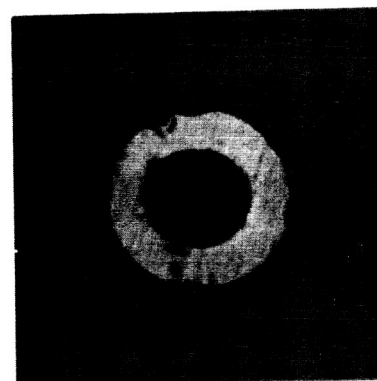
CESIUM DISCHARGE TUBE



# SCHEMATIC OF MOVABLE ELECTROSTATIC PROBE SIDEARM ASSEMBLY

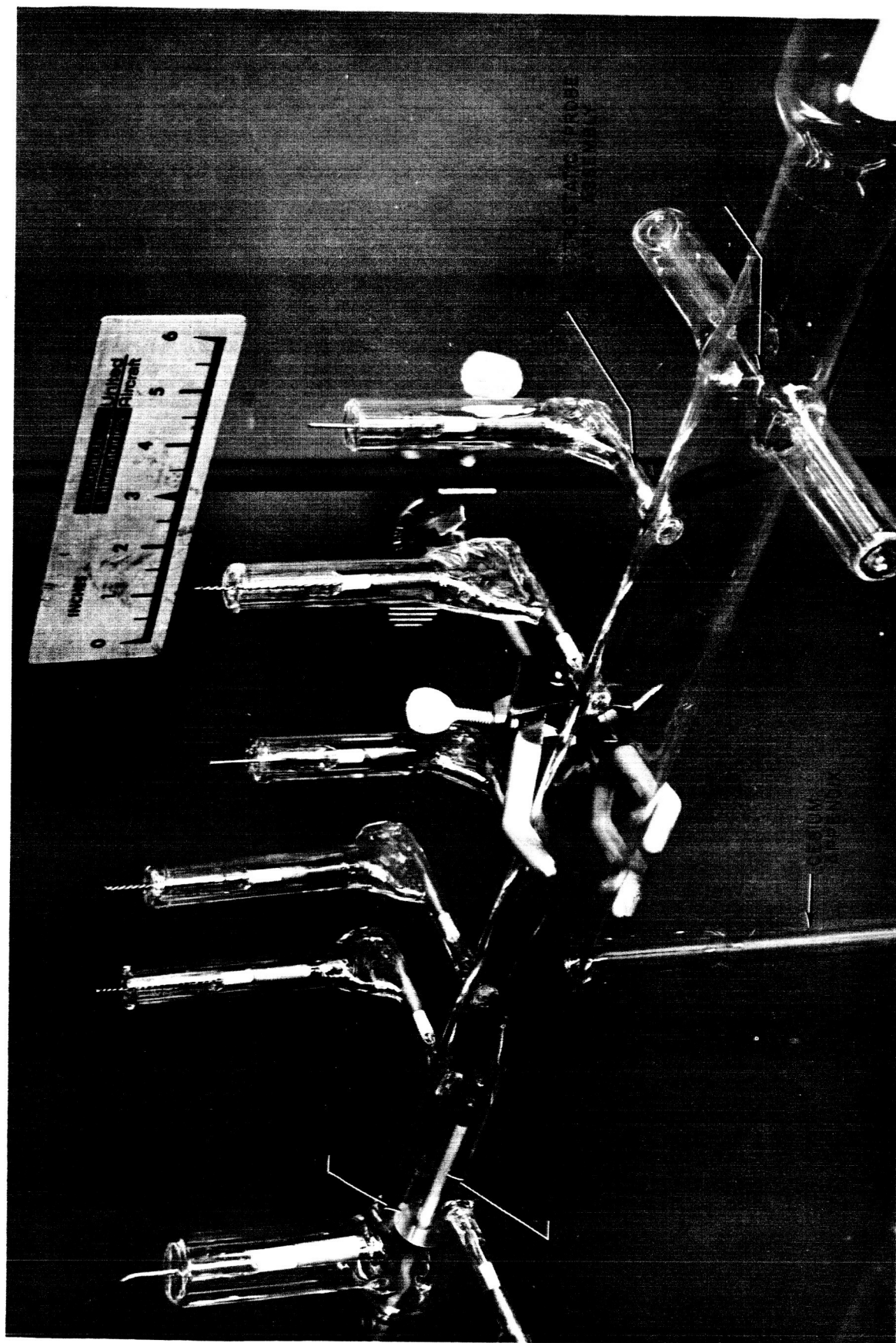


ENLARGEMENT OF ELECTROSTATIC  
PROBE TIP



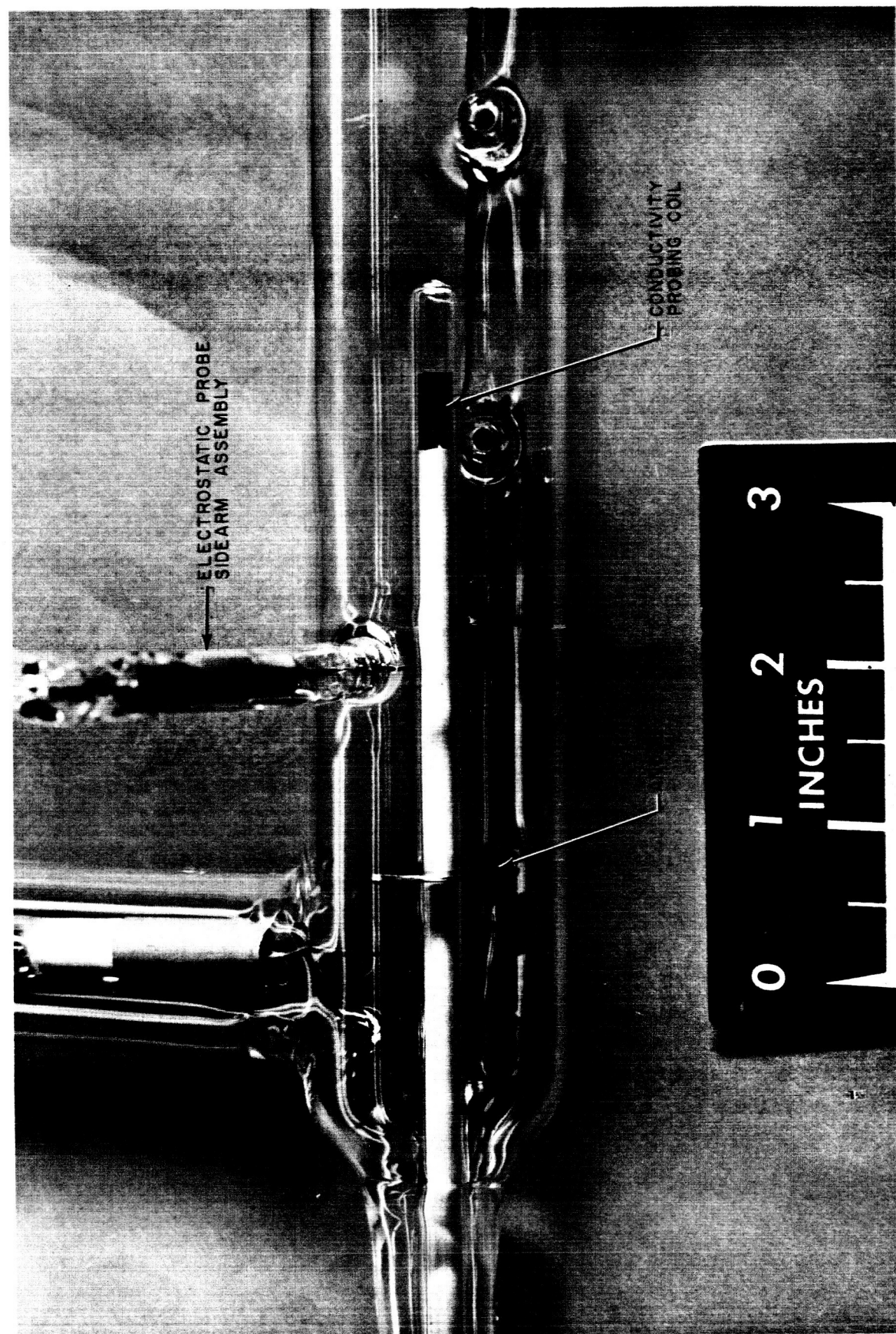
END VIEW OF PROBE  
MAGNIFICATION: 50 X

CESIUM DISCHARGE TUBE WITH CONDUCTIVITY PROBE

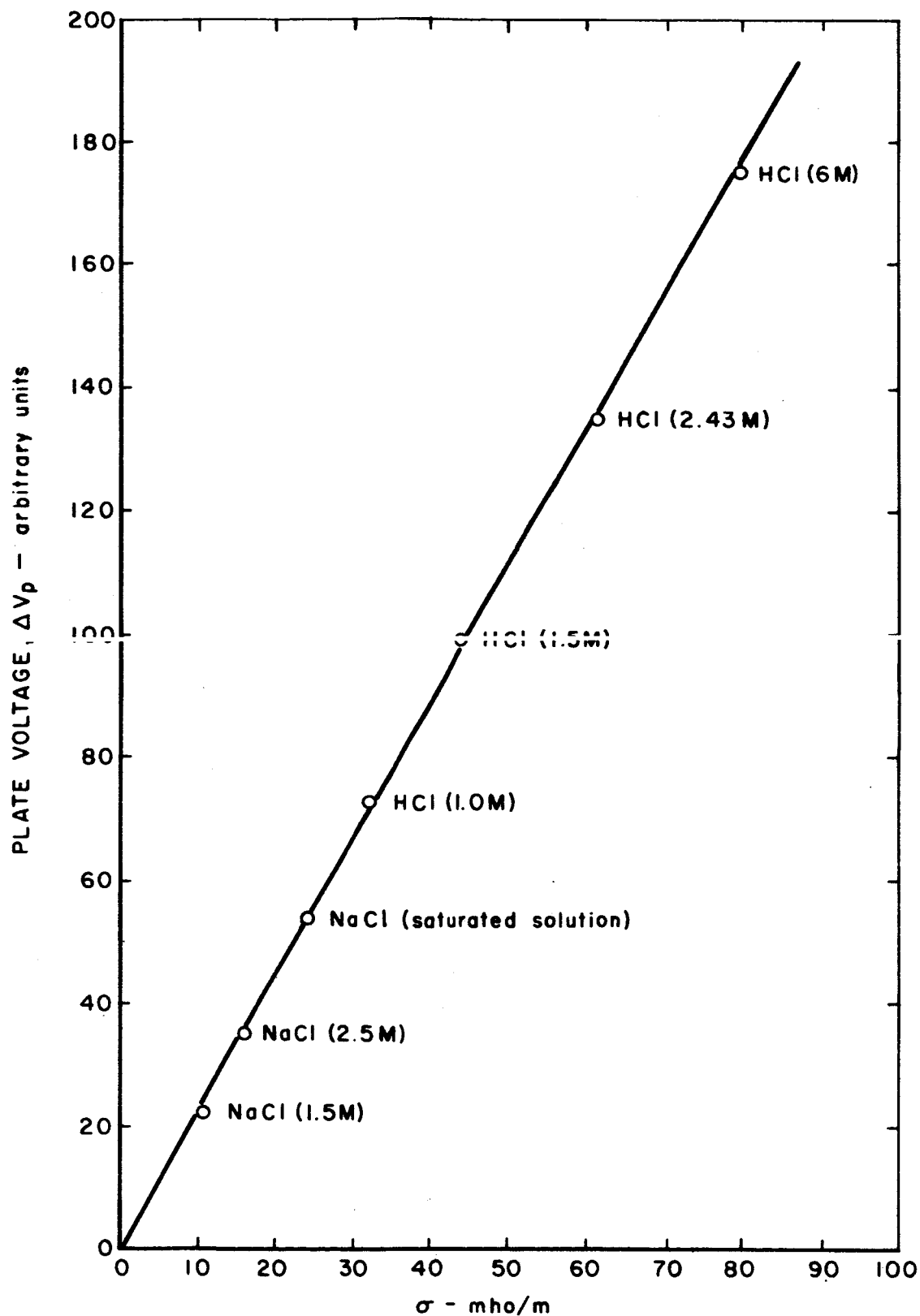




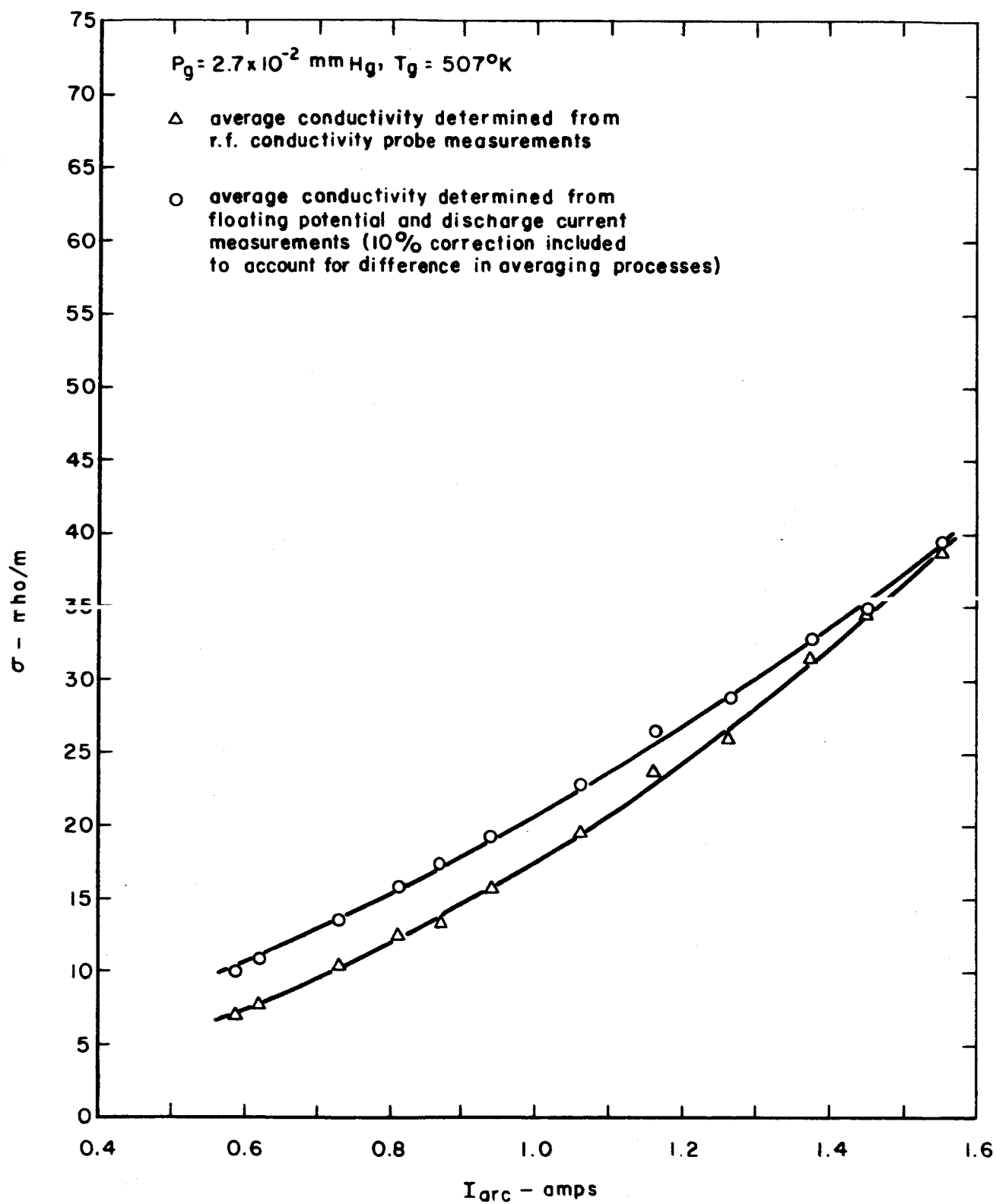
## ANODE REGION OF CESIUM DISCHARGE TUBE WITH CONDUCTIVITY PROBE



# CALIBRATION OF R.F. CONDUCTIVITY PROBE USING STANDARD ELECTROLYTIC SOLUTIONS

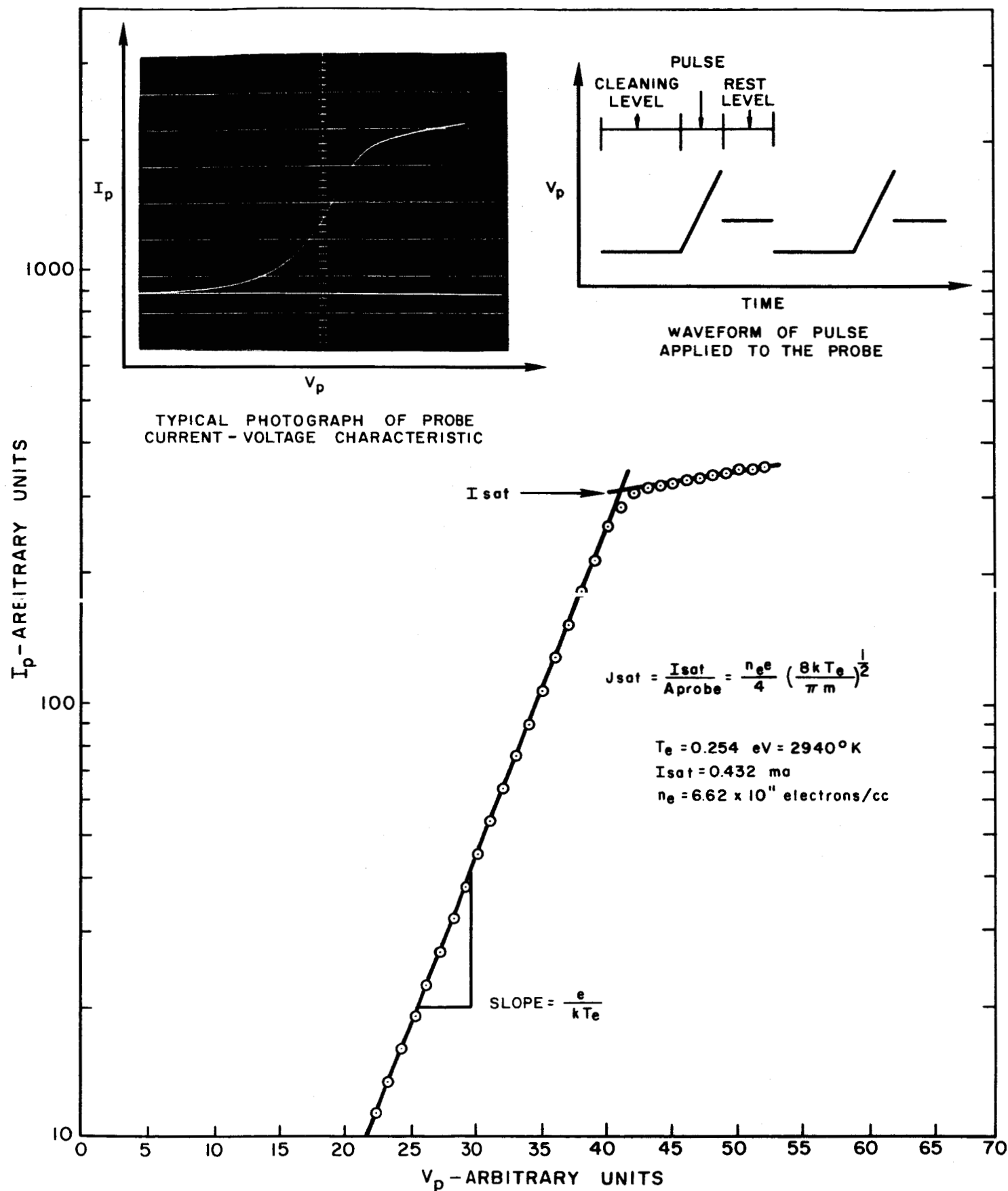


# VARIATION OF AVERAGED PLASMA CONDUCTIVITY WITH DISCHARGE CURRENT

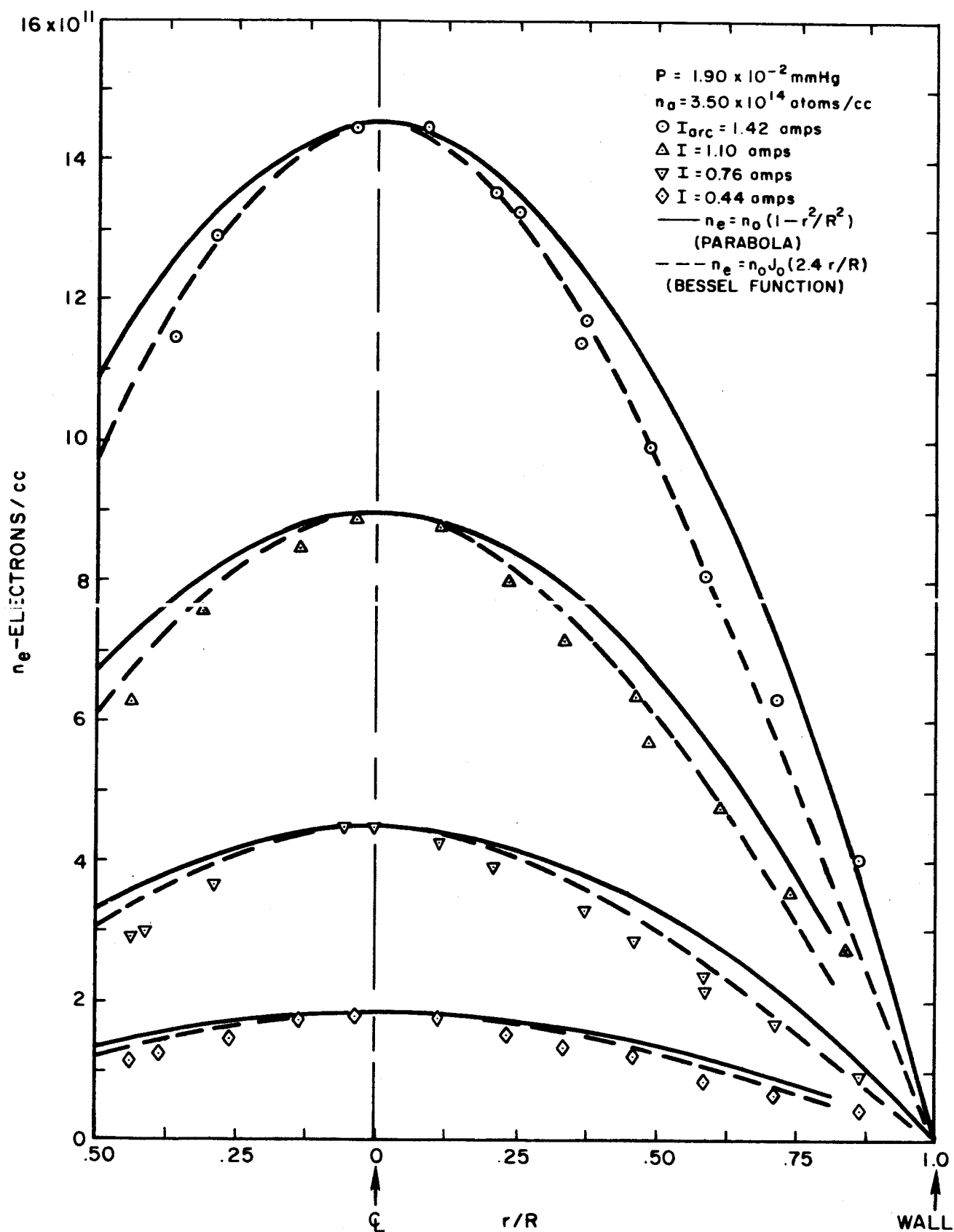




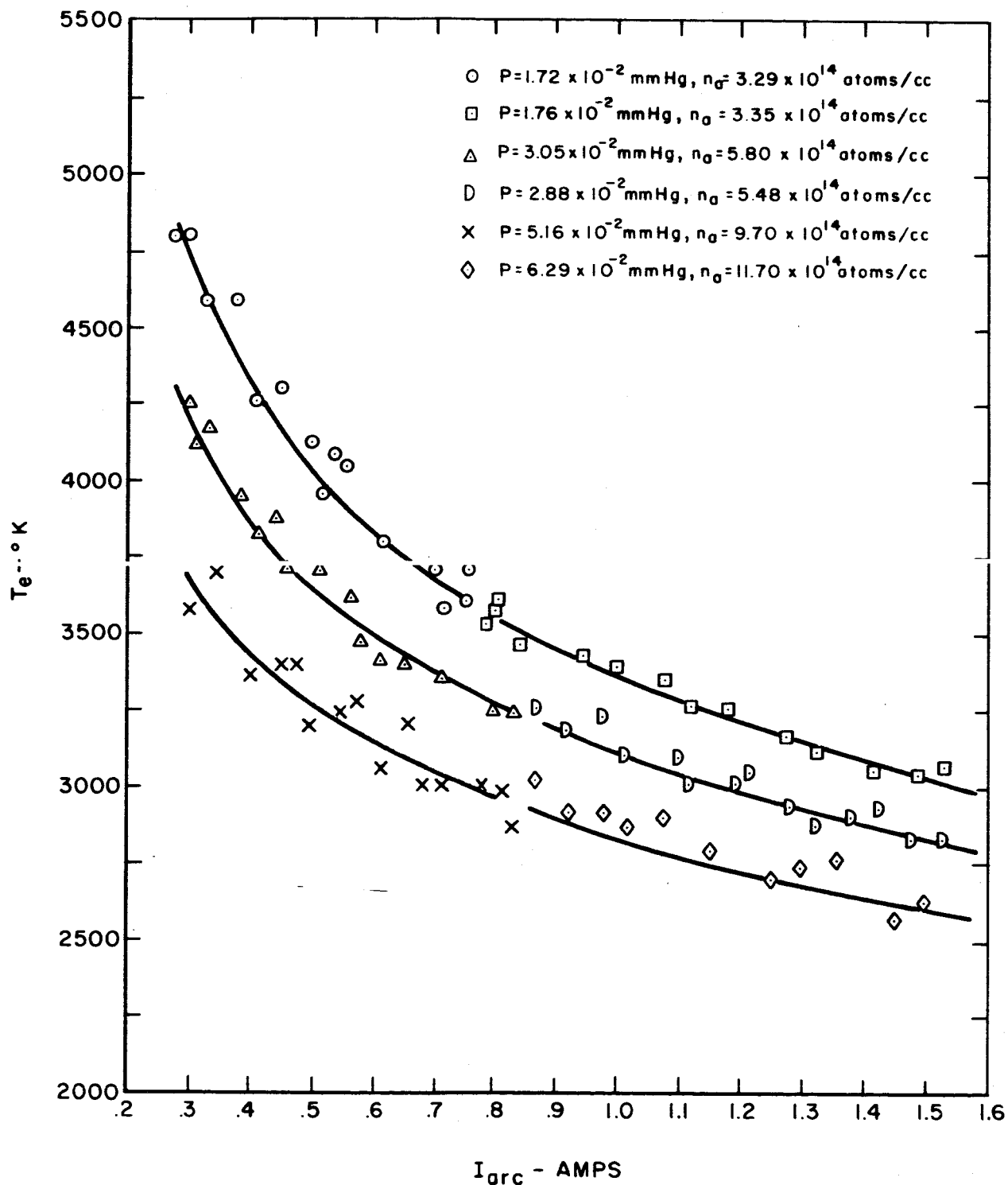
# TYPICAL SEMI-LOG PLOT OF ELECTROSTATIC PROBE CURRENT VOLTAGE - CHARACTERISTIC



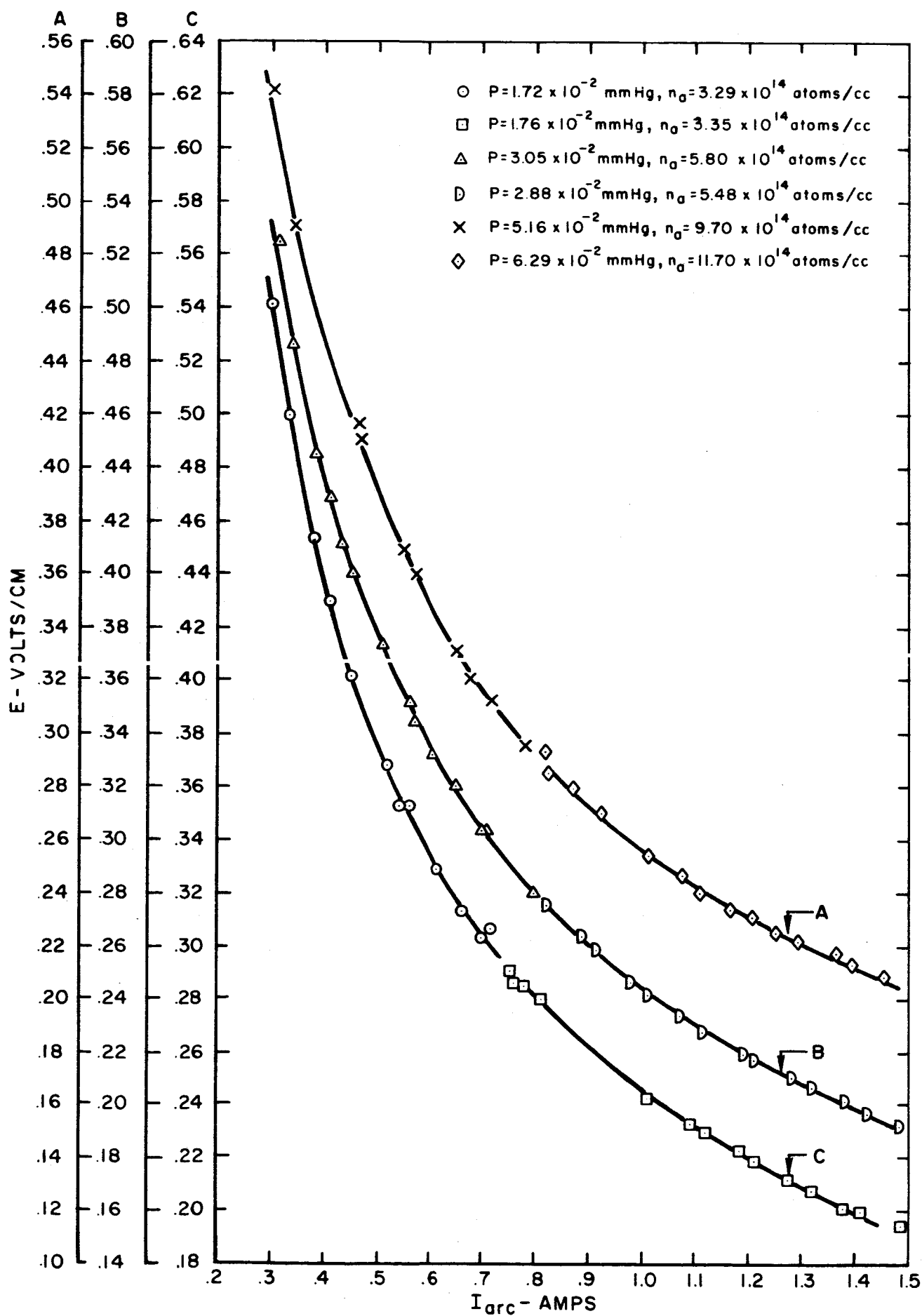
# VARIATION OF ELECTRON DENSITY WITH RADIAL POSITION



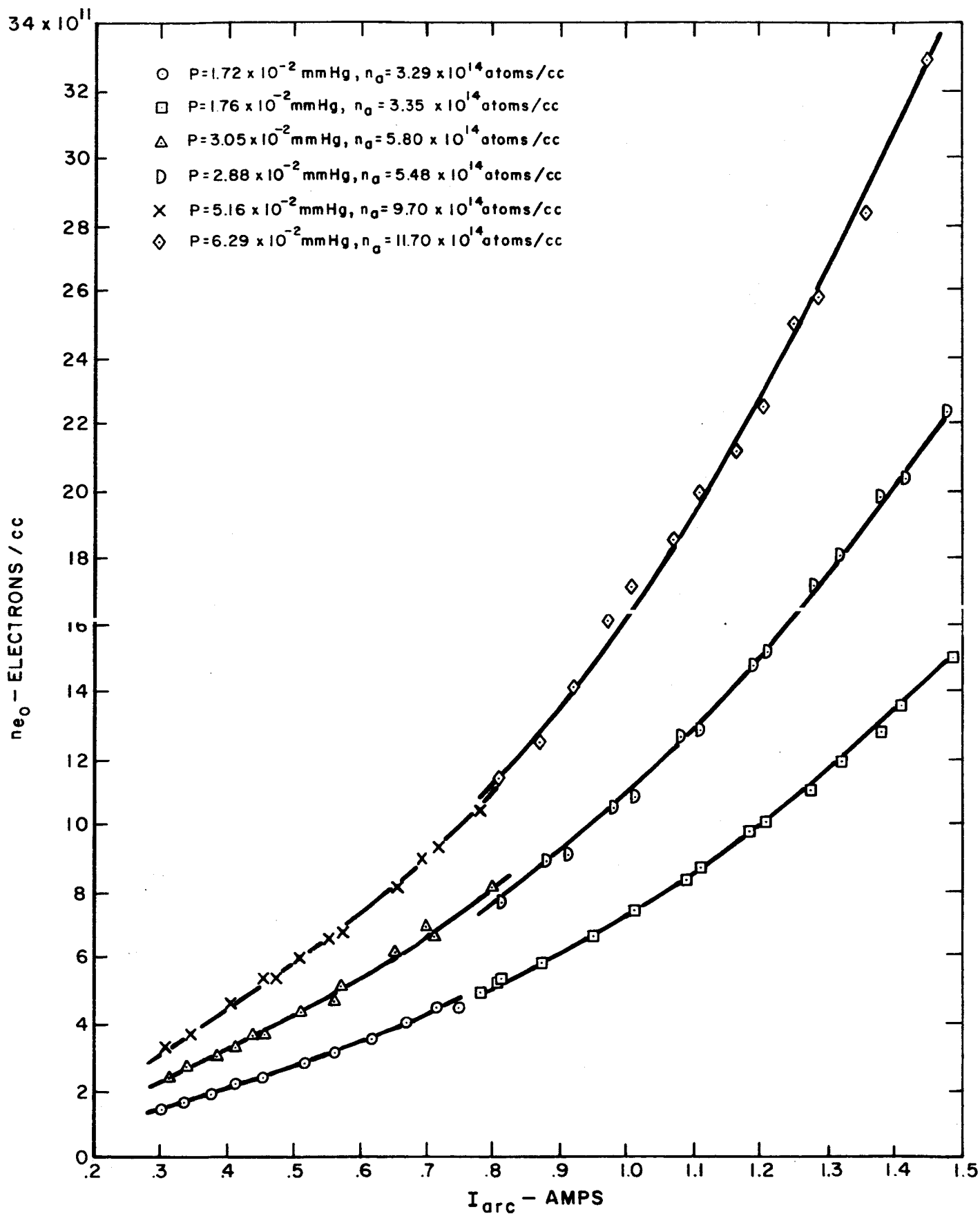
# VARIATION OF ELECTRON TEMPERATURE WITH DISCHARGE CURRENT AND PRESSURE



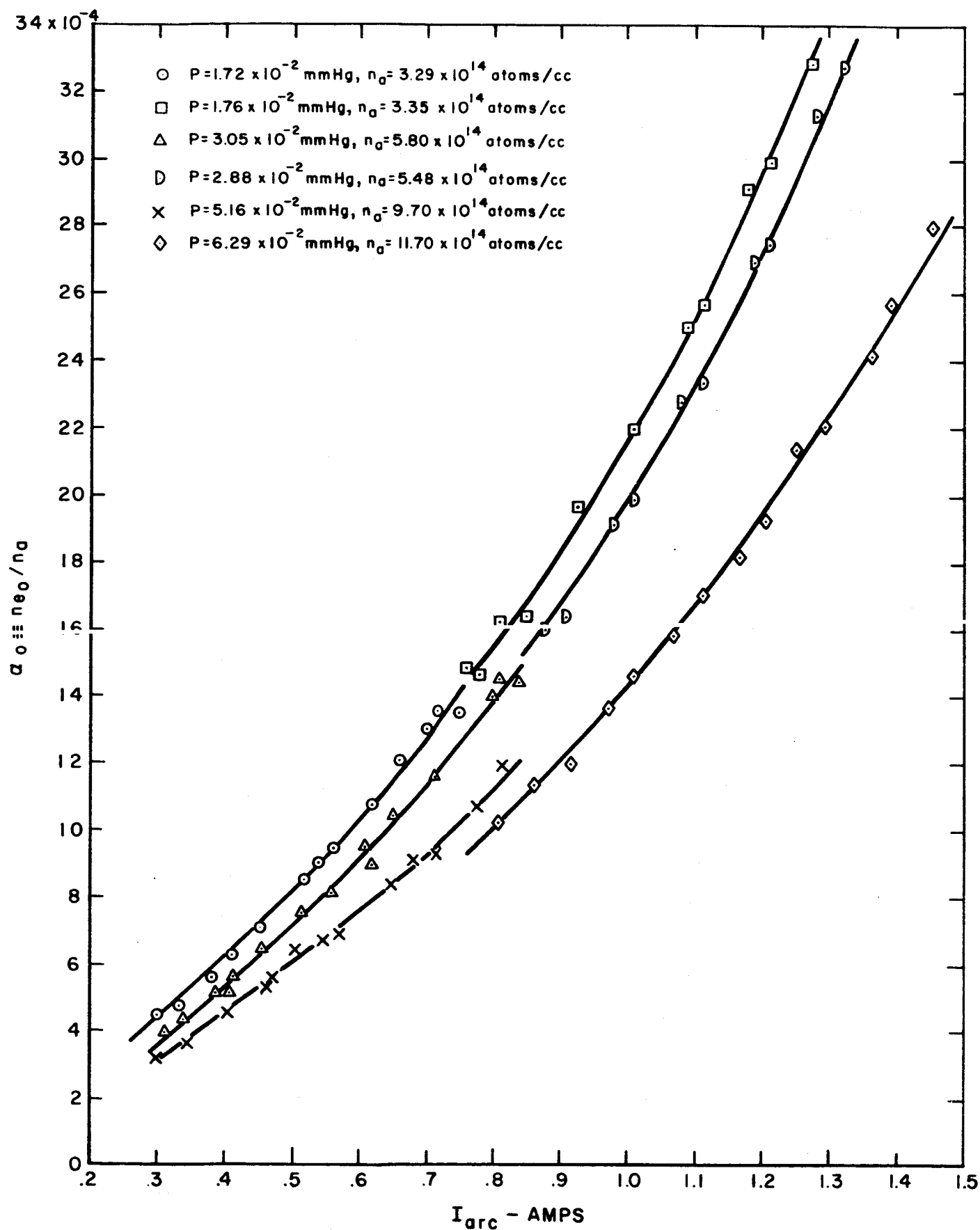
# VARIATION OF ELECTRIC FIELD WITH DISCHARGE CURRENT AND PRESSURE



# VARIATION OF ELECTRON DENSITY WITH DISCHARGE CURRENT AND PRESSURE



# VARIATION OF DEGREE OF IONIZATION WITH DISCHARGE CURRENT AND PRESSURE



# EXPERIMENTALLY DETERMINED NORMALIZED EFFECTIVE ELECTRON-CESIUM HEAVY PARTICLE COLLISION FREQUENCY VARIATION WITH ELECTRON TEMPERATURE AND DEGREE OF IONIZATION

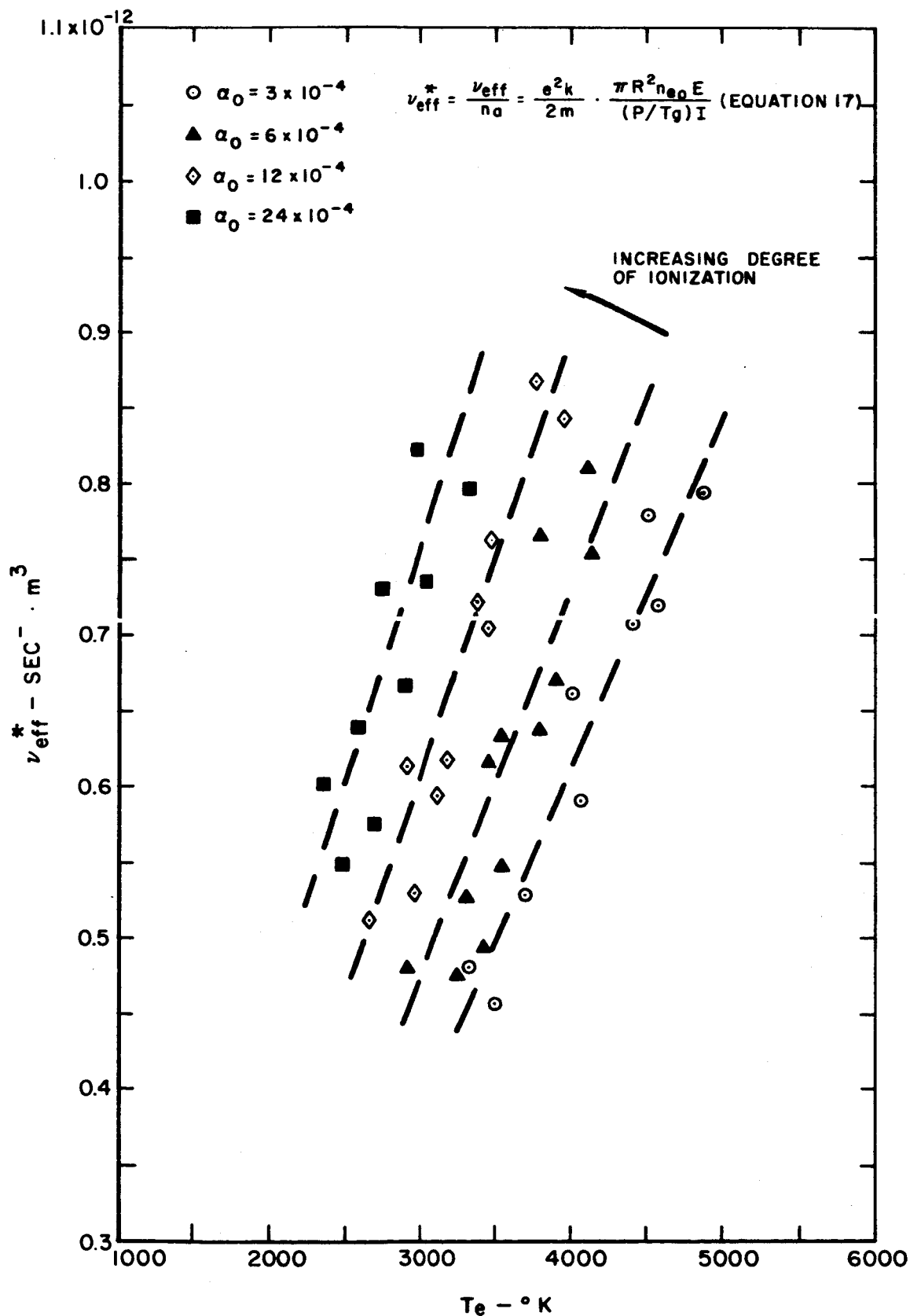
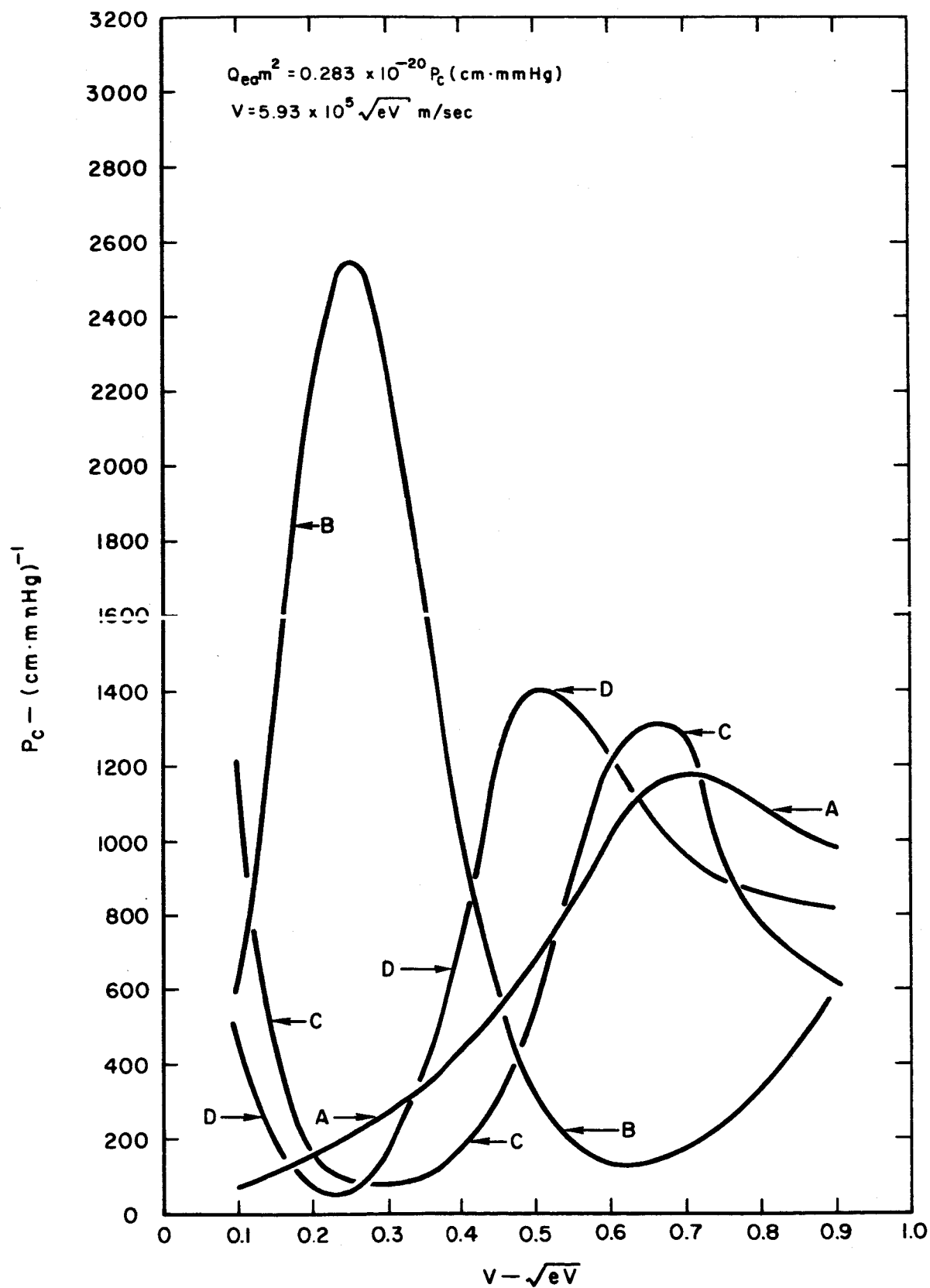
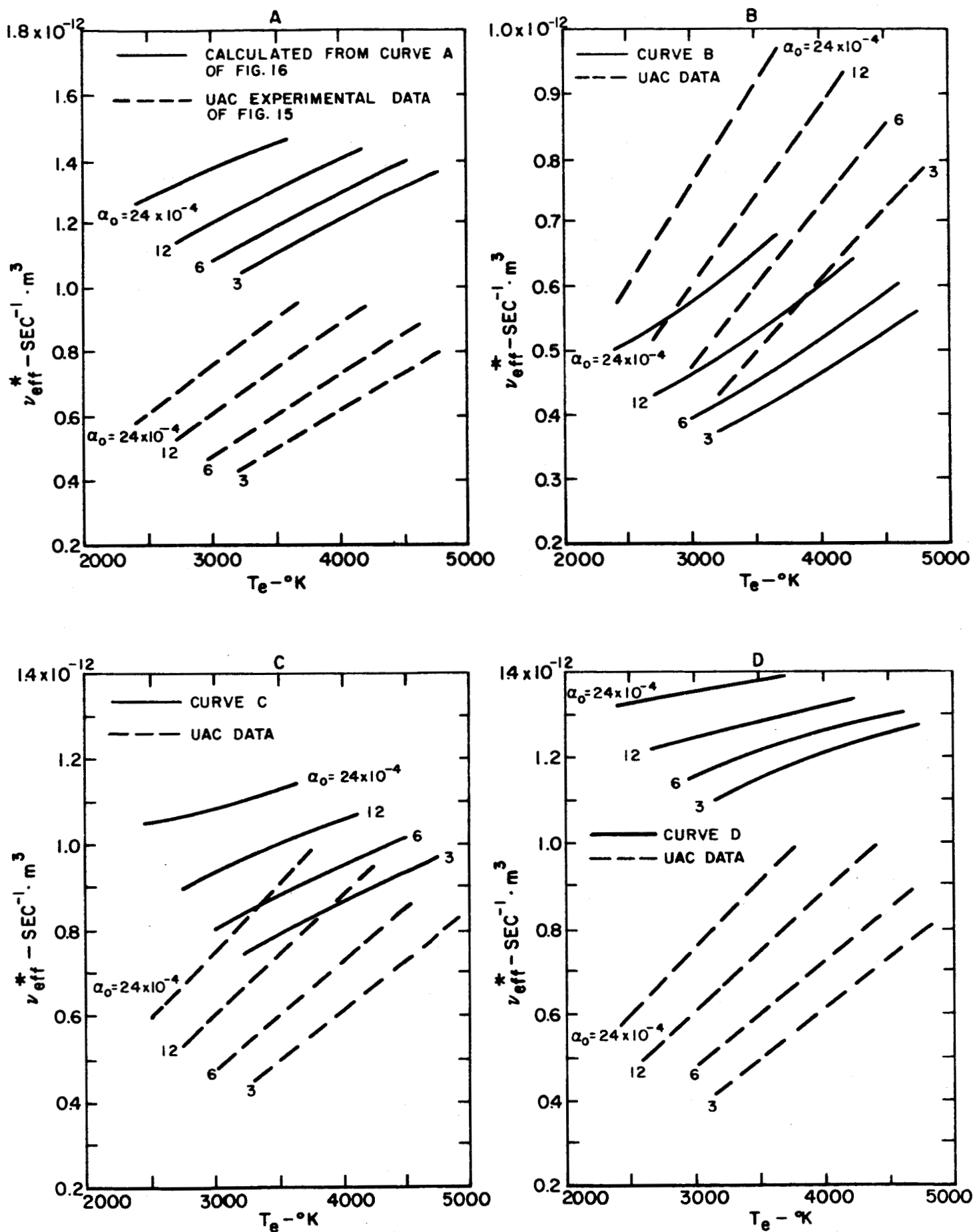


ILLUSTRATION OF TYPICAL TRIAL FUNCTIONS FOR THE  
ELECTRON-CESIUM ATOM MOMENTUM TRANSFER COLLISION  
PROBABILITY

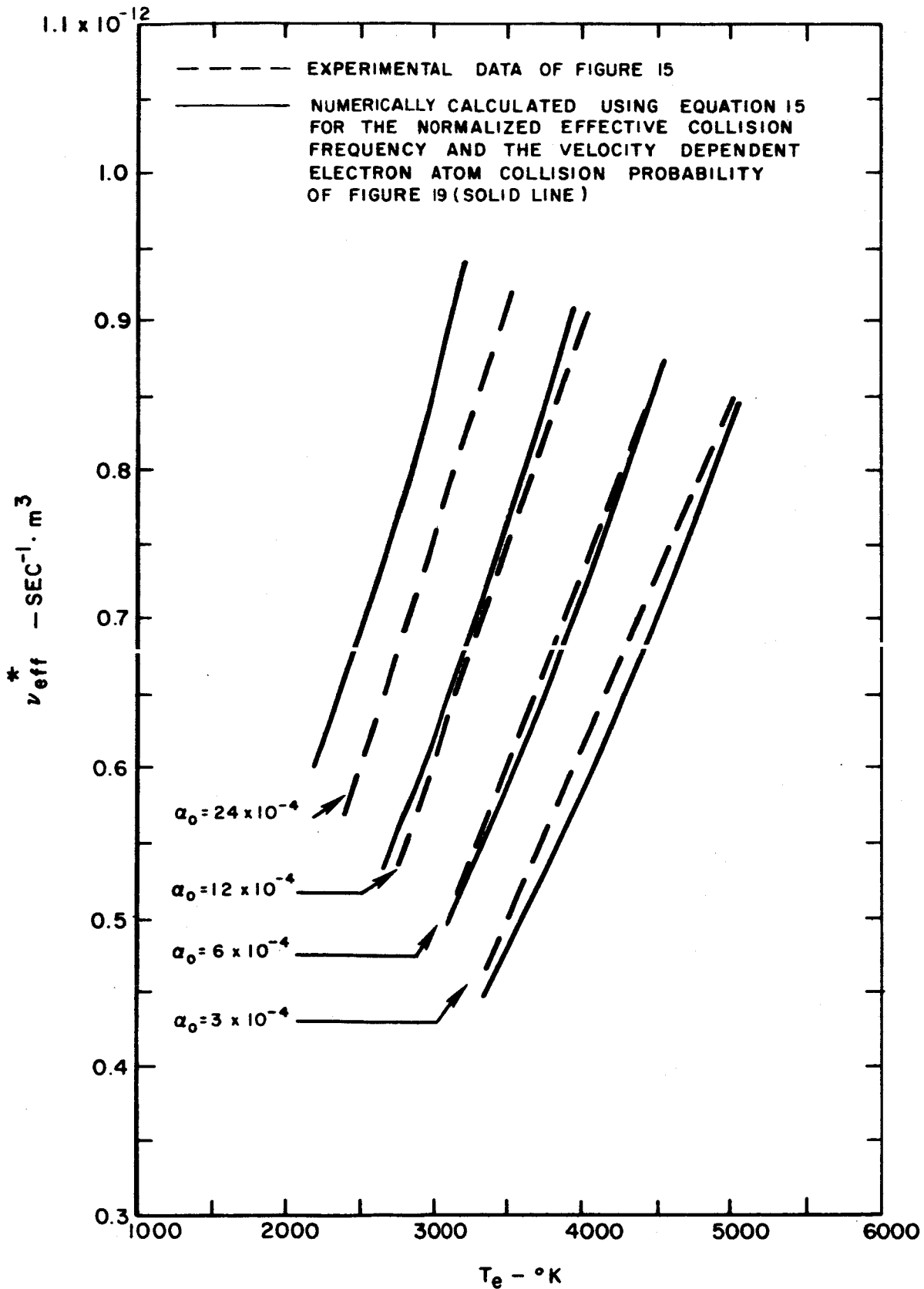




# NORMALIZED EFFECTIVE COLLISION FREQUENCY CALCULATED USING EQUATION 15 AND THE TRIAL FUNCTIONS FOR THE COLLISION PROBABILITY SHOWN IN FIGURE 16



# COMPARISON OF EXPERIMENTALLY DETERMINED AND NUMERICALLY CALCULATED NORMALIZED EFFECTIVE COLLISION FREQUENCY



# ELECTRON-CESIUM ATOM MOMENTUM TRANSFER COLLISION PROBABILITY DETERMINED FROM AN ANALYSIS OF THE EXPERIMENTAL AND NUMERICAL NORMALIZED EFFECTIVE COLLISION FREQUENCY DATA

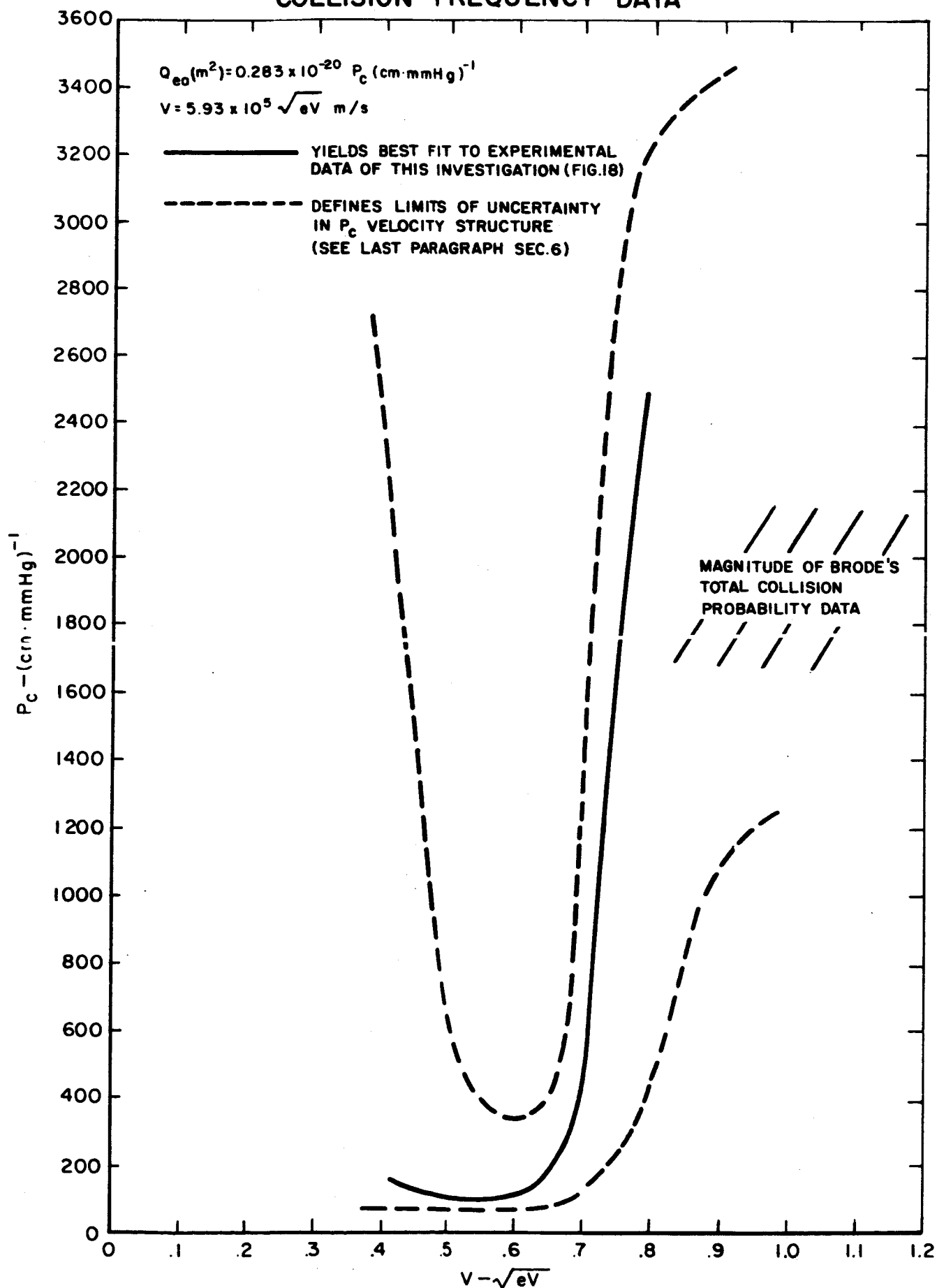


# ILLUSTRATION OF THE IMPROVEMENT IN RESOLUTION OF COLLISION PROBABILITY VELOCITY STRUCTURE THROUGH DEPENDENCE OF EFFECTIVE COLLISION FREQUENCY ON DEGREE OF IONIZATION

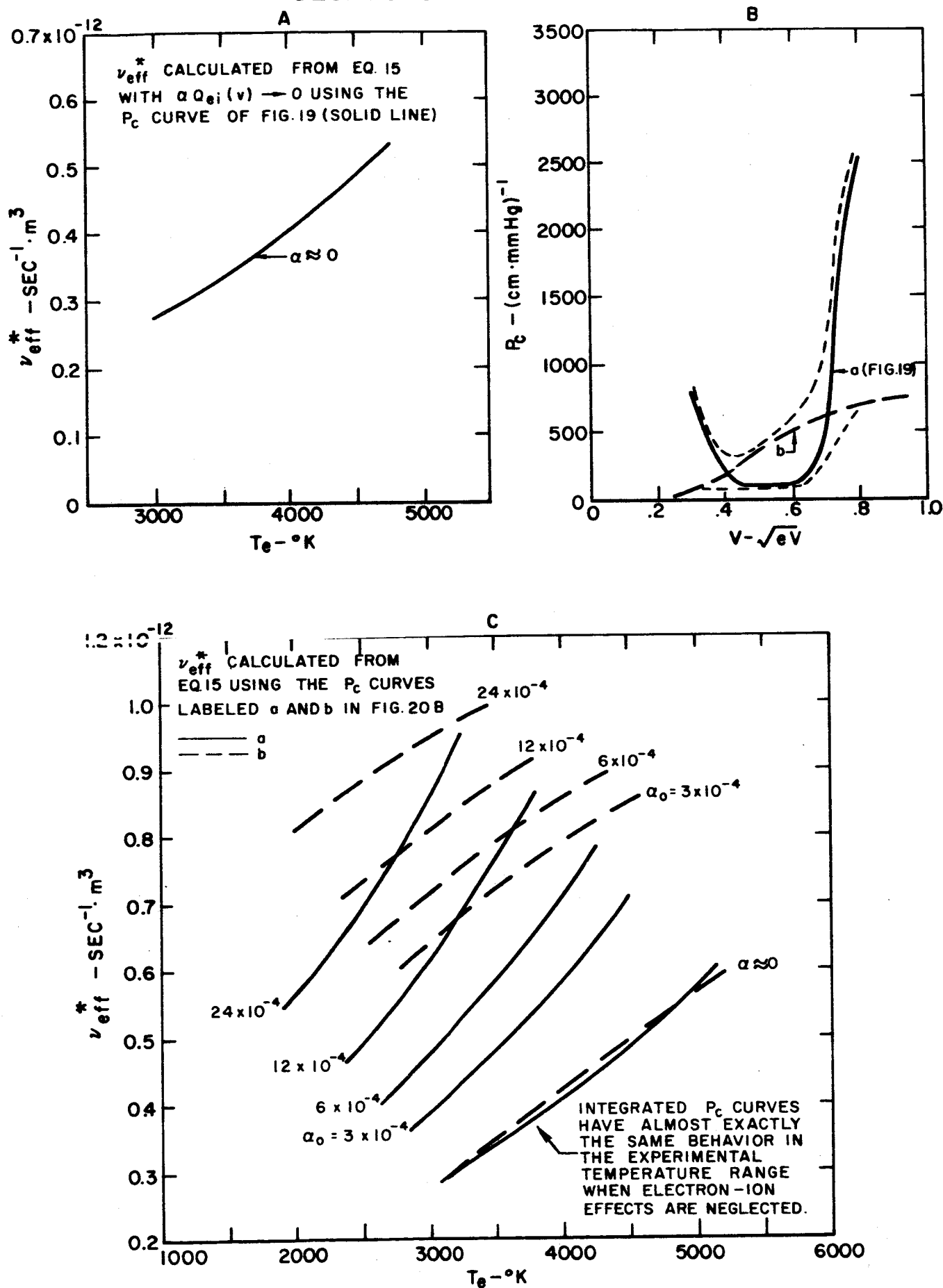
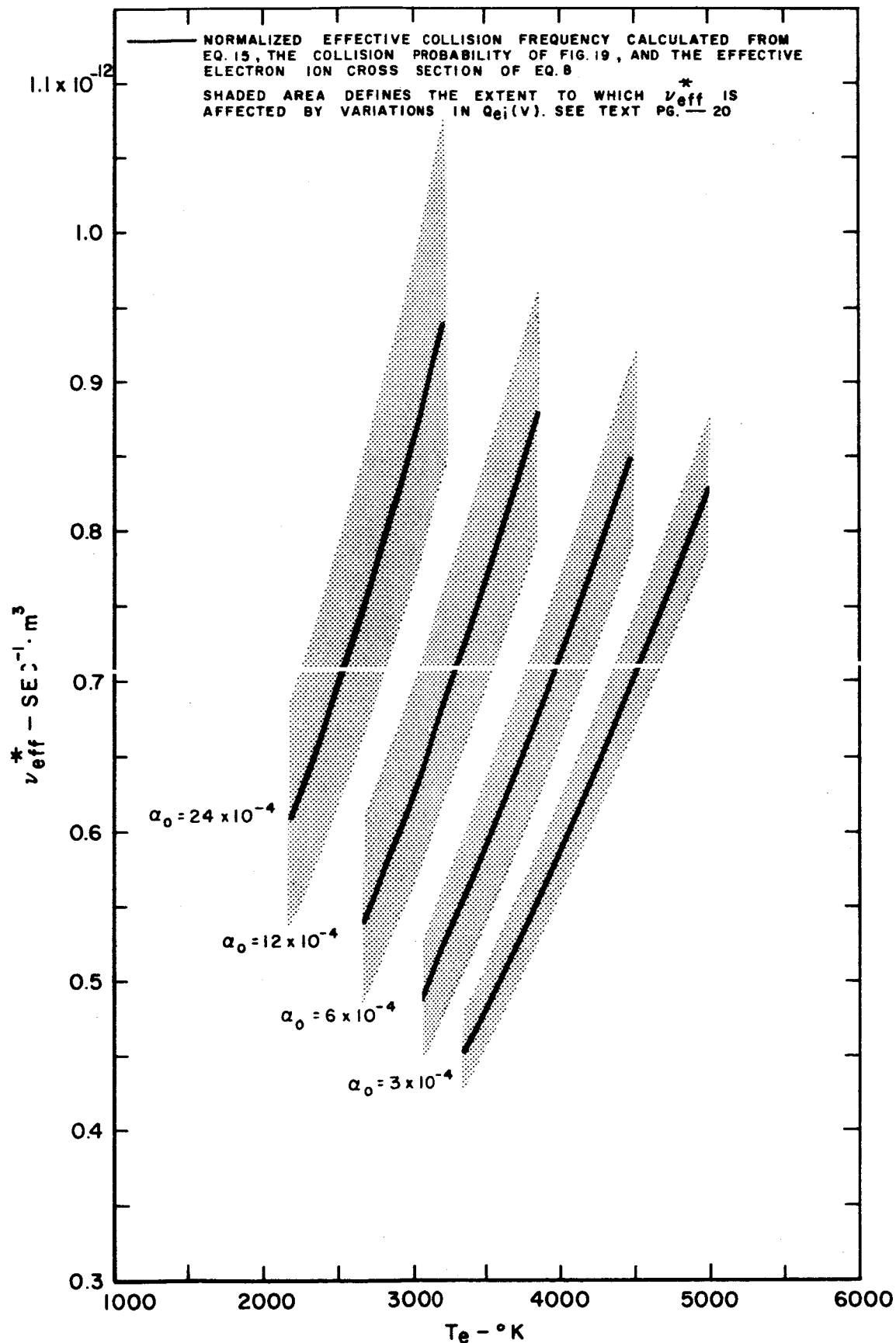
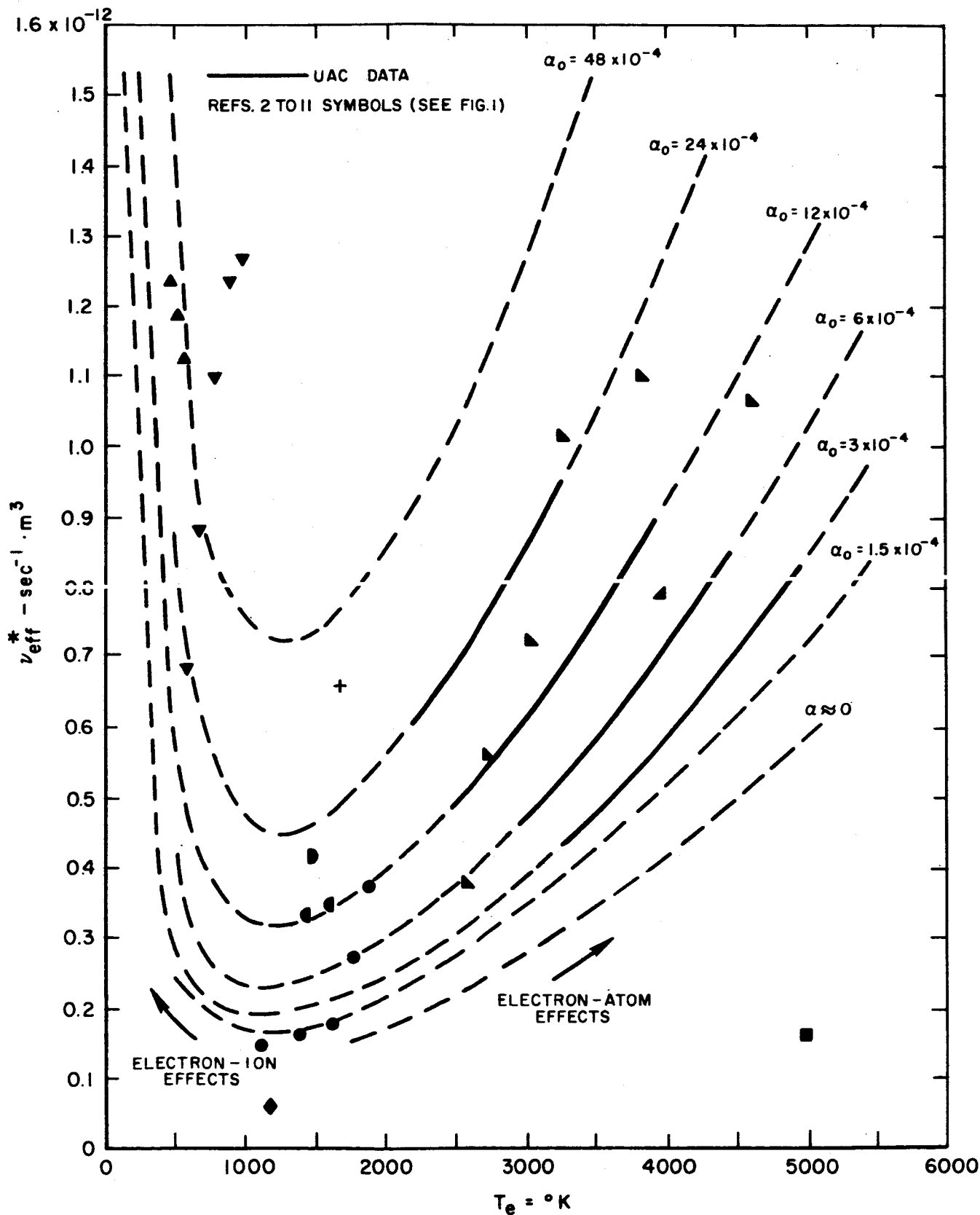


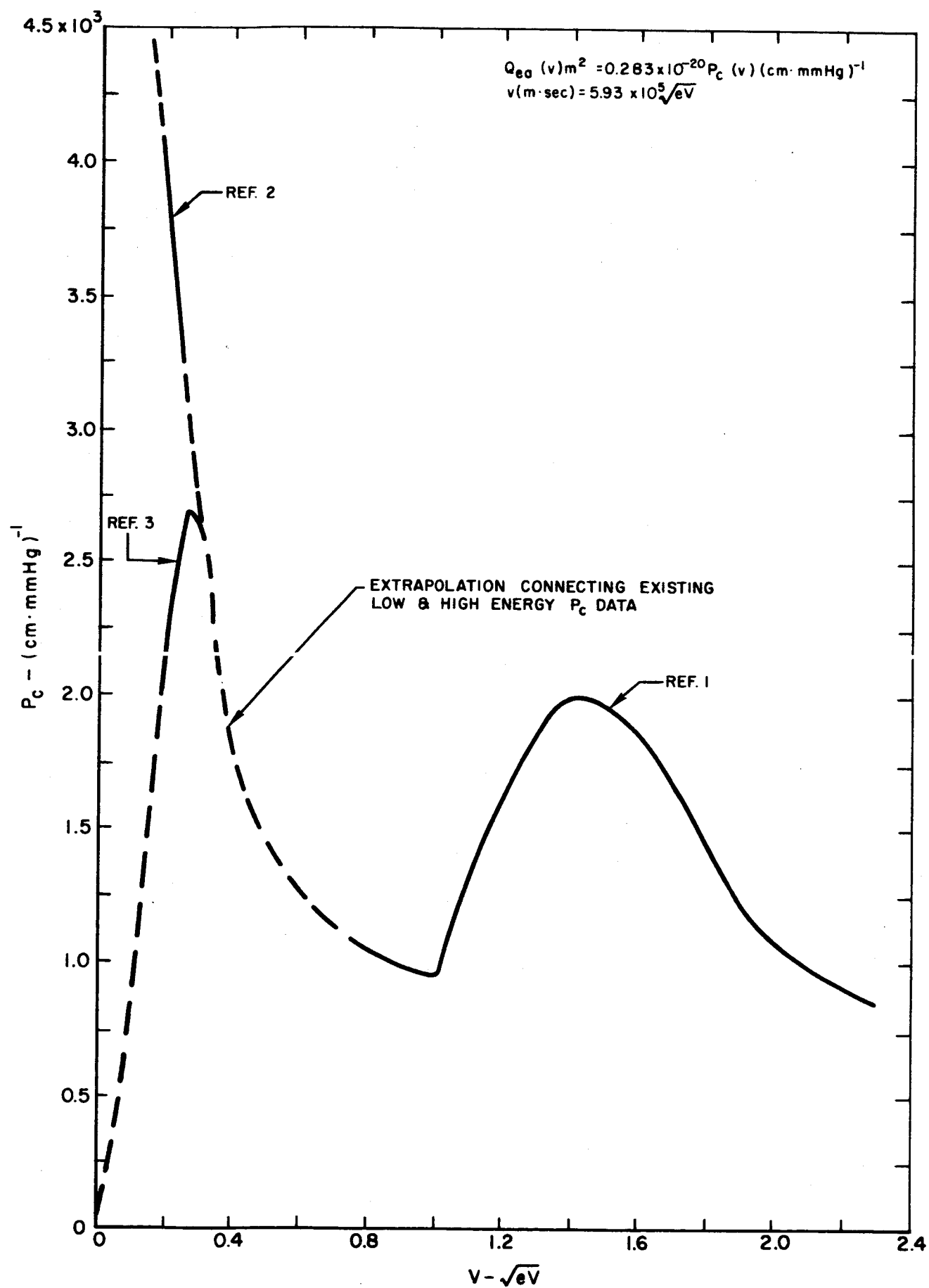
# ILLUSTRATION OF THE SENSITIVITY OF THE CALCULATED EFFECTIVE COLLISION FREQUENCY TO VARIATIONS IN THE VELOCITY DEPENDENCE AND MAGNITUDE OF THE EFFECTIVE ELECTRON-ION CROSS SECTION



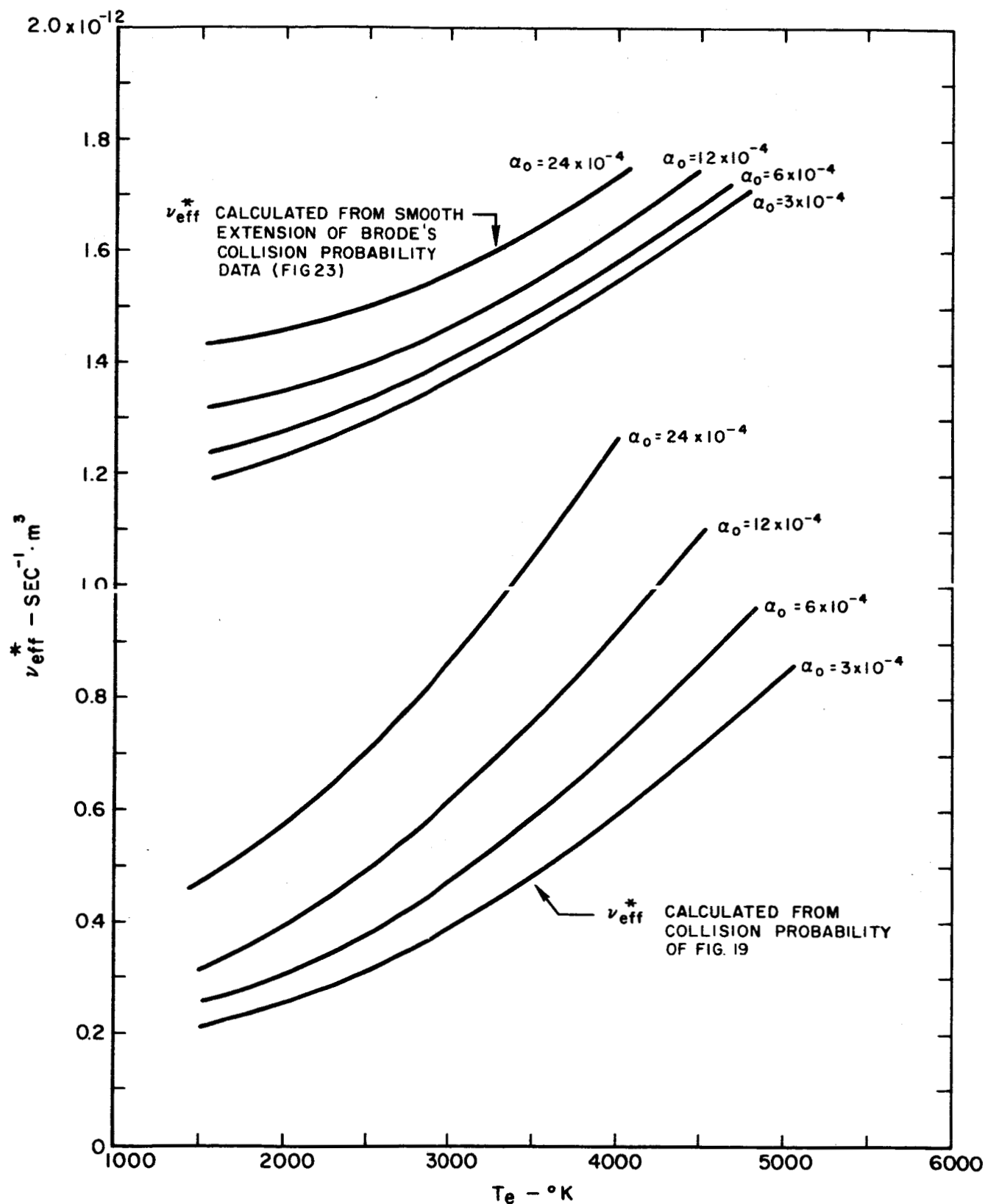
**NORMALIZED EFFECTIVE COLLISION FREQUENCY FROM  
REFERENCES 2 TO 11 COMPARED WITH UAC  
EXPERIMENTAL DATA AND EFFECTIVE COLLISION  
FREQUENCY CALCULATED USING EQUATION 15 AND THE  
COLLISION PROBABILITY OF FIGURE 19**



# ELECTRON-CESIUM ATOM COLLISION PROBABILITY VARIATION WITH ELECTRON VELOCITY

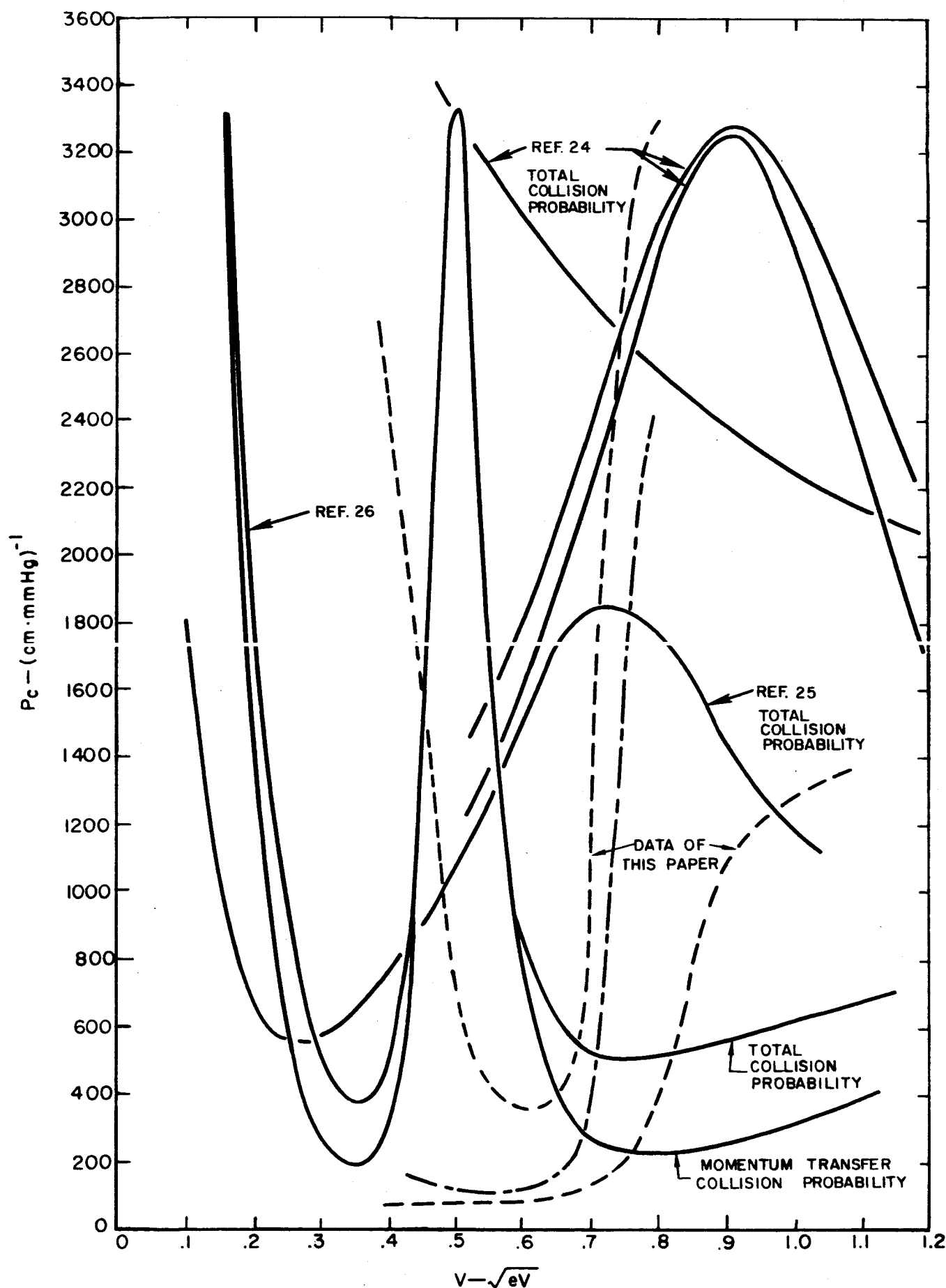


NORMALIZED EFFECTIVE COLLISION FREQUENCY CALCULATED  
USING THE EXTRAPOLATED COLLISION PROBABILITY OF FIGURE 23  
COMPARED WITH THE COLLISION FREQUENCY DATA OF FIG 22

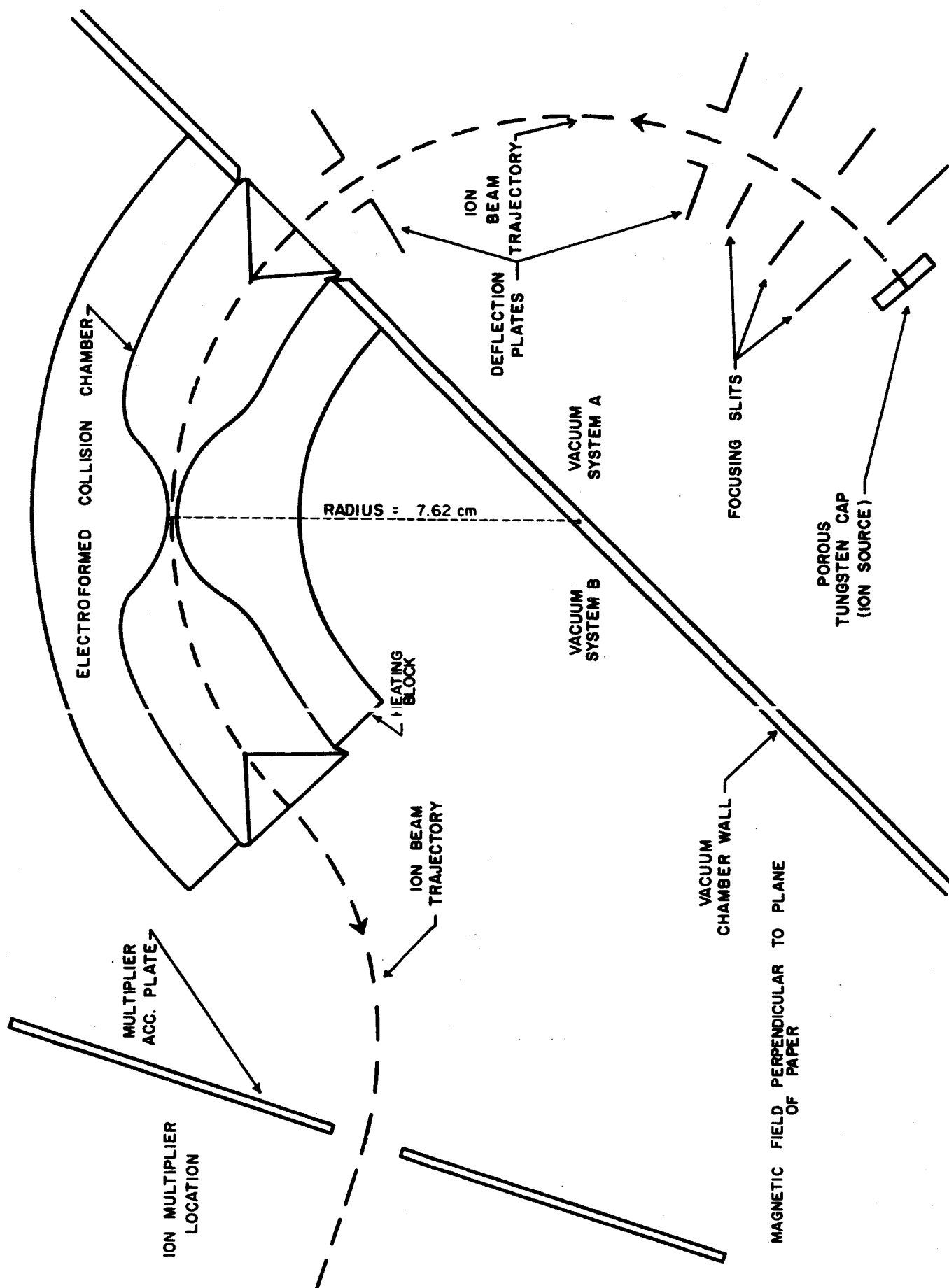




THEORETICALLY CALCULATED ELECTRON-CESIUM ATOM  
COLLISION PROBABILITY COMPARED WITH COLLISION  
PROBABILITY DATA OF THIS INVESTIGATION

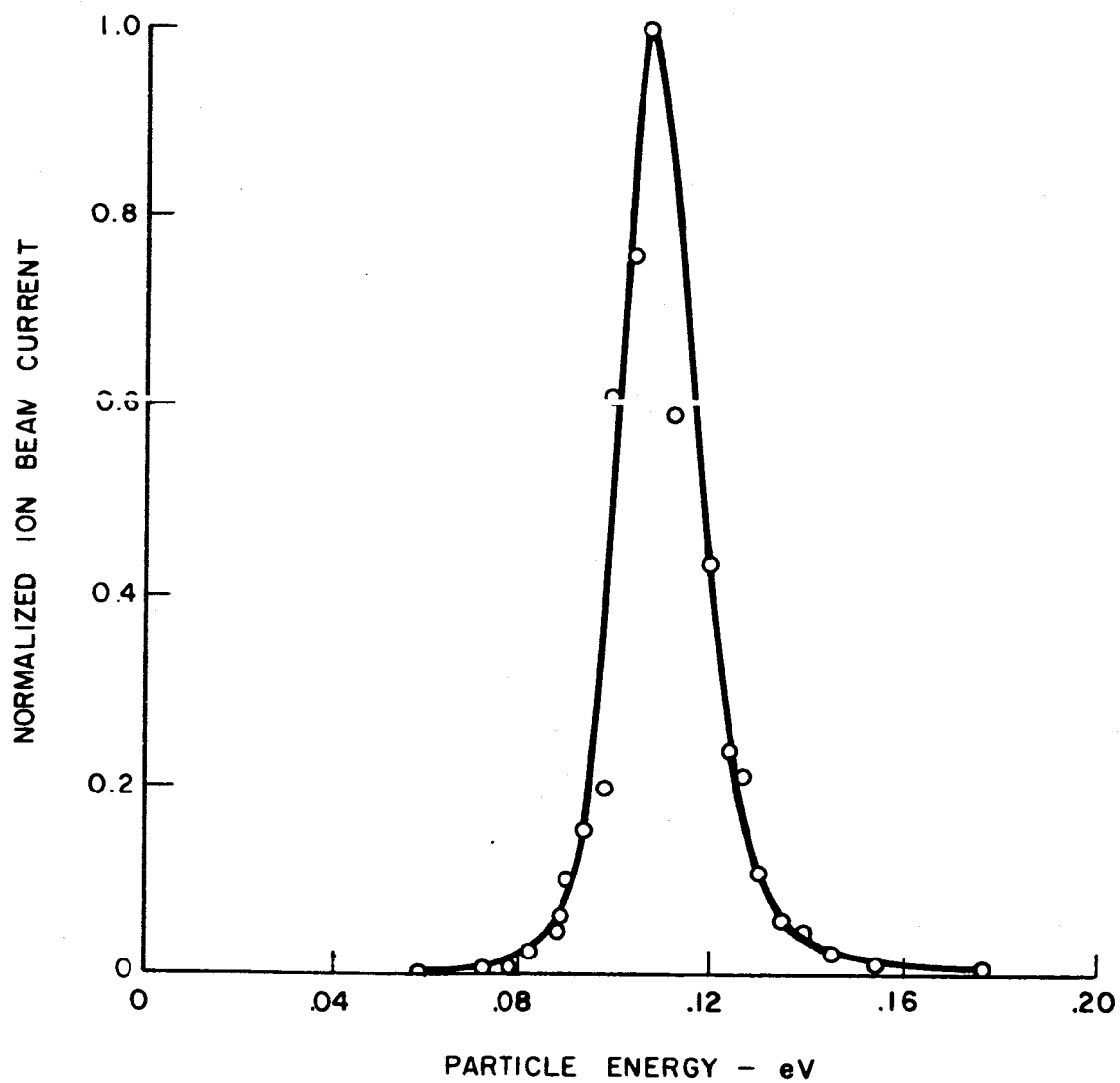


## SCHEMATIC DIAGRAM OF ION COLLISION CROSS-SECTION APPARATUS



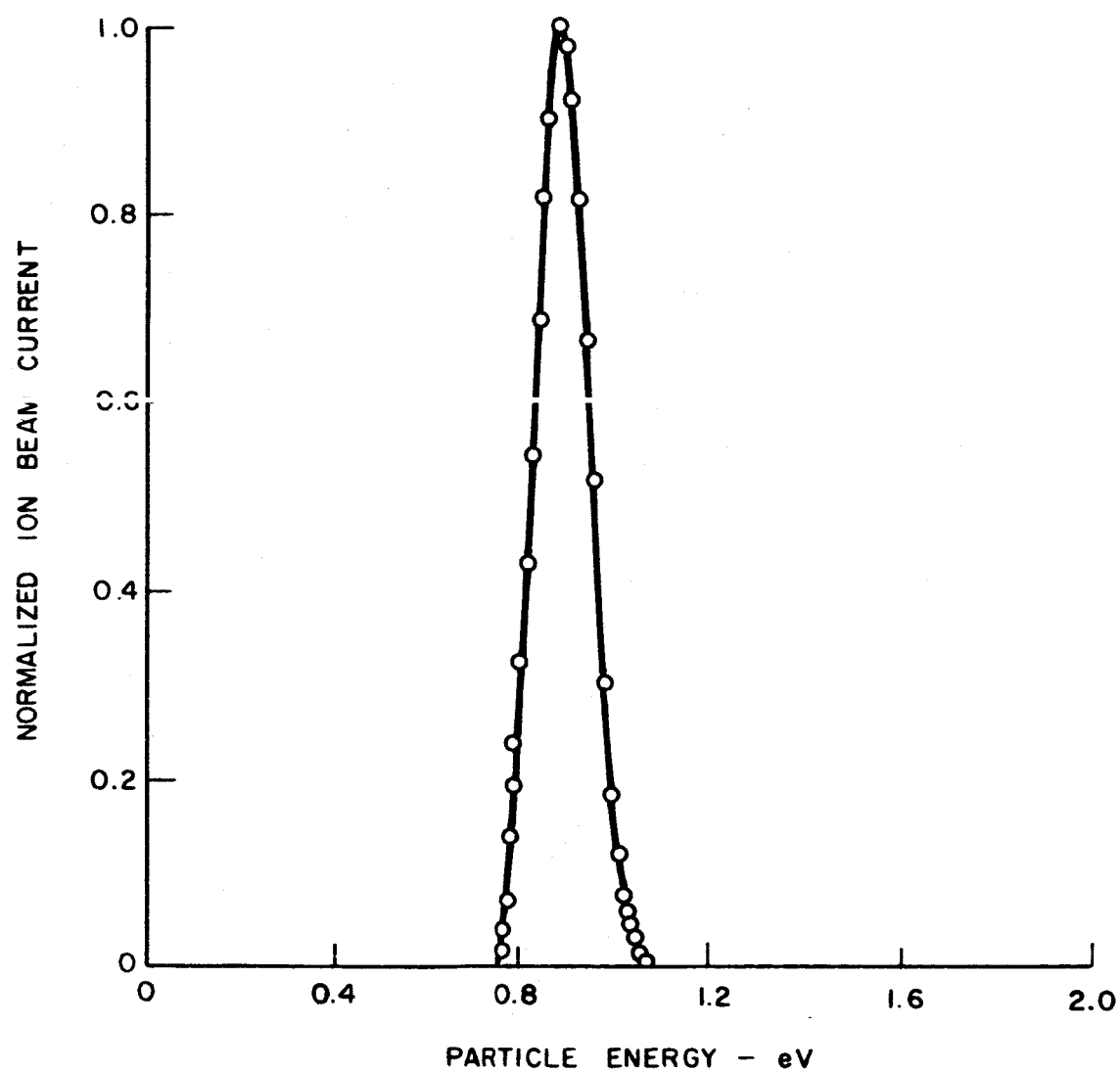
## NORMALIZED ION BEAM ENERGY DISTRIBUTION

PEAK ENERGY = .107 eV



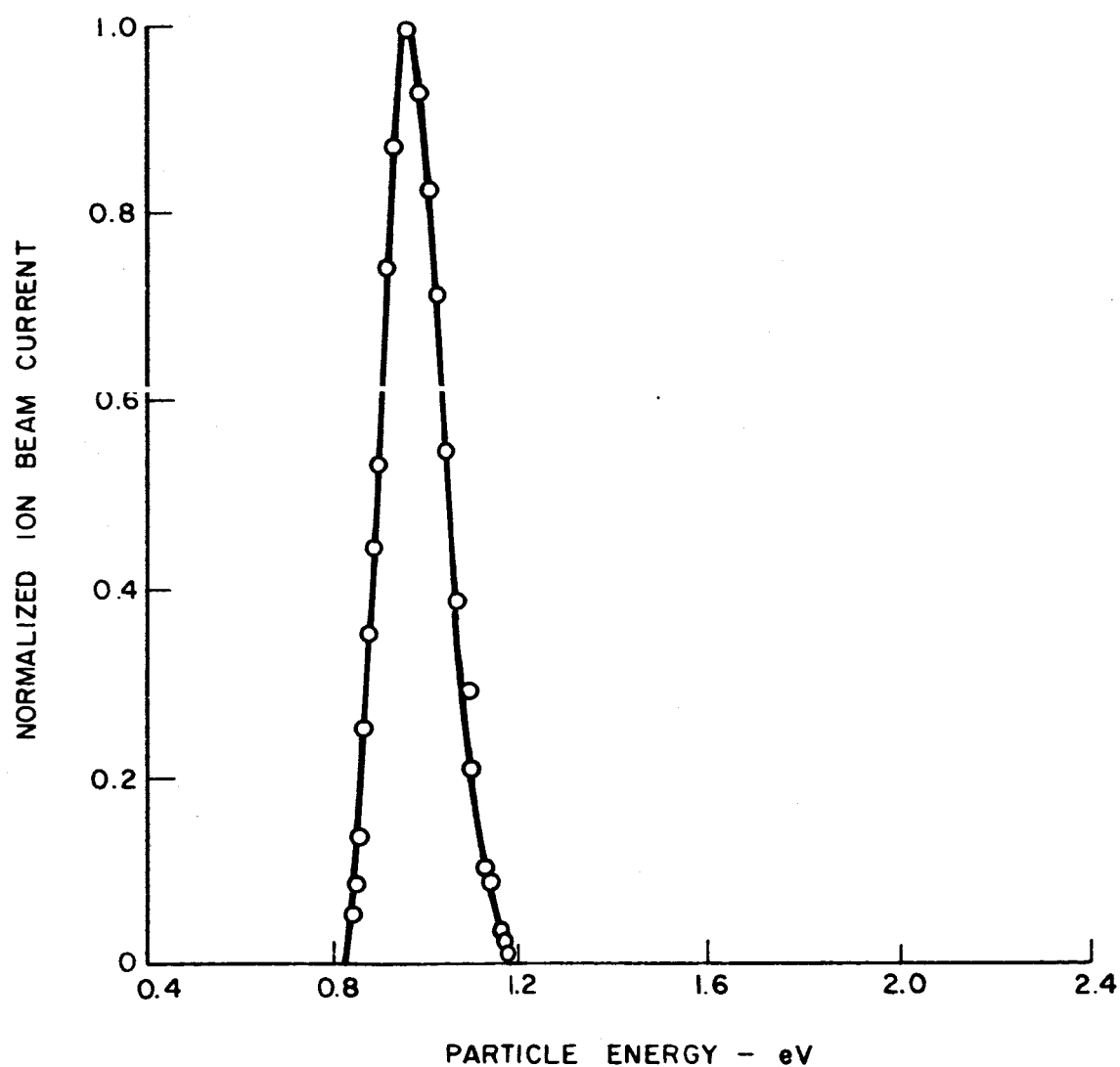
## NORMALIZED ION BEAM ENERGY DISTRIBUTION

PEAK ENERGY = 0.88 eV



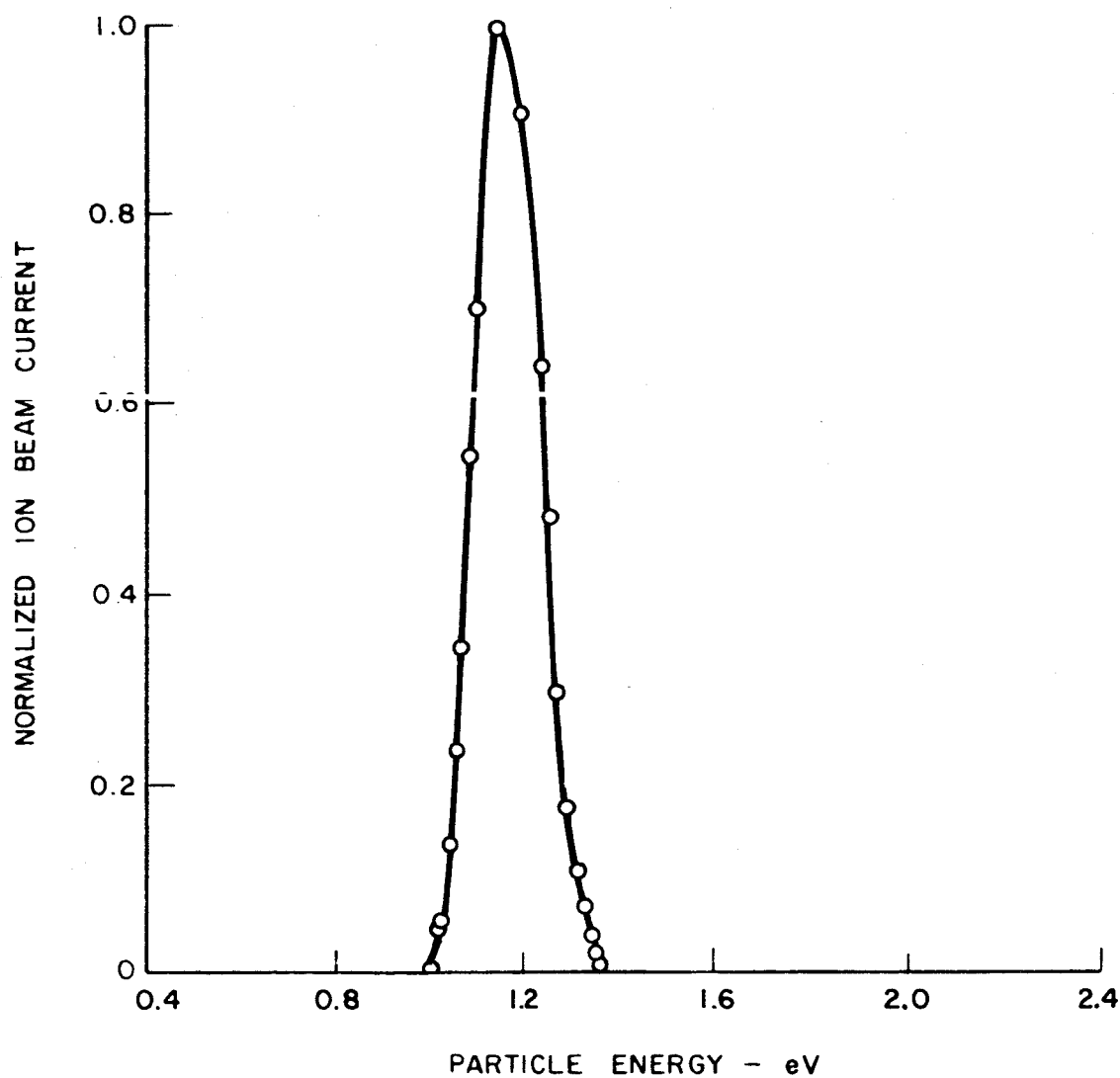
## NORMALIZED ION BEAM ENERGY DISTRIBUTION

PEAK ENERGY = 0.97 eV



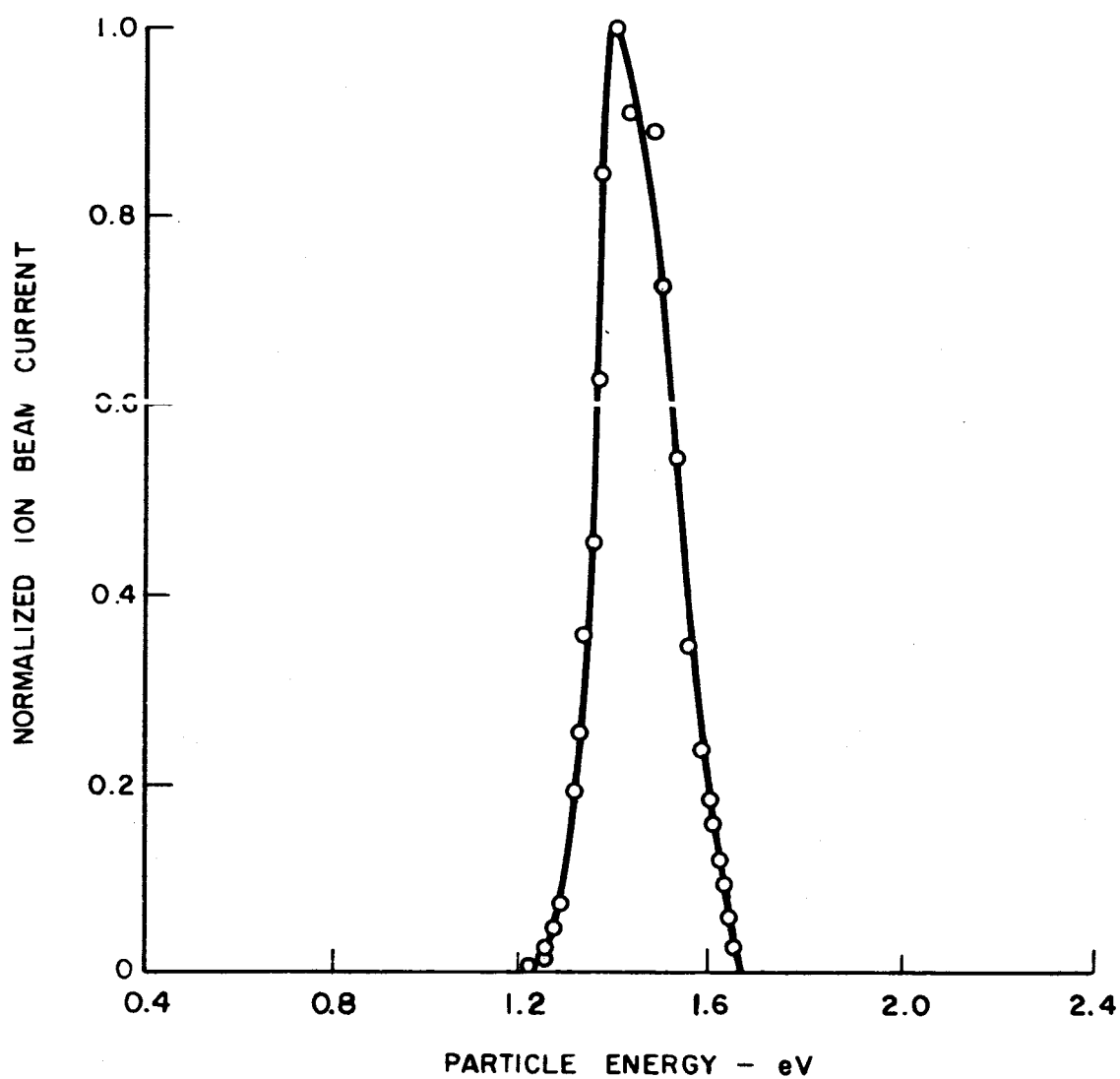
## NORMALIZED ION BEAM ENERGY DISTRIBUTION

PEAK ENERGY = 1.14 eV



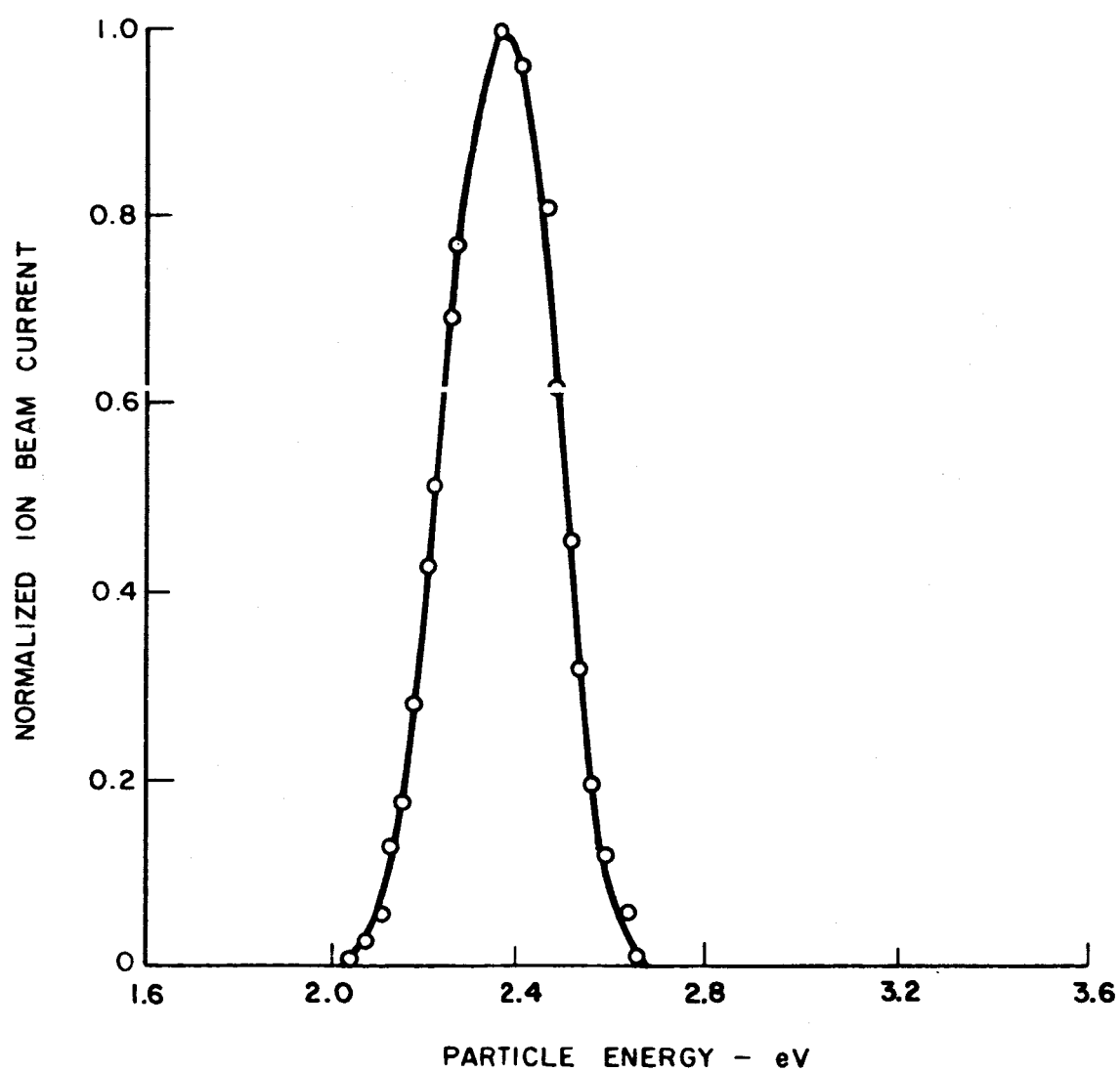
## NORMALIZED ION BEAM ENERGY DISTRIBUTION

PEAK ENERGY = 1.40 eV



## NORMALIZED ION BEAM ENERGY DISTRIBUTION

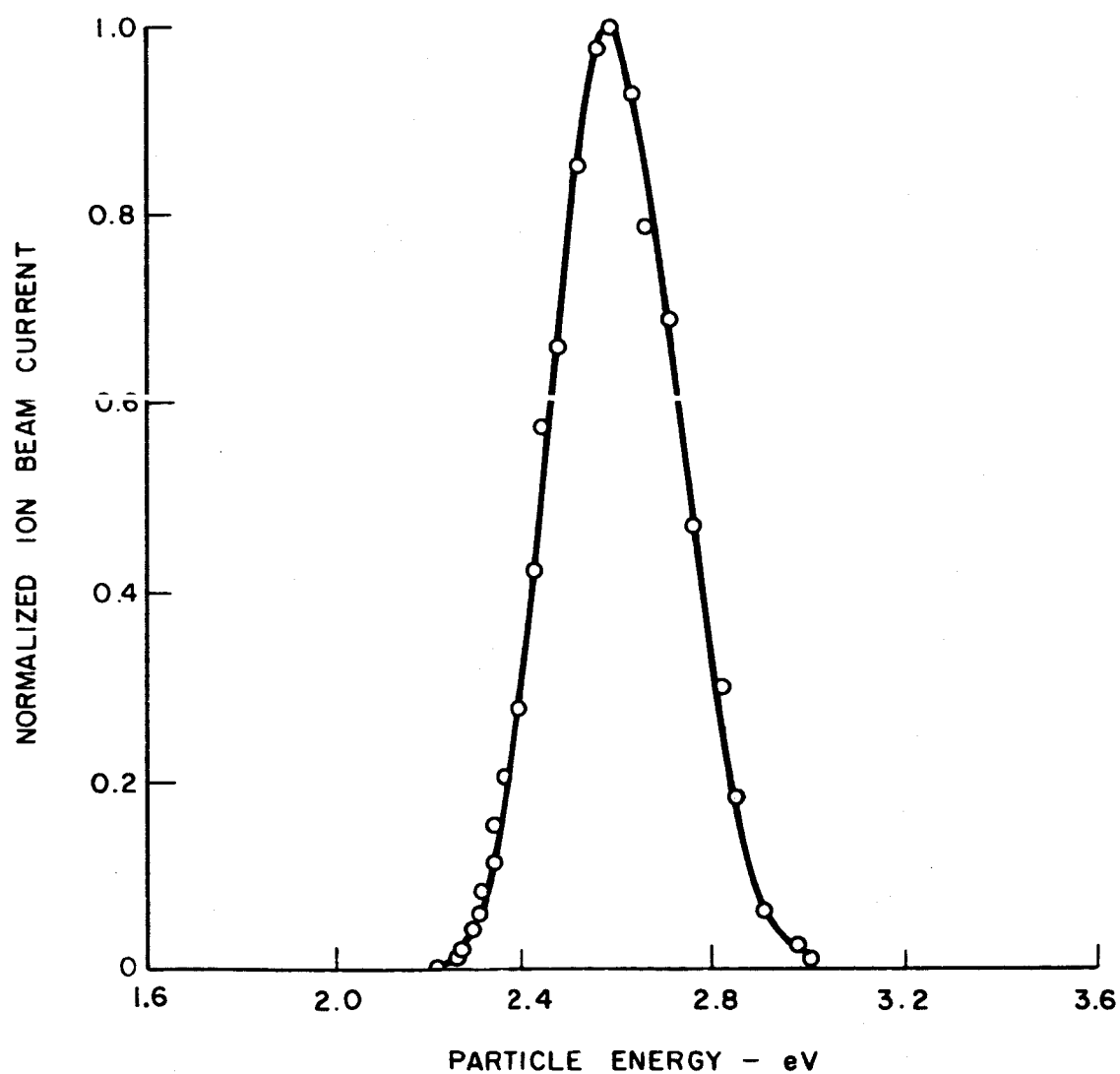
PEAK ENERGY = 2.36 eV



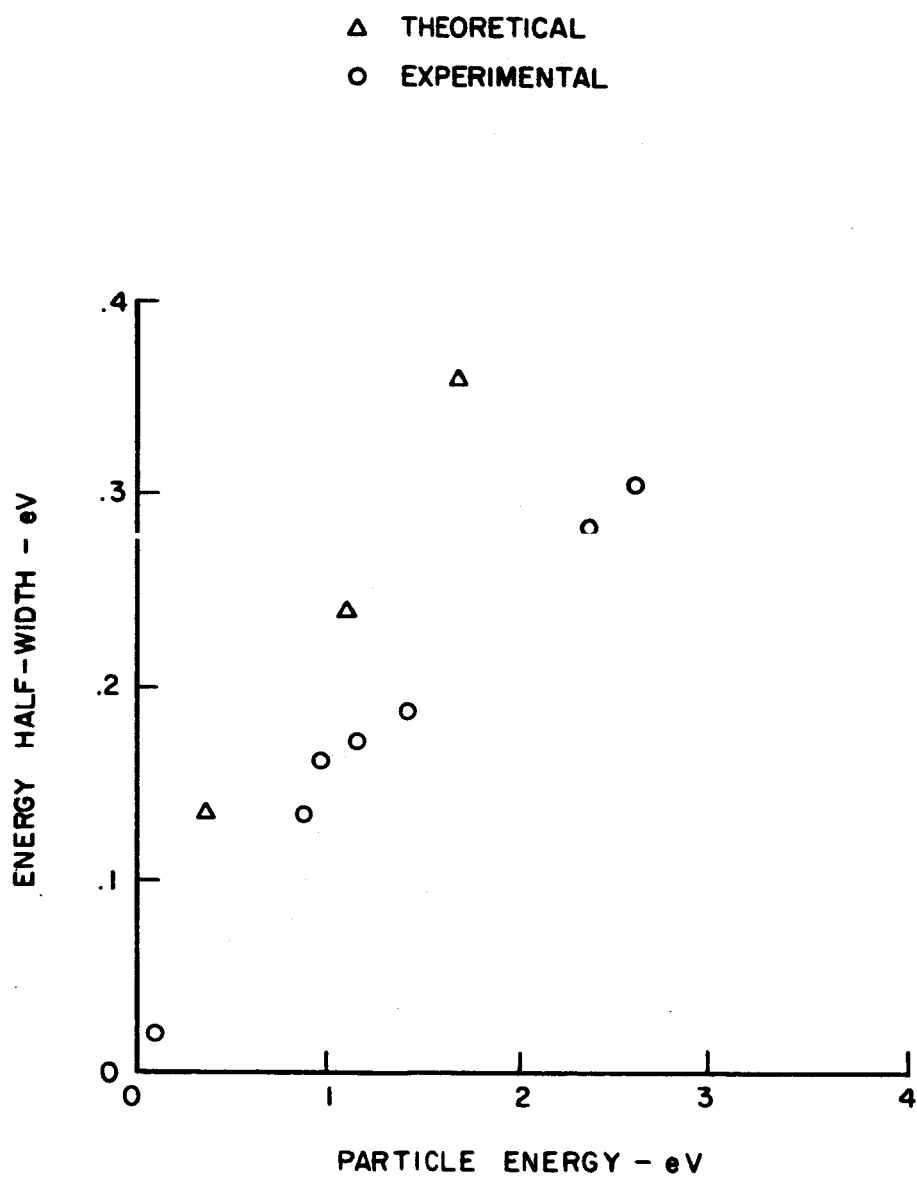


## NORMALIZED ION BEAM ENERGY DISTRIBUTION

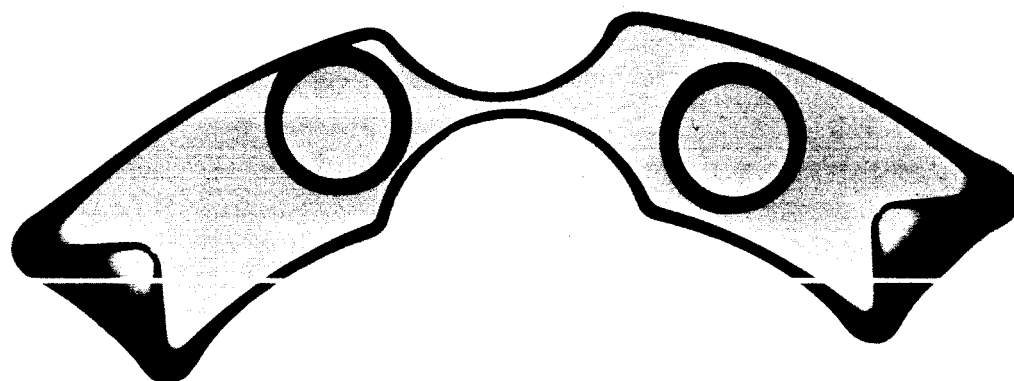
PEAK ENERGY = 2.59 eV



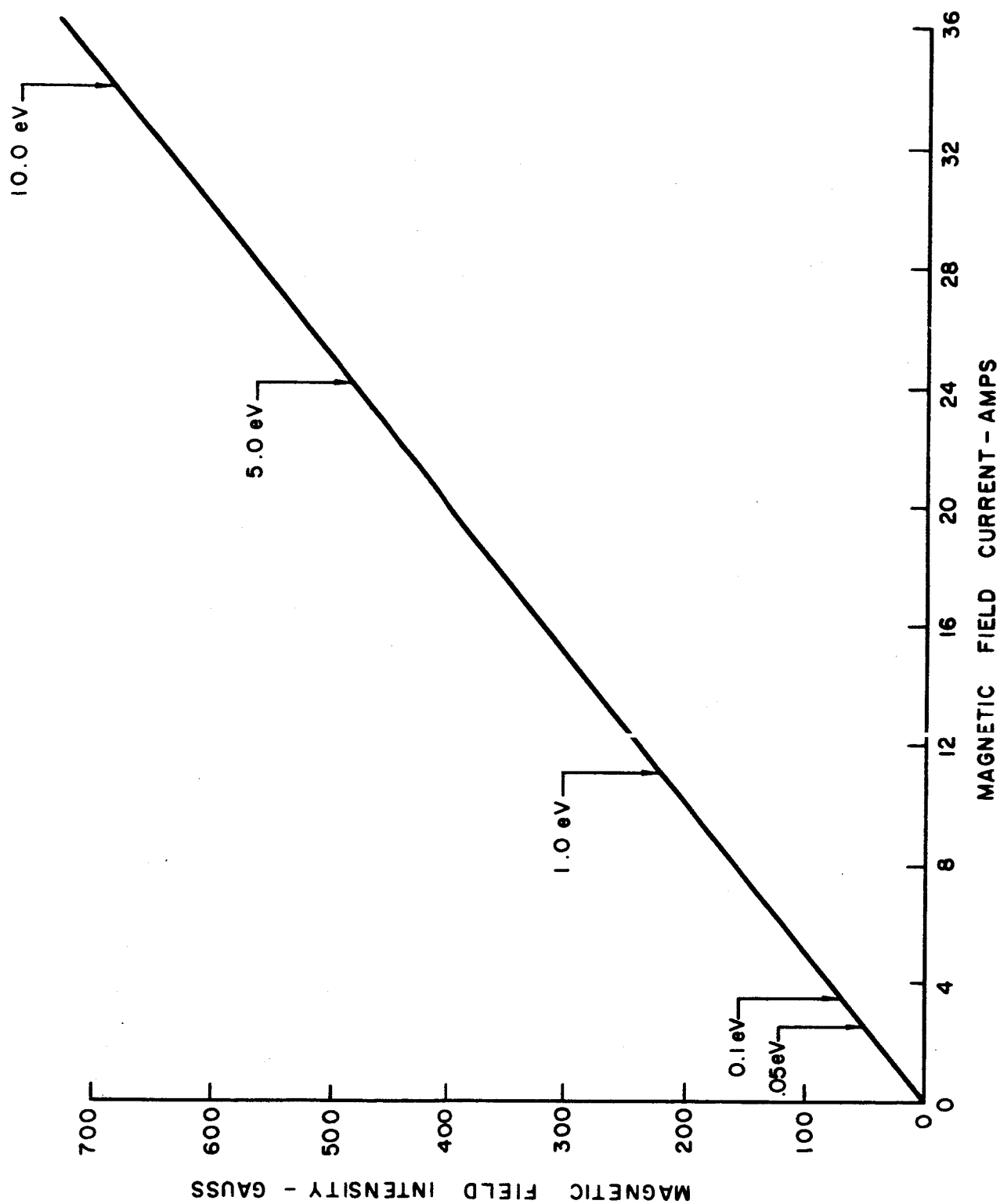
## ION BEAM HALF - WIDTHS



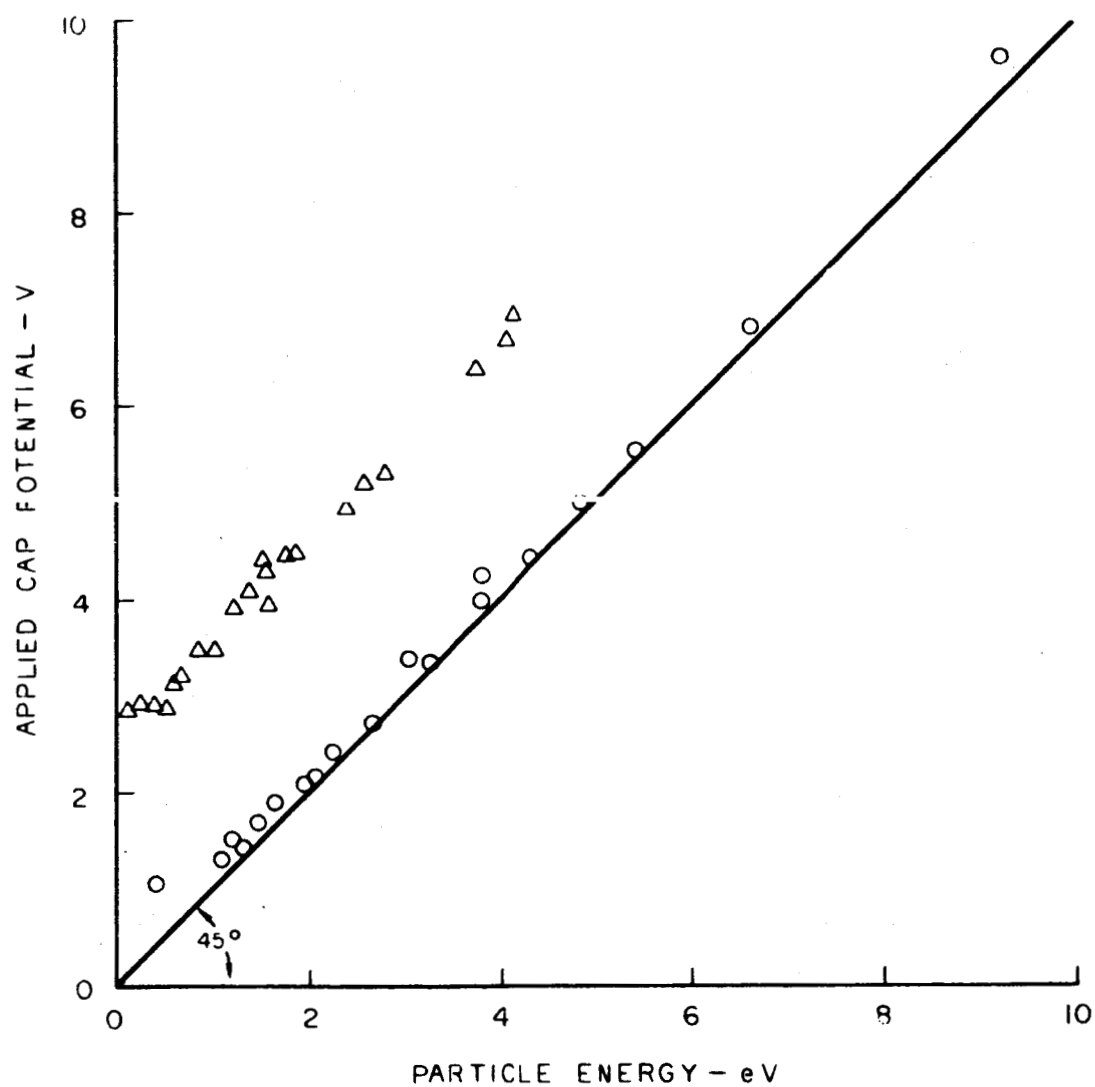
X- RAY OF ELECTRO - FORMED COLLISION CHAMBER



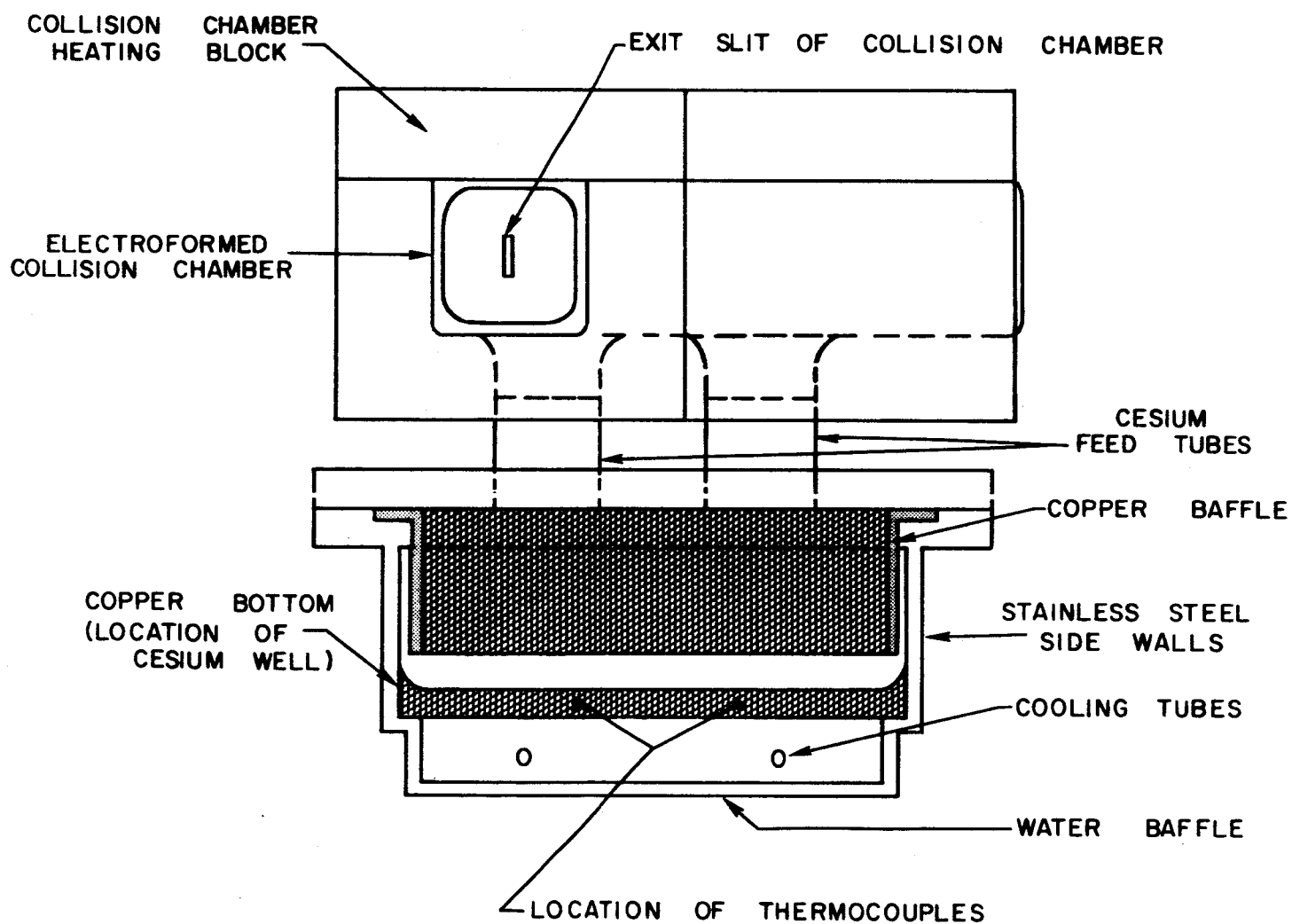
## MAGNETIC FIELD CALIBRATION



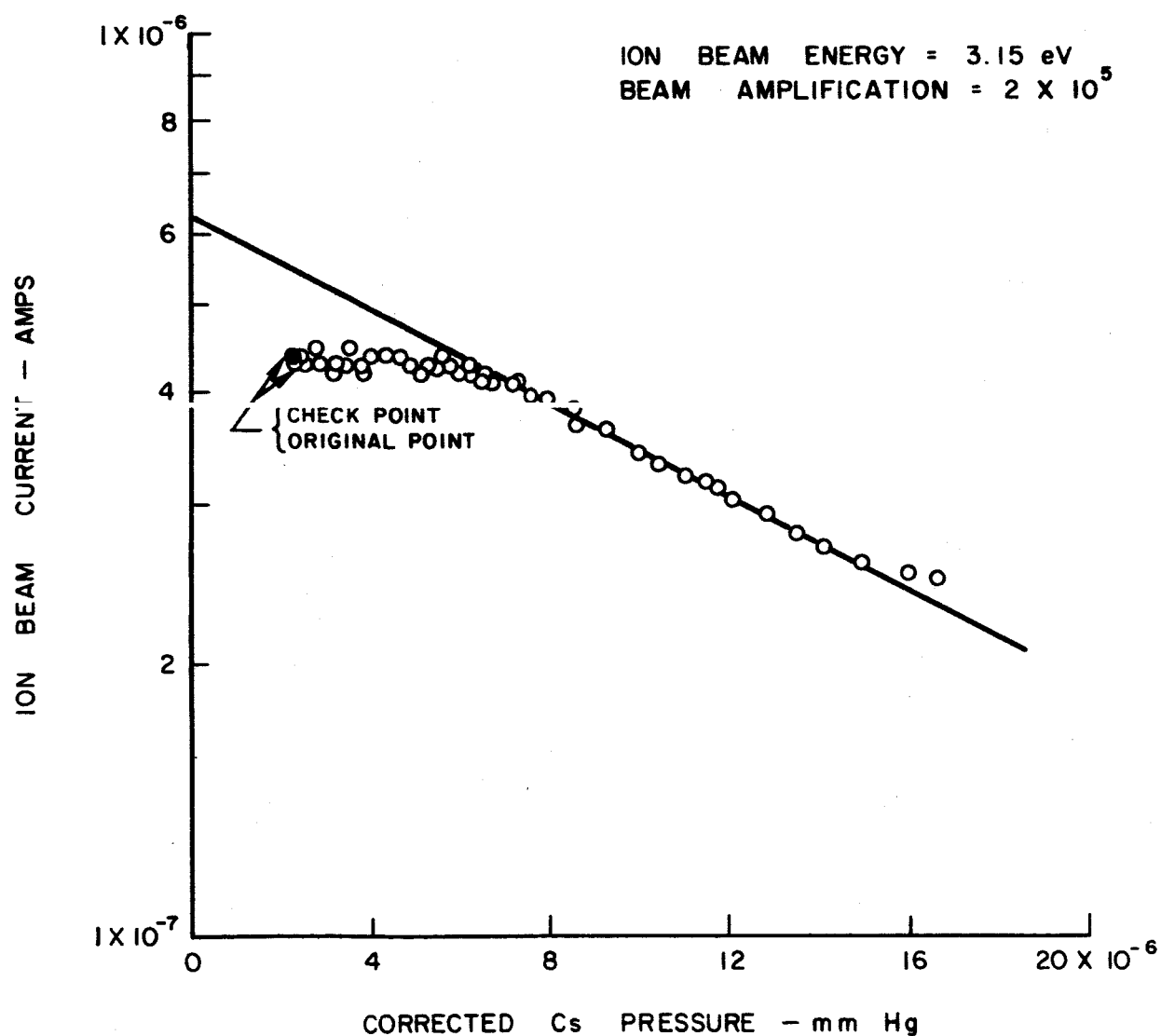
VARIATION OF APPLIED CAP POTENTIAL  
WITH MEASURED ION ENERGY



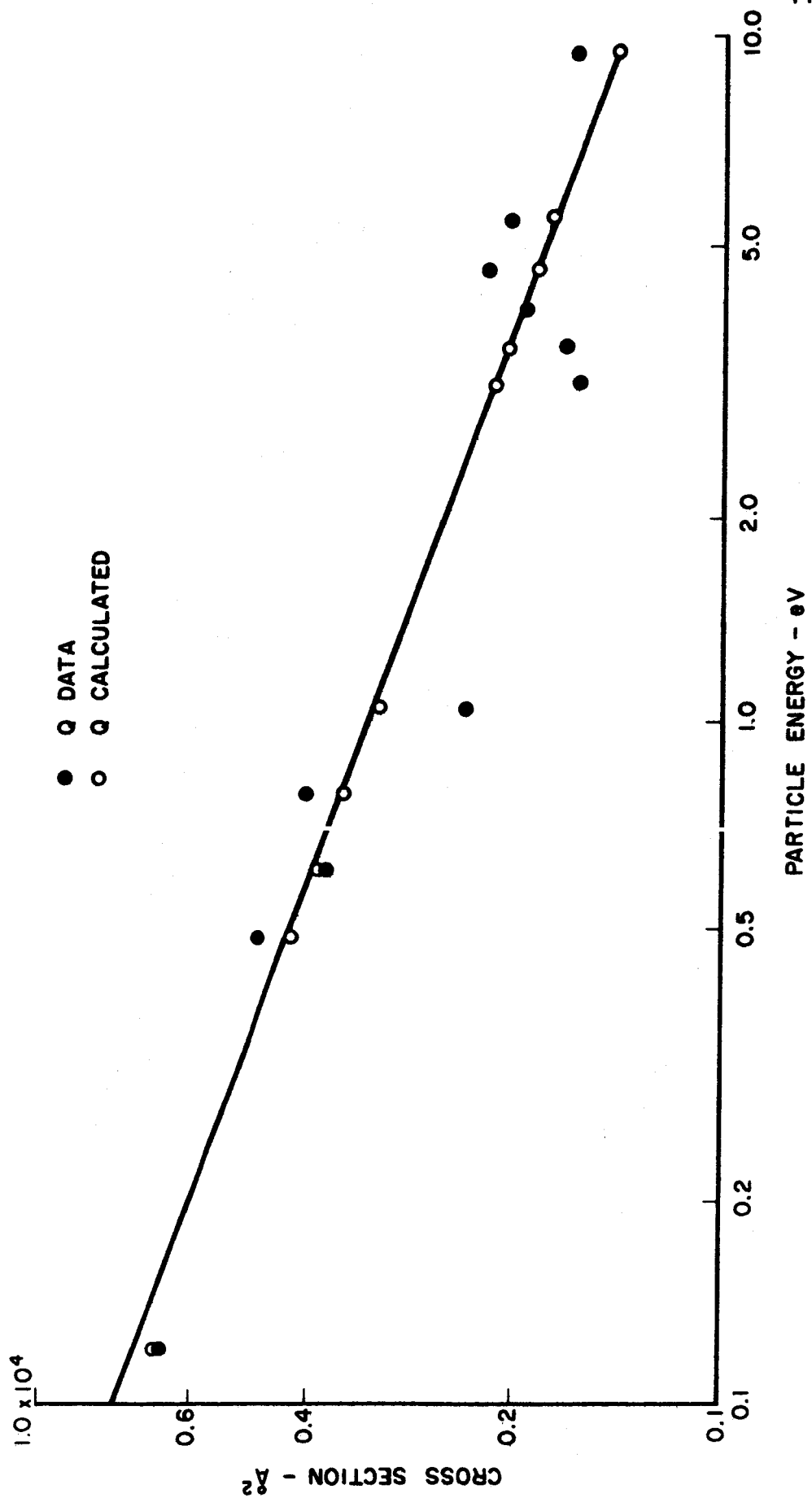
## COLLISION CHAMBER AND CESIUM RESERVOIR



# TYPICAL ION BEAM ATTENUATION WITH INCREASING COLLISION CHAMBER PRESSURE

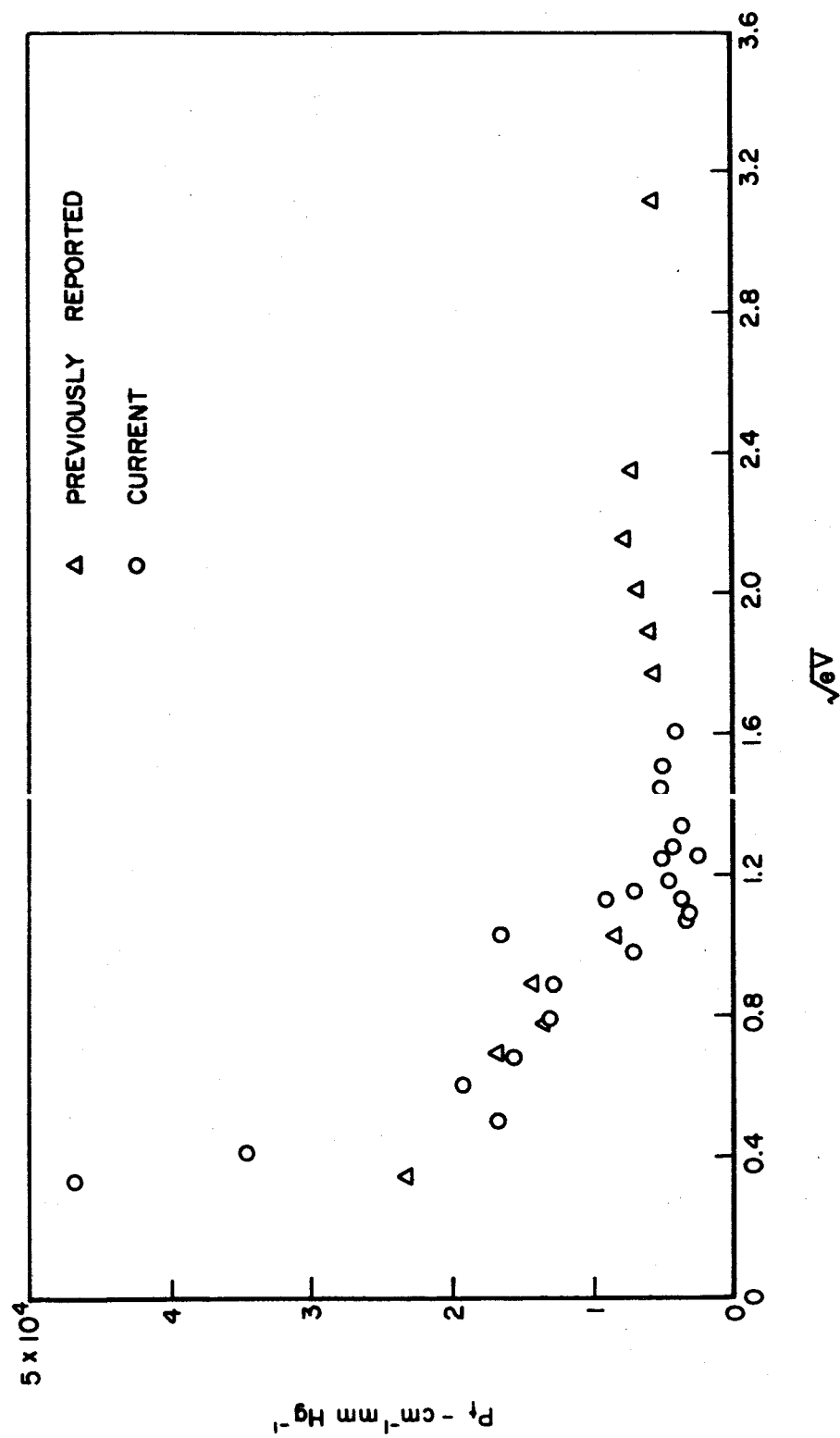


# CORRECTED TOTAL COLLISION CROSS SECTION





## COMPARISON OF CURRENT DATA AND PREVIOUSLY REPORTED DATA



DISTRIBUTION LIST FOR UNITED AIRCRAFT CORPORATION  
Contract No. NAS3-4171  
Semiannual and Final Reports

	<u>No. of Copies</u>
Aerojet General Nucleonics San Ramon, California Attention: K. Johnson	1
Aerospace Corporation El Segundo, California Attention: Librarian	1
Air Force Cambridge Research Center (CRZAP) L. G. Hanscom Field Bedford, Massachusetts	1
Air Force Spacial Weapons Center Kirtland Air Force Base Albuquerque, New Mexico Attention: Chief, Nuclear Power Division	1
Air Force Systems Command Aeronautical Systems Division Flight Accessories Laboratory Wright-Patterson AFB, Ohio Attention: AFAPL (APIP-2, A. E. Wallis)	1
Allison Division General Motors Corporation Indianapolis 6, Indiana Attention: Don L. Dresser	1
Aracon Laboratories Virginia Road Concord, Massachusetts Attention: S. Ruby	1
Argonne National Laboratory 9700 South Cass Avenue Argonne, Illinois Attention: Aaron J. Ulrich	1

D-920243-12

Illinois Institute of Technology  
Research Institute  
10 West 35th Street  
Chicago 16, Illinois  
Attention: D. W. Levinson

1

Atomics International  
P. O. Box 309  
Canoga Park, California  
Attention: Robert C. Allen  
Charles K. Smith

1

1

The Babcock & Wilcox Company  
1201 Kemper Street  
Lynchburg, Virginia  
Attention: Russel M. Ball

1

Battelle Memorial Institute  
505 King Avenue  
Columbus 1, Ohio  
Attention: David Dingee  
Don Keller

1

1

The Bendix Corporation  
Research Laboratories Division  
Northwestern Highway  
Detroit 35, Michigan  
Attention: W. M. Spurgeon

1

Bureau of Ships  
Department of the Navy  
Washington 25, D. C.  
Attention: B. B. Rosenbaum  
John Huth

1

1

Consolidated Controls Corporation  
Bethel, Connecticut  
Attention: David Mends

1

Mr. John McNeil  
Market Development Manager  
Research Division  
Allis-Chalmers Manufacturing Company  
Post Office Box 512  
Milwaukee, Wisconsin

1

D-920243-12

Douglas Aircraft Company  
Missile & Space Engineering  
Nuclear Research (AZ-260)  
3000 Ocean Park  
Santa Monica, California  
Attention: A. Del Grosso

1

Electro-Optical Systems, Incorporated  
300 North Halstead Avenue  
Pasadena, California  
Attention: A. Jensen

1

Ford Instrument Company  
32-36 47th Avenue  
Long Island City, New York  
Attention: M. Silverberg

General Atomic  
P. O. Box 608  
San Diego 12, California  
Attention: R. W. Pidd  
L. Yang  
A. Weinberg

1

1

1

General Electric Company  
Missile & Space Vehicle Department  
3198 Chestnut Street  
Philadelphia 4, Pennsylvania  
Attention: Library

1

General Electric Company  
Knolls Atomic Power Laboratory  
Schenectady, New York  
Attention: R. Ehrlich

1

General Electric Company  
Power Tube Division  
One River Road  
Schenectady 5, New York  
Attention: D. L. Schaefer

1

General Electric Company  
Nuclear Materials & Propulsion Operation  
P. O. Box 15132  
Cincinnati 15, Ohio  
Attention: J. A. McGurty

1

D-920243-12

General Electric Company  
Research Laboratory  
Schenectady, New York  
Attention: Volney C. Wilson  
John Houston

1  
1

General Electric Company  
Special Purpose Nuclear System Operations  
Vallecitos Atomic Laboratory  
P. O. Box 846  
Pleasanton, California  
Attention: E. Blue  
B. Voorhees

1  
1

General Motors Corporation  
Research Laboratories  
Warren, Michigan  
Attention: F. E. Jamerson

1

Hughes Research Laboratories  
3011 Malibu Canyon Road  
Malibu, California  
Attention: R. C. Knechtli

1

Institute for Defense Analyses  
400 Army-Navy Drive  
Arlington, Virginia 22202  
Attention: R. C. Hamilton

1

Jet Propulsion Laboratory  
California Institute of Technology  
4800 Oak Grove Drive  
Pasadena, California  
Attention: Arvin Smith  
Peter Rouklove

1  
1

Los Alamos Scientific Laboratory  
P. O. Box 1663  
Los Alamos, New Mexico  
Attention: G. M. Grover  
Walter Reichelt

1  
1

Marquardt Corporation  
Astro Division  
16555 Saticoy Street  
Van Nuys, California  
Attention: A. N. Thomas

1

Martin - Nuclear  
Division of Martin-Marietta Corporation  
P. O. Box 5042  
Middle River 3, Maryland  
Attention: J. Levedahl 1

Massachusetts Institute of Technology  
Cambridge, Massachusetts  
Attention: E. N. Carabateas 1

National Aeronautics & Space Administration  
Western Operations Office  
150 Pico Boulevard  
Santa Monica, California  
Attention: Fred Glaski 1

National Aeronautics & Space Administration  
Manned Spacecraft Center  
Houston, Texas  
Attention: J. D. Murrell 1

National Aeronautics & Space Administration  
600 Independence Avenue, N. W.  
Washington 25, D. C.  
Attention: Fred Schulman 1  
James J. Lynch 1  
H. Harrison 1  
Walter Scott 1

National Aeronautics & Space Administration  
Lewis Research Center  
21000 Brookpark Road  
Cleveland, Ohio 44135  
Attention: Roland Breitwieser (C&EC) 1  
Robert Migra (NRD) 1  
Bernard Lubarsky (SPSD) 1  
James J. Ward (SPSD) 1  
Herman Schwartz (SPSD) 1  
C. Walker (SPSPS) 1  
R. Mather (SPSD) 1  
H. E. Nastelin (SPSD) 3  
John J. Weber (TUO) 1

National Aeronautics & Space Administration  
Marshall Space Flight Center  
Huntsville, Alabama  
Attention: Library 1

D-920243-12

National Aeronautics & Space Administration  
Scientific & Technical Information Facility  
P. O. Box 5700  
Bethesda 14, Maryland  
Attention: NASA Representative

2 Copies &  
1 Reproduction

National Aeronautics & Space Administration  
Goddard Space Flight Center  
Greenbelt, Maryland  
Attention: Joseph Epstein

1

National Bureau of Standards  
Washington, D. C.  
Attention: Library

1

Oak Ridge National Laboratory  
Oak Ridge, Tennessee  
Attention: Library

1

Office of Naval Research  
Power Branch  
Department of the Navy  
Washington 25, D. C.  
Attention: Cdr. J. J. Connelly, Jr.

1

Power Information Center  
University of Pennsylvania  
Moore School Building  
200 South 33rd Street  
Philadelphia 4, Pennsylvania

1

Pratt & Whitney Aircraft Corporation  
East Hartford 8, Connecticut  
Attention: William Lueckel  
Franz Harter

1

1

Radio Corporation of America  
Electron Tube Division  
Lancaster, Pennsylvania  
Attention: Fred Block

1

Radio Corporation of America  
David Sarnoff Research Center  
Princeton, New Jersey  
Attention: Karl G. Hernqvist  
Paul Rappaport

1

1

The Rand Corporation 1700 Main Street Santa Monica, California Attention: Librarian	1
Republic Aviation Corporation Farmingdale, Long Island, New York Attention: Alfred Schock	1
Space Technology Laboratories Los Angeles 45, California Attention: Kenneth K. Tang	1
Texas Instruments, Incorporated P. O. Box 5474 Dallas, Texas Attention: R. A. Chapman	1
Thermo Electron Engineering Corporation 85 First Avenue Waltham 54, Massachusetts Attention: George Hatsopoulos Ned Rasor	1 1
Thompson Ramo Wooldridge, Incorporated 7209 Platt Avenue Cleveland, Ohio Attention: W. J. Leovic	1
United Nuclear Corporation Five New Street White Plains, New York Attention: Al Strasser	1
U. S. Army Signal R & D Laboratory Fort Monmouth, New Jersey Attention: Emil Kittil	1
U. S. Atomic Energy Commission Division of Reactor Development Washington 25, D. C. Attention: Direct Conversion Branch	1
U. S. Atomic Energy Commission Technical Reports Library Washington 25, D. C. Attention: J. M. O'Leary	3



D-920243-12

U. S. Atomic Energy Commission  
Department of Technical Information Extension  
P. O. Box 62  
Oak Ridge, Tennessee

3

U. S. Atomic Energy Commission  
San Francisco Operations Office  
2111 Bancroft Way  
Berkeley 4, California  
Attention: Reactor Division

1

U. S. Naval Research Laboratory  
Washington 25, D. C.  
Attention: George Haas  
Library

1

1

Defense Research Corporation  
P. O. Box 3587  
Santa Barbara, California  
Attention: Harold W. Lewis

1

Westinghouse Electric Corporation  
Research Laboratories  
Pittsburgh, Pennsylvania  
Attention: R. J. Zollweg

1

The Boeing Company  
Seattle, Washington  
Attention: Howard L. Steele

1

Varian Associates  
611 Hansen Way  
Palo Alto, California  
Attention: Ira Weissman

1